Titan's interaction with the Saturnian magnetosphere

Leonardo H. Regoli

A dissertation submitted in partial fulfillment

of the requirements for the degree of

Doctor of Philosophy

of

University College London.

Department of Space and Climate Physics

University College London

August 24, 2016

I, Leonardo H. Regoli, confirm that the work presented in this thesis is my own. Where information has been derived from other sources, I confirm that this has been indicated in the work.

Abstract

In this thesis, a combination of data analysis and test particle simulations is used in order to study several aspects of the complex interaction of Titan with the Saturnian magnetosphere. First, the energetic charged particles environment at the orbital distance of Titan is studied using data from the MIMI/LEMMS instrument. Average fluxes and spectral slopes for energetic ions and electrons are analysed. A large variability is found, and it is interpreted as originated from the high mobility of the energetic ions and electrons, making a simple classification of this environment practically impossible, with only a weak correlation between the ion average fluxes with the plasma environment detectable and an asymmetry between the noon-to-dusk and midnight-to-dawn sectors. Second, the effect of local electromagnetic field disturbances in the access of energetic H^+ and O^+ ions is studied. By studying the trajectories of individual particles to predict where they will deposit their energy, differences in ionisation rates at different locations around the moon of almost 80% are found for H^+ ions and of more than 15% for the case of O^+ ions. Finally, the contribution of freshly produced pickup ions to the overall mass loss of the atmosphere is investigated by looking at particular signatures left by these ions in the thermal plasma data from the CAPS/IMS instrument. A statistical survey of all the flybys with available data leads to a constraint of the region around the moon where these ions are detected. Mass losses on the anti-Saturn side of the moon of between 570 kg/day and 1 tonne/day are derived depending on the species, accounting for a small fraction of the total losses estimated from distant tail observations.

To Bene

Acknowledgements

I would first like to acknowledge all the support received throughout these three years from my PhD supervisors, Geraint Jones, Andrew Coates, Elias Roussos and Norbert Krupp. It is always said that one of the most important things when embarking on a project as complex as the completion of a PhD thesis is the choice of supervisors and I was certainly really fortunate to count with appropriate guidance in every possible aspect while maintaining a perfectly pleasant and relaxed interaction with all of them. Moreover, I am truly thankful as well for all the support received when it came to practical matters that were certainly beyond their expected areas of support such as financial struggles or the search for a postdoc position, to name just a couple.

The possibility to collaborate with different people from my research field with fruitful discussions during conferences and per email had also a significant contribution to my understanding of different topics. I really enjoyed my interaction with Kostas Dialynas, Peter Kollmann, Janet Luhmann, Steve Ledvina, Michelle Thomsen, Hunter Waite, Sven Simon and Neil Murphy among others. Thanks to all of them for taking the time to talk to students and help them during the first stages of what hopefully will become a successful scientific career.

Thanks to Ingo Müller-Wodarg and Jonathan Rae for carefully reading this thesis and acting as examiners during my viva. I know that a lot of work is involved in such a process and their suggestions ended up as important contributions for the improvement of the final result.

The support provided by the administrative staff at both institutions (MSSL and MPS) was also crucial in the completion of this thesis. Special thanks to Ros,

Libby, Julia and Jane at MSSL and Sonja and Sibylla at MPS.

I would also like to thank all the people with whom I was able to share my working and free time, both at MSSL and at MPS. It is impossible to mention each person, but I should at least acknowledge the Offices 108 and 210 people at MSSL (Jamie, Will, Yudish, Ravi, Marianna, Kim, Sam, Gethyn and Annie), Ali for the never-ending conversations at Libby's, the ever-changing open space occupants at MPS (Benjamin, David, Chris, to name a few) and of course the lunch and coffee group at MPS (this is just too long to put here!).

A very important contribution in the form of support throughout these three years definitely comes from Claudia, my wife. She has always been there to support me both when I had to spend long weekends working but also when we could simply enjoy life (the most wonderful life I could ever imagine!) together.

Also, the drive to pursue a career in academic research came from my parents, Héctor and Sylvia, who always taught me the wonders of nature since I was a child and my sisters, Carolina and Xiomara. All of them were always an example to follow, both in the academic and living aspects.

Finally, I would like to acknowledge the invaluable contribution of the Impact scholarship from UCL and the Max Planck Society. It would have been absolutely impossible for me to spend these three years studying such a fascinating topic without the economic support provided by it.

Contents

List of Figures

List of Tables

Chapter 1

Introduction

This thesis describes studies of different subjects related to the interaction of Titan with the Saturnian magnetosphere. Both simulations and data analysis were used to complete the research described. For the data analysis, three main instruments that are part of the Cassini spacecraft, namely the Cassini Plasma Spectrometer (CAPS), the Magnetospheric Imaging Instrument (MIMI) and the Magnetometer investigation (MAG) were used. Chapter 3 gives a description of the Cassini spacecraft as a whole and of the instruments used throughout the duration of the studies summarised here.

Three main research topics are addressed in Chapters 4 to 6. In Chapter 4, a statistical analysis of the energetic ion and electron environment at Titan's orbit is performed, using data collected over a period of more than 10 years by the MIMI instrument. This analysis provides an overview of the average fluxes as well as energy distribution of the energetic plasma population that can contribute to the ionisation of neutrals in Titan's atmosphere.

In Chapter 5, a specific flyby is used to study the energy deposition and ionisation rates from energetic ions at Titan. A particular emphasis is put on the influence that the draping of the field lines around the moon has on the trajectories of the energetic particles and how this affects the ionisation rates on a local scale. For this, data from the MIMI instrument as well as test particle simulations using a tracing code developed for this thesis are used.

In Chapter 6, the production of pickup ions in the vicinity of Titan and the mass

loss due to the escape of these ions is investigated based on data provided by the CAPS instrument. After studying in detail an individual flyby from data analysis and simulations perspective to validate the detection of pickup ions, a statistical study is carried out with all the data available to estimate the escape region and rates of these particular ions.

All the research described in this thesis is related to magnetospheric physics, especially with the motion of charged particles inside a magnetosphere. It is for this reason that Chapter 2 contains a review of some of the basic concepts that are relevant to the understanding of the analysis and results presented later on.

1.1 Saturn

Saturn, with an equatorial radius of 60268 km (almost ten times that of Earth) is the second largest planet in the Solar System after Jupiter. It is the sixth furthest planet from the Sun and is one of the so-called gas giants. It hosts the most prominent rings system of all the planets and is orbited by more than 60 moons.

The planet has a rotation period of only $\sim 10\ h\ 34\ m$ (Read et al. 2009). The exact rotation period is unknown due to variations in a radio emission from the planet known as the Saturn Kilometric Radiation, SKR, from which the rotation period was originally inferred. It has an internal magnetic field whose dipole axis is aligned with the rotation axis to within 1° with an equatorial surface strength of approximately 20 nT. This creates an axisymmetric near-dipole dominated region in the inner magnetosphere that is progressively more perturbed when one moves towards the outer regions.

1.1.1 Saturn's magnetosphere

A planetary magnetosphere can be defined as a cavity in space filled with plasma, where the dynamics of that plasma are dominated by the planet's magnetic field. A typical magnetosphere interacts with an external plasma source, which in the case of the Solar System is the solar wind.

In order to facilitate the understanding of the relevant processes for this work, the basic concepts of a magnetosphere will be introduced using Saturn's magneto-

sphere, instead of the usual approach of taking the Earth as example. This approach is valid, since the basic structure is similar in both planetary systems, except that the planetary magnetic is field reversed.

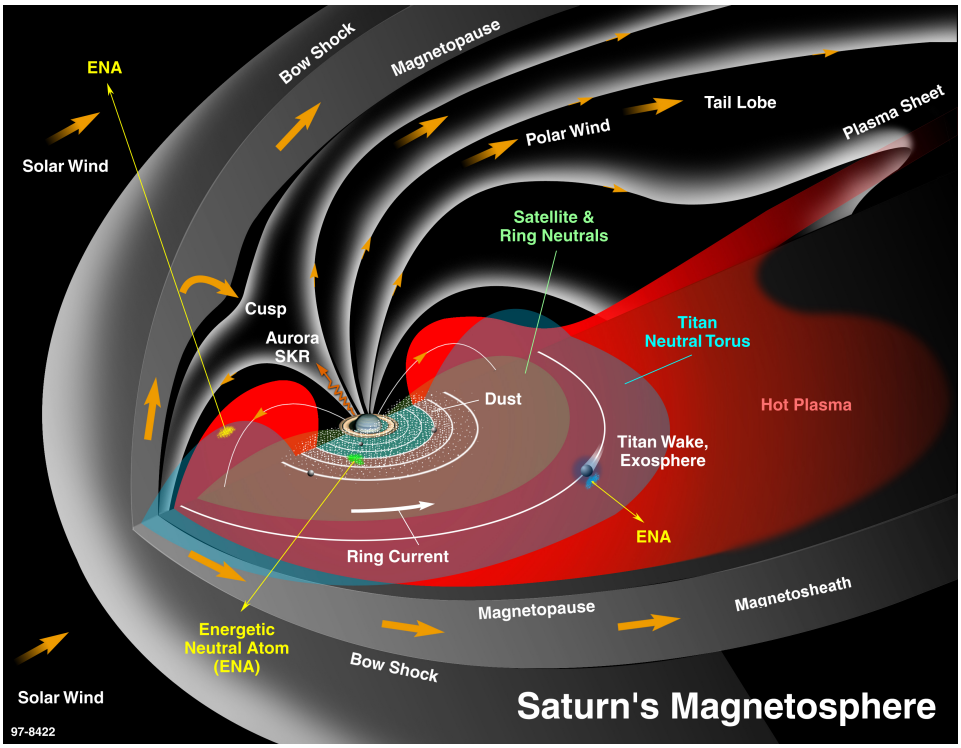

Figure 1.1: Saturn's magnetosphere (adapted from Krimigis et al. 2004).

Figure 1.1 shows a schematic of the Saturnian magnetosphere. In the schematic, the solar wind encounters the planet's magnetic field from the lower left and is deflected around the planet. The solar wind dynamic pressure compresses the magnetic field lines on the dayside of the planet and stretches those located on the night side, creating what is known as the magnetotail.

In the process just described, some regions and boundaries are created, where plasmas of different composition, temperature and densities can be encountered. The first one of these boundaries is the bow shock, located at the surface where the supersonic solar wind is first affected by the presence of the planet, causing a rapid deceleration of the plasma.

A transition region known as the magnetosheath is located right after the bow shock, where slowed-down and heated solar wind particles can be encountered. This is the region located between the bow shock and the magnetopause in the

schematic shown in Figure 1.1.

The inner boundary of the magnetosheath is the magnetopause. Inside the magnetopause is where the region known as the magnetosphere is located. Outside the magnetopause, the solar wind dominates. Inside the magnetopause, the planet's magnetic field dominates, and all the plasma processes and transport are internally driven (even though for some processes the solar wind will still play a role, due to reconnection of magnetospheric and heliospheric magnetic field lines).

Inside the magnetosphere, some characteristic structures can be encountered, such as the ring current, the plasma sheet, the cusps and the lobes.

The ring current is an electric current system created due to the opposite direction of the drift of positively and negatively charged trapped particles around the planet. At Saturn, the ring current is estimated to have a value between 8 and 17 MA with an influence in the region between $\sim 6\ R_S$ and ~ 12 to $20\ R_S$ (the outer boundary being heavily controlled by the magnetopause location, Gombosi et al. 2009).

As the planet rotates, due to ion- and electron-neutral collisions the ionosphere corotates with it, draging the magnetic field lines along. This causes in turn the plasma of the magnetosphere to corotate as well . The centrifugal force resulting from the high rotation speed forces the plasma to be confined close to the equatorial plane forming the so-called current or plasma sheet. Arridge et al. (2008) reported that this current sheet can be bent in the form of a bowl due to the direction of arrival of the solar wind (Figure 1.2).

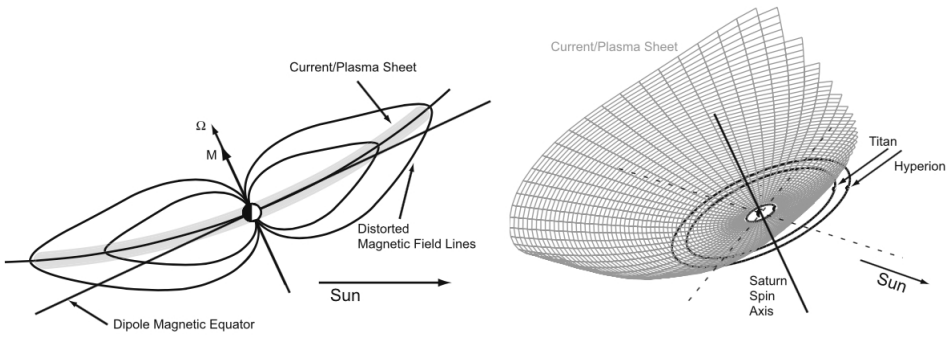

Figure 1.2: Warping of the current sheet at Saturn caused by solar wind dynamic pressure (from Arridge et al. 2008).

The cusps are the high-latitude regions close to the poles where, due to magnetic reconnection with the heliospheric magnetic field, solar wind particles can enter the planet's magnetosphere (Smith and Lockwood 1996).

Finally, the lobes are regions with relatively low plasma density (Rymer et al. 2009). They are located to the north and south of the plasma sheet. These regions also exhibit a magnetic field (especially in the outermost regions) much stronger than what would be expected from a dipole (Gombosi et al. 2009).

With respect to ion sources, Saturn's magnetosphere is mostly populated by ions that originate by impact ionisation of neutrals from an H_2O cloud that ultimately comes from the icy moon Enceladus (Blanc et al. 2015). Other sources that play a less important role are Saturn and Titan's atmospheres, ionospheres, as well as the ring system.

The moons and the rings also act as sinks for energetic particles, with a clear depletion observed in the vicinity of the moons, commonly referred to as microsignatures, and an absence of energetic particles above and below the rings (Krupp et al. 2009).

Saturn's magnetosphere is frequently classified as a middle case between those of Earth and Jupiter in terms of the dominating processes (Gombosi et al. 2009). Earth is the closest to the Sun of all three and it has a small internal mass source of magnetospheric plasma and its magnetosphere is dominated by solar wind activity while at Jupiter a strong magnetic field and the internal mass sources (especially the Galilean moon Io) create a magnetospheric environment in which solar wind only plays a minor role. The Saturnian magnetosphere in turn falls somewhere in between, with both internal processes (mass loading from Enceladus, Titan, icy moons and rings) and the solar wind activity playing important roles.

In terms of internal transport processes, Saturn and Jupiter are rotationally dominated. This is a consequence of the fast rotation rate and is the cause of having an extended plasma sheet and current sheet that can be encountered at all local times and in the outer magnetosphere. In contrast, the Earth's plasma sheet is only encountered on the night side where the field lines are stretched as a consequence

of the solar wind compressing the dayside's magnetosphere.

Another special aspect of the Saturnian magnetosphere is the dominance of neutral molecules, mostly hydrogen and water products, with their densities exceeding by at least one order of magnitude that of local plasma almost everywhere (André et al. 2008). In comparison with Jupiter, Saturn's magnetosphere contains 100 times more neutrals (Krupp 2014). This affects the overall transport processes by increasing the charge exchange rate of ions that result in a drag on the corotation of magnetospheric plasma (Mauk et al. 2009). Also, when an ion with high energy induces charge exchange with a neutral, an energetic neutral atom (ENA) is created that can travel on a straight trajectory (unaffected by the electromagnetic field) leaving the region where it was created.

1.1.2 Overall structure of the Saturnian magnetosphere

Using combined data from multiple Cassini instruments gathered during the Cassini Prime Mission, a classification of the macroscopic magnetospheric regions was described by Arridge et al. (2011b). Since the available data are restricted to the areas close to the equatorial plane, the classification is valid for the equatorial regions.

At the largest scale, three distinctive regions are identified, namely the inner, middle and outer magnetosphere, with the boundaries between the regions roughly located at 6 R_S and 15 R_S. The inner region is characterised by a high flux of low-energy particles with a comparatively low flux of particles with energies of tens to hundreds of keV.

Saturn, as the Earth, has a region, known as the radiation belts, with high flux of trapped ions and electrons that surrounds the planet covering an equatorial distance between 2.3 R_S and 3.5 R_S. The most intense part of the radiation belts is located in the inner region, which is also populated by thermal water group ions and protons. By using an adapted version of a model developed by Connerney et al. (1983) and comparing the magnetometer data with the model, Dougherty et al. (2005) determined that in this region, the magnetic field configuration is dominated by the planet's internal dipolar field with some perturbations due to the planetary ring current.

In the middle magnetosphere, the radiation belts are present with an important reduction in intensity, except for times when a transient radiation belt is present, as reported by Roussos et al. (2008). In the boundary between the two regions, there is an important decrease in flux of particles with energies above 10 MeV. The neutral gas density also decreases with increasing distance from Enceladus. Here, the magnetic field starts to depart from the dipolar configuration observed in the inner region.

The outer magnetosphere is much more variable with a magnetic field configuration which is not only far from being dipolar but also presents important perturbations that are influenced by the local environment (Saturn local time asymmetries, the presence of Titan, solar wind dynamic pressure, etc.). In this region, the local time asymmetries are very pronounced, with a compressed magnetic field on the dayside and the stretched field lines forming the magnetotail on the night side. Also in this region, the temporal variations induced by the flapping of the current sheet are more visible, alternating between dense regions (plasma sheet) and empty regions (lobes). The magnetopause position at the sub-solar point stands at around 20 R_S (close to Titan's orbit). It has been suggested that the magnetopause position is actually influenced by the presence or absence of Titan in the magnetopause's vicinity at a given time, apparently by increasing the total pressure by means of its contribution to the local mass loading Wei et al. 2009).

1.1.3 Plasma transport processes in the Saturnian magnetosphere

Inside planetary magnetospheres, there are some processes that drive circulation and transport of bulk plasma. Two of these processes are dominant inside the Saturnian magnetosphere, namely the Dungey cycle (Dungey 1961) and the Vasyliūnas cycle (Vasyliūnas 1983).

Dungey cycle

When the interplanetary magnetic field (IMF) is directed opposite to that of the planet (southwards for the Earth and northwards for Saturn), a merging of the IMF

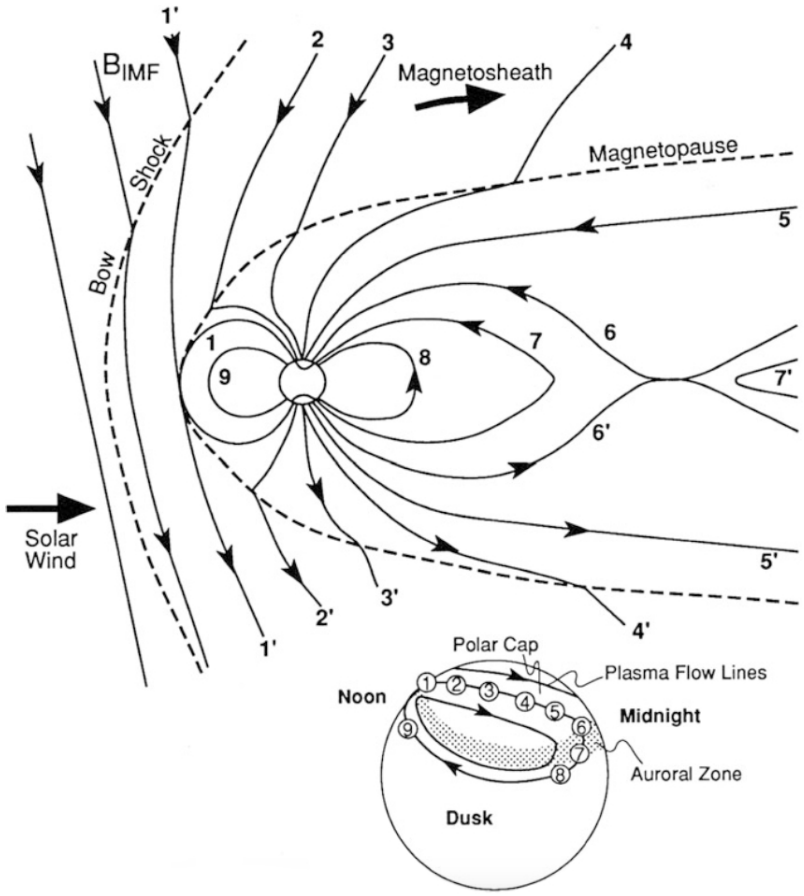

Figure 1.3: Merging of IMF and planetary magnetic field lines on the magnetopause and reconnection on the tail, responsible for the convection electric field (shown for Earth; from Hughes 1995).

lines and those of the planet located in the magnetopause can occur through reconnection, creating open magnetic field lines with their origin in the polar caps (Figure 1.3).

The solar wind convects the field lines towards the tail side, following the path marked by the numbers on the inset of Figure 1.3. This process will carry on until two open lines meet on the tail side and undergo reconnection, resulting in auroral emissions. This creates an interplanetary field lines that ultimately joins the solar wind and a closed field line that is transported towards the planet, causing a flux of plasma that in turn will create an electric field defined by Equation 1.1, where $\bar{E}_c$ represents the convection electric field, $\bar{v}_c$ the plasma velocity and $\bar{B}$ the magnetic field.

$$\bar{E}_c = -\bar{v}_c \times \bar{B} \tag{1.1}$$

This electric field is called the convection field and it has a dawn to dusk direction at Earth and dusk to dawn at Saturn. The magnetic field line eventually returns to the dayside and the process repeats itself to form what is known as the Dungey cycle.

Vasyliūnas cycle

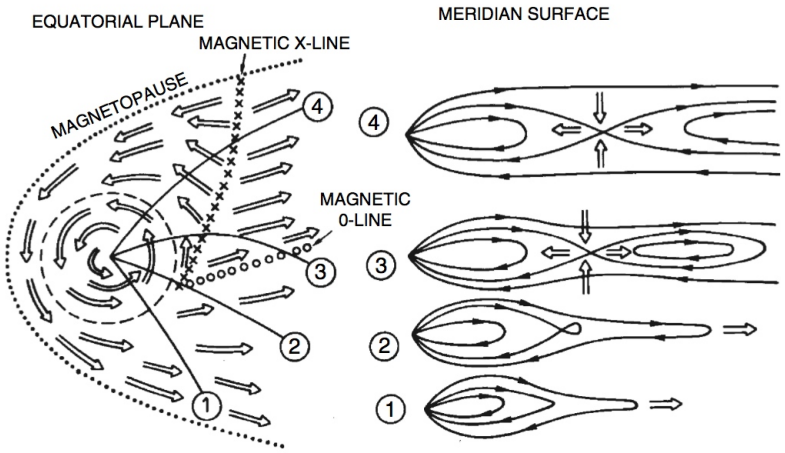

Figure 1.4: Vasyliūnas cycle (from Gombosi et al. 2009).

Apart from the Dungey cycle, another plasma transport process has been observed in the magnetospheres of fast rotators (Jupiter and Saturn so far). In the Vasyliūnas cycle, the mass loading of magnetic field lines, together with the centrifugal force exerted by the fast corotation of plasma induced by the planet, ends up stretching the closed field lines in the post-dusk sector of the magnetosphere, eventually forcing reconnection of the field line with itself on the night side, creating a plasmoid in the process and depleting the field line of plasma.

The sketches on the right of Figure 1.4 show four different snapshots of the process as seen from the side. The sketch on the left shows an equatorial view of the magnetosphere, showing the approximate location of the field lines undergoing reconnection with the thick lines showing the location around the planet where each stage takes place.

Stages 2 and 3 mark the locations where the plasmoids are produced. This location is known as the magnetic O-line, and it arises from the geometry of the closed magnetic field loops that characterises a plasmoid. The magnetic X-line, in turn, marks the locations where the reconnection of the field lines is expected to be found during the cycle.

Comparing both cycles, it is easy to see that the Dungey cycle allows the combination of plasma from magnetospheric and solar wind origin, while the Vasyliūnas cycle, only involving closed field lines, simply provides a mechanism for magnetospheric plasma to be lost to the solar wind.

Corotation electric field

Not directly related to an inwards or outwards plasma transport process, there is another important electric field source in planetary magnetospheres that creates the so-called corotation field, which has its origin in the corotation of plasma inside the magnetosphere. When a planet rotates, due to ion and electron-neutral collisions, it tends to drag the magnetospheric plasma with it causing once again an electric field ($\bar{E}_{cr}$) governed by Equation 1.2, where Ω_P is the angular velocity of the planet, $\bar{r}$ is an arbitrary position and $\bar{B}$ is the magnetic field. This time, the field is directed radially towards the planet for the case of Earth and away from the planet for Saturn.

$$\bar{E}_{cr} = -\left(\Omega_p \times \bar{r}\right) \times \bar{B} \tag{1.2}$$

From Equation 1.2, the equatorial plane electric potential (ϕ_{cr}) can be obtained and is given by Equation 1.3, where B_P is the surface equatorial magnetic field, R_P is the radius of the planet and L is the equatorial distance of the shell (called L-shell in the case of a dipole field, McIlwain 1961) at which the potential needs to be calculated.

$$\phi_{cr} = -\frac{\Omega_p B_p R_p^2}{L} \tag{1.3}$$

An additional electric field mostly pointing in the noon-midnight direction was discovered by studying the microsignatures left by the moons Tethys and Dione

(Andriopoulou et al. 2012). In their study, they observed drifts in the location of the electron dropouts present at the moon tails. These drifts wer consistent with the presence of an additional electric field mostly pointing in the noon-midnight direction. The existence of this field was deduced from the presence of a consistent drift of the microsignatures and it implies an asymmetry in the radial plasma flow in the inner magnetosphere (Jia and Kivelson 2016).

1.2 Titan

Titan is Saturn's largest moon and the second largest moon of the Solar System, after Jupiter's moon Ganymede. Nevertheless, the most prominent feature of Titan is not its size, but the fact that it is the only moon in the Solar System known to have a significant atmosphere.

The moon itself was discovered in 1655 by Christiaan Huygens, a Dutch scientist who made important contributions to different disciplines, including astronomy. The presence of the atmosphere, first suspected by Spanish astronomer Josep Comas I Sola in 1903, was finally detected in 1944 by Gerard Kuiper.

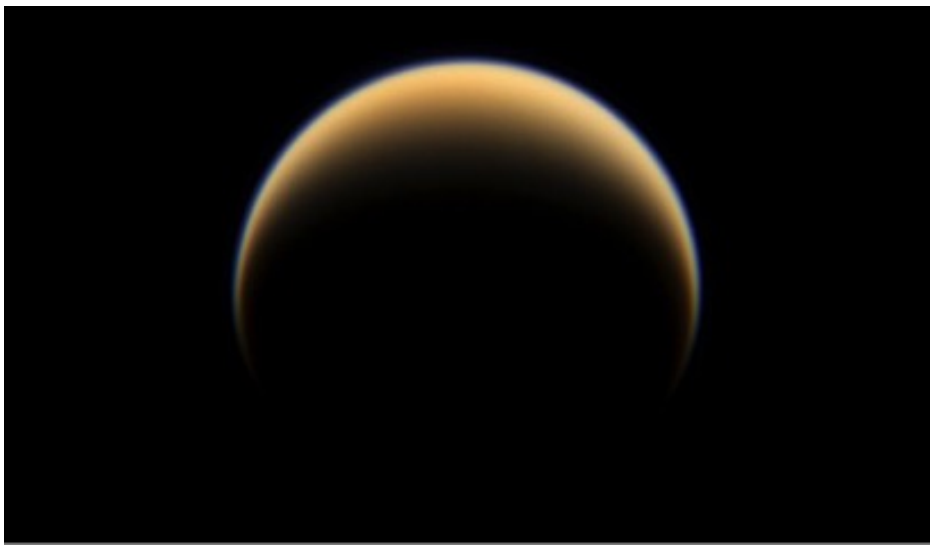

Figure 1.5: Titan's north pole showing the distinctive atmospheric haze as taken by Cassini on June 6, 2009 (NASA/JPL/Space Science Institute).

Titan orbits Saturn at an approximate distance of 20.3 R_S and its orbital period around the planet is 15.95 days. Most of the time, Titan is located in the outer

region of Saturn's magnetosphere but during the Cassini mission, the moon was encountered three times in the magnetosheath (T32, Bertucci et al. 2008, T42, Rymer et al. 2009 and T85, Edberg et al. 2013) and once (T96, Bertucci et al. 2015) in the unshocked solar wind.

Since the orbital period of Titan, 15 days and 22 hours, is much longer than the rotation period of the planet, and due to the fact that the plasma still partially corotates with Saturn at the distance of the moon's orbit, the plasma encounters the moon at a relative speed of approximately 100 - 120 km/s (Hartle et al. 1982, Neubauer et al. 1984).

Prior to the first close encounters with Titan by the Voyager 1 and 2 spacecraft, it was clear that its atmosphere would have a complex composition as determined using spectroscopy techniques. However, only with these close encounters, which occurred on the 12th of November, 1980 and 26th of August, 1981 at distances of 3915 km and 666190 km from its surface respectively, was it possible to get more precise measurements of its composition. With these flybys it was determined that the atmosphere's composition was 97% molecular nitrogen (N_2) and 1.5 to 3% methane (CH_4). The atmospheric surface pressure exceeds that of Earth by approximately 50%.

While planning the Cassini - Huygens mission to Saturn, Titan and its atmosphere were important objectives. This is reflected by the fact that more than 120 flybys will have been performed by Cassini by the time the mission ends in September 2017, some of them reaching altitudes as low as 950 km. Also, the Huygens probe was an important part of the mission, designed as an atmospheric probe to land on the moon and provide in-situ measurements and a vertical profile of the dense atmosphere as well as insight into the surface features that are invisible from orbit due to the thick haze that surrounds the moon.

1.2.1 Titan's atmosphere

Titan's atmosphere has been compared with that of the primitive Earth, raising interest as well among the astrobiology community (Raulin et al. 2009).

Figure 1.6 shows different vertical profiles taken at equatorial latitudes for Ti-

tan's atmosphere obtained with different instruments, including the Huygens lander, as well as a pre-Cassini engineering model (Yelle et al. 1997). The agreement below 600 km between all the measurements, including those for the Voyager era and the Cassini era is an indication of the long radiative time constants at lower altitudes. This implies that the densities are much less influenced by factors such as solar activity or distance of the moon from the Sun (due to the eccentricity of Saturn's orbit, the distance to the Sun varies by slightly more than 1 AU and the solar flux ∼20% between perihelion and aphelion).

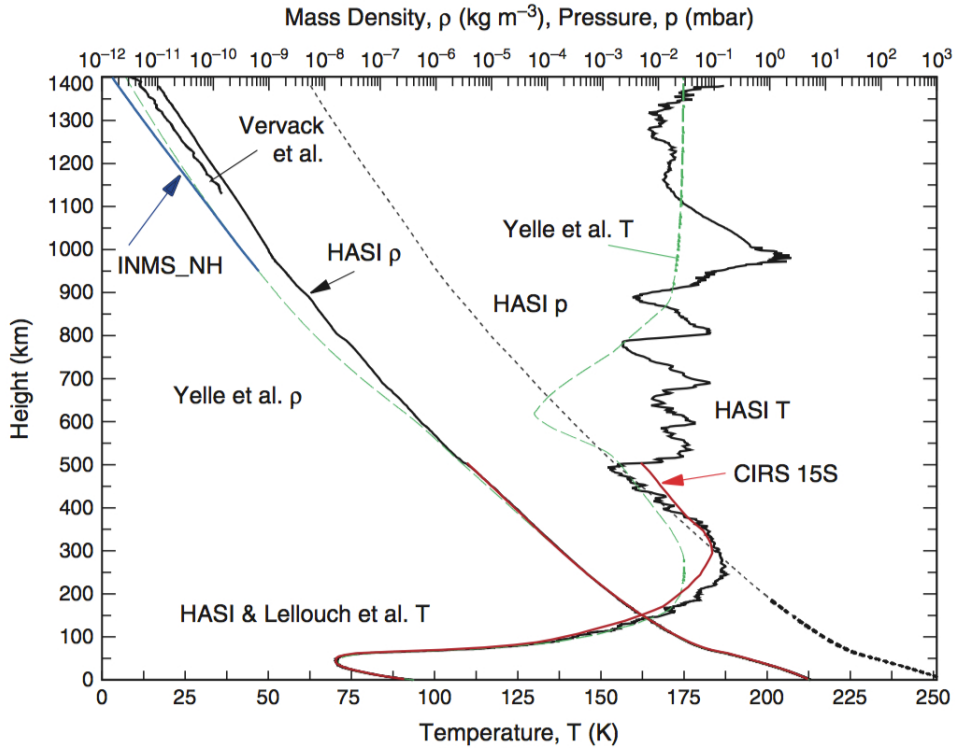

Figure 1.6: Vertical profile of Titan's atmosphere showing neutral density and temperature (from Strobel 2009).

In addition to the variations already discussed, latitudinal variations are present in density, pressure and temperature. These variations have been studied in more detailed during the many flybys performed by Cassini throughout its whole life span.

The uppermost region of the atmosphere is called the exosphere. This is a tenuous environment that can be treated as collisionless. The lower boundary of

the exosphere is the exobase, which can be formally defined as the point where the mean free path of an atmospheric component is equal to the atmospheric scale height (Strobel and Cui 2014). At Titan, the exobase is located approximately at an altitude of 1450 km.

The exosphere has been observed to be highly variable even on relatively short time scales. Figure 1.7 shows exospheric densities for N_2 and CH_4 obtained with the Ion and Neutral Mass Spectrometer (INMS) throughout all the flybys with available data (Strobel and Cui 2014).

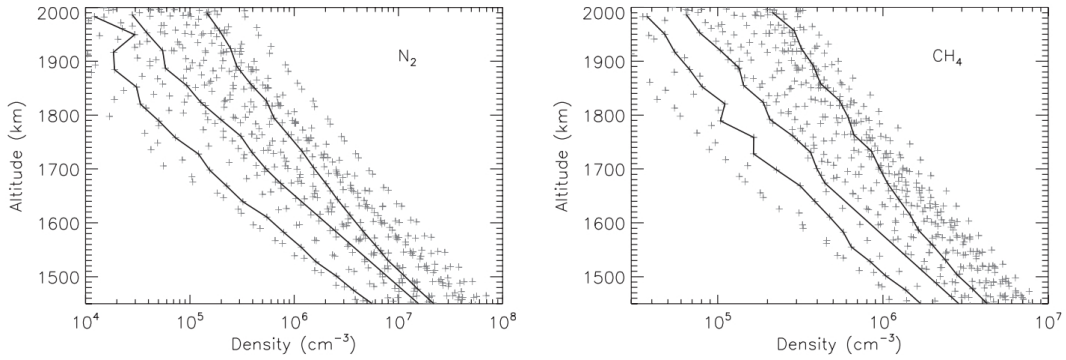

Figure 1.7: Exospheric densities for N_2 (left panel) and CH_4 (right panel) obtained with INMS (from Strobel and Cui 2014). The solid lines show the T55, T56 and T57 flybys which occurred with a similar trajectory and separated only by one Titan day.

In both figures, large variabilities can be observed throughout all the flybys, but even when looking at flybys that occurred within only one Titan day of each other (T55, T56 and T57, solid lines), differences of about one order of magnitude can be observed.

1.2.2 Titan's ionosphere

Different energy sources contribute to the ionisation of Titan's atmosphere, creating a complex structure with a main ionisation layer, located at approximately 1200 km, created by extreme ultraviolet (EUV) photoionisation, and different sub-layers with high temporal variability due to other minor ionisation processes such as magnetospheric ion and electron precipitation, meteorites (at medium altitudes) and cosmic rays (at low altitudes) (Galand et al. 2010, Cravens et al. 2009). In terms of losses, the main chemical sink is dissociative recombination.

Photoionisation is the dominant process on the dayside and is only able to ionise particles at specific heights (down to ∼400 km, Sittler et al. 2009) due to the absorption of UV radiation at higher altitudes. Saturn's magnetospheric plasma plays its major role at higher altitudes (∼1400 km) through electron impact ionisation and charge exchange, while heavy and energetic ions can penetrate below 950 km. Finally, cosmic rays can penetrate much lower with most of their energy being deposited at ∼70 km (López-Moreno et al. 2008).

All these different ionisation processes give place to a dynamic stratified ionosphere with different layers that change altitude depending on a variety of factors such as relative position of Titan with respect to Saturn, solar activity and Titan local time and latitude. Additionally, secondary ionisation caused by a particle produced by primary ionisation (e.g. electron impact ionisation by an electron produced through photoionization) plays an important role, especially at lower altitudes and it was also suggested that plasma transport from the dayside of the ionosphere could be an important factor for the nightside composition (Cui et al. 2010).

Given that the most abundant species in Titan's atmosphere are N_2 and CH_4, it was expected to find these molecules in ionised form in the moon's ionosphere. These are, however, not the most abundant species. Using data from INMS for a nightside flyby (T5), Cravens et al. (2009) demonstrated that Titan's ionosphere is mostly composed of complex species generated by ion-neutral interactions, like $C_2H_5^+$ and $HCNH^+$.

Figure 1.8 shows the vertical profile of the electron density in Titan's ionosphere. The data for the plot was taken by the Cassini radio occultation experiment during different flybys covering different regions of the moon and both the dusk and dawn averages are shown (blue and red curves respectively). The main ionospheric peak at ∼1200 km is clearly visible, with the densities significantly changing between dusk and dawn passages.

1.2.3 Titan's interaction with the surrounding plasma

Titan's interaction with the Saturnian magnetosphere is special in many different aspects. One of them is the fact that Titan spends most of the time inside Saturn's

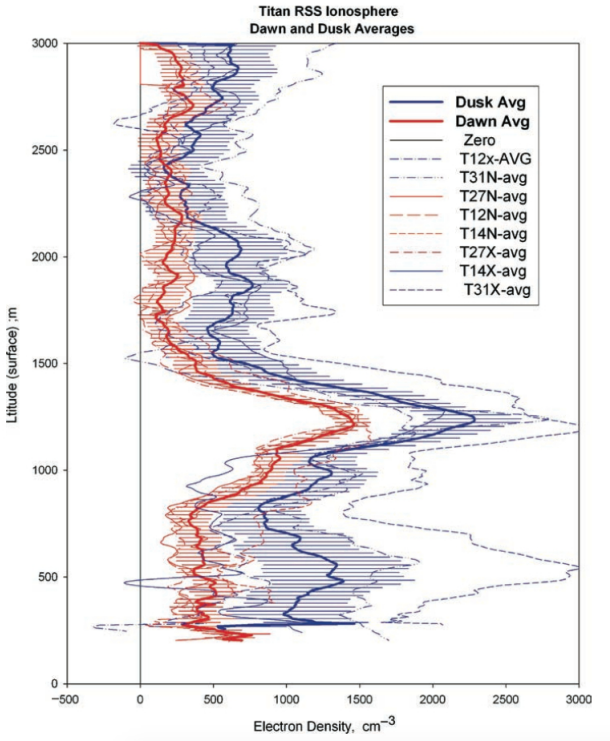

Figure 1.8: Electron density profiles for Titan's ionosphere from radio occultation experiments (from Cravens et al. 2009).

magnetosphere, and that its interaction is hence governed by its position in Saturn Local Time (SLT). It is of particular importance the fact that the magnetospheric wake and the solar wake can vary their relative orientations, giving rise to different types of interactions in relation to the position of the photoionisation and the electron impact ionisation peaks (Figure 1.9).

There are different types of interactions between moons and magnetospheric plasmas, the most common one being that of unmagnetised airless bodies where the planet's corotating plasma directly impinges on the moon's surface where the charged particles are absorbed. These interactions, depending on whether the incoming flux is of subsonic or supersonic nature, will leave a plasma wake that can extend for just a few or several satellite's radii.

Titan has no internal magnetic field but it has a thick atmosphere, so the nature of the interaction is quite different from that of other moons in the Solar System. Many aspects of this interaction have been compared with that of comets, Mars or Venus with the solar wind (Alfvén 1957, Backes et al. 2005, Arridge et al. 2011a).

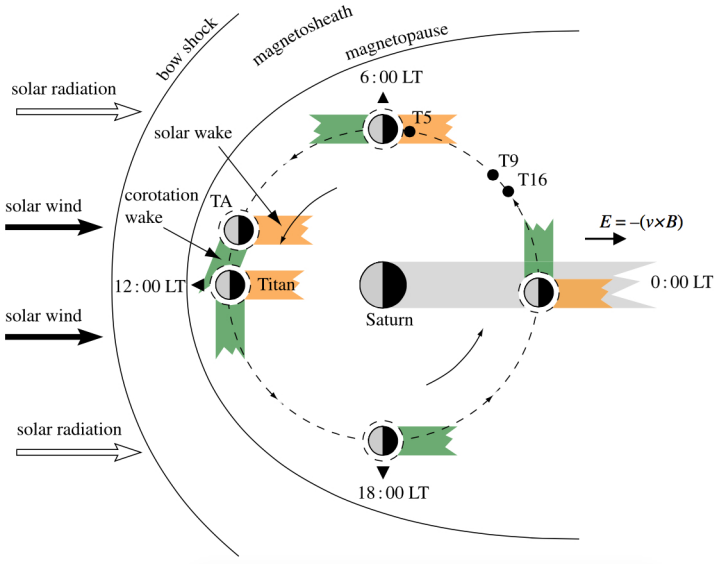

Figure 1.9: Relative position of Titan's solar and ionospheric wakes for different locations of the moon (from Coates 2009).

This is because even though these bodies do not have an internal magnetic field strong enough to create a magnetosphere in a classical sense, the presence of a sufficiently dense atmosphere and ionosphere causes a mass loading of the incoming magnetic field lines. This mass loading process in turn induces currents in the ionosphere that causes the deflection and draping of the field lines creating an induced magnetosphere.

There are, however, some important differences between these bodies that affect the structure of this interaction. Table 1.1 shows typical values for some upstream parameters at Mars, Venus and Titan.

While some parameters, such as the magnetic field magnitude $\bar{B}$ and the magnetic moment $|M|$, are comparable, some others are very different. There are two types of waves that involve magnetic field lines, namely Aflvén and magnetosonic waves, with the first ones traveling along and the second ones across the field lines. In a similar way to sonic waves in a fluid, the relationship between the speed of the flowing plasma and that of the propagation of the waves is termed Mach number.

One of the main distinctions arises from the difference in the Alfvénic and magnetosonic Mach numbers (M_A and M_S respectively). Mars and Venus are immersed in a supersonic and super-Alfvénic flow, whilst the interaction at Ti-

Parameter	Mars	Venus	Titan		
			M'sphere	M'sheath	Solar wind
$\|M\|$ $(T \cdot m^3)$	$< 2x10^{11}$	$< 3x10^{11}$	$< 2x10^{11}$		
n $(10^6\ m^{-3})$		~ 20	0.029	0.5-1.0	0.80 (0.54, 1.52)
$\|\bar{u}\|$ $(km \cdot s^{-1})$	410	~ 400	90	100	520 (540, 630)
$\|\bar{B}\|$ (nT)	2.8	11-12	4.1	< 10	1.4 (1.2, 3.1)
M_A	7-8	7	0.6	0.3-1	24 (16, 13)
M_S	6-7	6	0.5	0.4-0.7	14 (14, 12)
β	2-3	1-2	1.7	0.5-4	6.9 (1.6, 1.6)
T_e (eV)	8	17	130	30-40	1-2
T_i (eV)	11	9	2000	200	1-2

Table 1.1: Upstream flow parameters for Mars, Venus and Titan (from Arridge et al. 2011a).

tan is subsonic and sub-Alfvénic, except when it is located in the magnetosheath (subsonic, possibly super-Alfvénic) or in the solar wind (supersonic and super-Alfvénic).

During the Voyager 1 flyby, even though Titan was located inside the magnetosphere, the flow was reported by Neubauer et al. (1984) to be subsonic ($M_S = 0.57$) and super-Alfvénic ($M_A = 1.9$). Using data from the same flyby, Ness et al. (1982) reported values of 0.5 for both Mach numbers indicating that they can oscillate around one. For this reason, the magnetospheric flow at Titan is sometimes referred to as trans-sonic and trans-Alfvénic.

This means that, unless located in the solar wind, a bow shock is not formed upstream of the moon and thus the unaffected magnetospheric plasma is able to directly interact with the moon's atmosphere. This interaction facilitates the escape of ionospheric and atmospheric particles through a series of escape processes (see Chapter 6 for a more detailed explanation) that led to the prediction, prior to the arrival of Cassini at the Saturnian system, of a neutral Nitrogen torus that has thus far not been found (Smith et al. 2004).

When the incoming magnetospheric plasma carrying a frozen-in magnetic field is mass-loaded with ions from Titan's ionosphere and locally produced ions from the atmosphere (including the creation and further escape of pickup ions, see Chapter 6), the incoming flow and thus the magnetic field lines are slowed down in front

of the moon, causing a draping of the lines as the plasma flows around the obstacle. This creates an induced magnetosphere around the moon and a very special magnetic field configuration that further complicates its interaction with the environment. A sketch of this induced magnetosphere is shown in Figure 1.10.

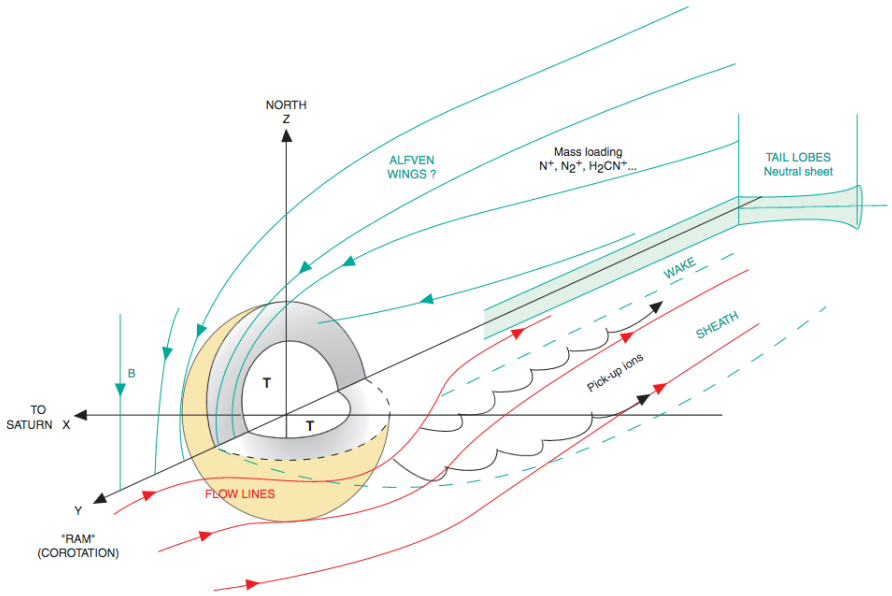

Figure 1.10: Sketch of the induced magnetosphere around Titan (from Blanc et al. 2002).

Analysing data from a magnetosheath flyby (T32), Bertucci et al. (2008) showed that the induced draped field lines remain in the form of what was called 'fossil fields' even after Titan left the plasma environment that originated them. This is a consequence of the difference in the convection time of the field lines in the magnetosphere and in the ionosphere. When the magnetospheric field lines penetrate the moon's ionosphere, their velocity is reduced from about 120 km/s to about 100 m/s, changing the convection time past the moon from a couple of seconds to a few hours. This causes that when Cassini flies through Titan's ionosphere while the moon is located in the magnetosheath, magnetospheric field lines can still be detected (Simon et al. 2015).

The location of Titan in the outer magnetosphere also exposes the moon to plasmoids released after reconnection of tail lines when passing through the midnight sector. Even though the interaction of Titan with a plasmoid has not yet been directly observed, Russell et al. (2008) suggested that the presence of the moon can

actually have an influence on the formation of plasmoids by additional mass loading of the field lines.

In general, even though the role of Titan as a major source of neutrals for the magnetosphere was initially overestimated, the moon still seems to exert some control on the overall structure of the magnetosphere, with the extent of this control still being an active research topic.

In addition to those particularities, the plasma environment surrounding Titan can be highly variable, as shown by Rymer et al. (2009) who divided the different possible magnetospheric environments into four groups, namely lobe-like, magnetosheath, plasma sheet or bimodal. This is a consequence of the current sheet moving up or down according to the external solar wind pressure (Arridge et al. 2008), making it possible for Titan to be located at different magnetic latitudes, even though its orbit lies almost at the equatorial plane of Saturn.

The energetic environment seems to be even more variable. Garnier et al. (2010) tried to find global trends by performing a statistical study of the energetic ions detected by the MIMI instrument and, even though some local time dependency was found, the study was carried out with the data available until the end of 2007, when only 39 dedicated flybys had occurred.

In Chapter 4 of this thesis, a similar study but with significant improved statistics is presented. The results confirm a noon-midnight asymmetry in the ion fluxes that was already reported by Garnier et al. (2010). This asymmetry is not observed in the electron data. When looking at different parameters such as average fluxes or spectral slopes, the overall energetic environment remains a very dynamic one. This implies that, at least until some governing factor is found, the influence of the energetic plasma in Titan's atmosphere needs to be studied on a case-by-case basis.

As mentioned before, different ionisation processes take part in the ionisation of Titan's atmosphere and the subsequent creation of its complex ionosphere. Many of these processes have been studied by analysing the different data sets provided by Cassini (Cravens et al. 2008) or by simulation (e.g. Snowden and Yelle 2014).

One that has so far not been taken into account is the draping of the field lines

caused by the presence of the moon. While thermal plasma tends to be confined close to the equator and its motion be governed by the partial corotation observed at the orbit of Titan, energetic ions and electrons have a field-aligned velocity component that can no longer be neglected. This enables these particles to travel far from the equatorial plane and this, together with the large gyroradius of ions, allows them to reach different locations around the moon in a much more complex way than for the case of thermal plasma.

In Chapter 5, this phenomenon and its ultimate influence in the ionisation rates of the moon's atmosphere are investigated. A combination of data analysis and test particle simulations is used in order to determine the trajectories of energetic ions around the moon and the location where those particles encounter the exobase and deposit their energy. While the contribution of energetic ions to the total ionisation, especially on the dayside, is small compared to photoionisation or electron impact ionisation, the relative differences found indicate that, when studying this ionisation process, the draping of the field lines is something that needs to be taken into account.

Finally, in Chapter 6 the contribution of pickup ions to the loss of mass from the atmosphere to the magnetosphere in the form of pickup ions is investigated. The trajectories of equatorial tail flybys made it possible for previous studies (e.g. Coates et al. 2012) to estimate the total ion losses by measuring the fluxes encountered by Cassini downstream of the moon. The individual contribution of each process, however, remains poorly understood. By taking advantage of a signature left in the data collected by the CAPS instrument by freshly produced pickup ions, the escape region of these ions was constrained and escape rates from a specific species were estimated. The results show that the contribution of this process is small, even though further studies including more species could change these figures.

Chapter 2

Basic plasma physics concepts

2.1 Basic plasma physics concepts

There are several textbooks that deal with the topic of plasma physics from a space physics point of view. The concepts described here were partly taken from Roederer (1970), Kivelson and Russell (1995), Baumjohann and Treumann (1997) and Kallenrode (2004).

Plasma

In simple terms, a plasma, commonly referred to as the fourth state of matter, is a quasi-neutral ionised gas. More formally, for an ionised gas to be classified as a plasma, three criteria need to be met, but before listing these criteria, some other concepts need to be introduced.

Debye shielding and Debye length

In the definition given before, the term quasi-neutral was used. This is because, on a large scale, the number of positive and negative charges in a plasma is the same, giving a net charge of zero.

First, it is necessary to define what large scale means. For this, it is useful to imagine a cloud of ionised gas with neutral net charge where a test charge is introduced. After a short time, particles around the test charge will re-organise themselves in such a way that a shielding effect occurs, creating a sphere of a given radius outside of which neutrality is restored. This radius is the so-called Debye length, and is defined by Equation 2.1, where λ_D is the Debye length, ε_0 is the

vacuum permittivity, k_B is the Boltzmann constant, T_e is the electron temperature (assumed to be the same as the ion temperature), n_e is the electron number density (also assumed to be the same as the ion density due to the quasi neutrality condition) and e is the electron charge.

$$\lambda_D = \left(\frac{\varepsilon_0 \cdot k_B \cdot T_e}{n_e \cdot e^2} \right)^{1/2} \tag{2.1}$$

The first criterion for an ionised gas to be classified as a plasma is that the length at which the different processes occur in the plasma (known as the physical dimension of the system, L) needs to be larger than the Debye length, since inside a sphere of radius λ_D (called a Debye sphere), the plasma will not be neutral anymore, and Coulomb effects will become important.

Plasma parameter

The Debye shielding effect arises from the collective behaviour of particles and thus, it is required that the number of particles inside a Debye sphere, given by Equation 2.2, is large enough to produce it.

$$n_D = \frac{4}{3} \cdot \pi \cdot n_e \cdot {\lambda_D}^3 \tag{2.2}$$

The last two terms of the equation are commonly known as the plasma parameter, Λ, and for an ionised gas to behave as a plasma, this needs to be much larger than 1, it means, $n_e \cdot {\lambda_D}^3 >> 1$. This is the second plasma criterion.

Plasma frequency

When some external force disturbs the quasi-neutrality of the plasma, electrons collectively move to restore neutrality as a consequence of their lower mass. However, due to their inertia, the electrons will stay oscillating around the heavier ions at a specific frequency that will depend on the electron density of the plasma and that is given by Equation 2.3.

$$\omega_{pe} = \left(\frac{n_e e^2}{m_e \varepsilon_0} \right)^{1/2} \tag{2.3}$$

The third plasma criterion is related to the frequency of the plasma. If we take τ_n as the average time between two electron-neutral collisions, for an ionised gas to behave as a plasma, it must be larger than the plasma oscillation period, otherwise collisional interactions will prevail. This can be written as $\omega_{pe} \cdot \tau_n >> 1$.

Guiding centre approximation

If particles are followed for long periods of time compared to the gyroperiod, in some cases it is useful to consider the guiding centre approximation. This approximation implies dividing the motion of a charged particle into a parallel and a perpendicular motion.

If the perpendicular motion is further separated into the gyration about the field line and the drift motion, the combination of the drift and the parallel motion can be regarded as the translation of the centre of gyration of the particle (Equation 2.4).

$$\bar{r} = \bar{r_{\parallel}} + \bar{r_{\perp}} = \bar{r_{\parallel}} + \bar{r_D} + \bar{\omega} = \bar{r_{gc}} + \bar{\omega} \tag{2.4}$$

This approximation can significantly reduce the computational effort when tracing particles if the spatial scale of any changes in the field is much larger than the gyroradius of the particles. By only calculating the guiding centre component of the motion ($\bar{r_{gc}}$), the position of the particle within a distance of a gyroradius can be determined at any time.

2.2 Motion of charged particles in electromagnetic fields

When a neutral particle is placed in an electromagnetic field, the particle's motion will remain unaffected, unless a force of another nature, for instance gravity, acts upon it. If the particle is electrically charged (either positive or negative), the situation changes.

The electromagnetic field surrounding the particle will exert a force on it that will depend both on intrinsic characteristics (charge of the particle) and on external factors (electric and magnetic fields). The force governing this situation is known

as the Lorentz force and is described by Equation 2.5:

$$\bar{F}_L = q(\bar{E} + \bar{v} \times B) \tag{2.5}$$

When analysing the motion, it is useful to separate the effects of the electric and the magnetic fields. For instance, if no electric field is included (E = 0), it can be seen that a charged particle originally at rest (v = 0) will remain at rest. Also, unless otherwise stated, in the following analysis the magnetic field is taken as uniform along the trajectory of the particles.

In order to facilitate the analysis when the initial velocity is non-zero, whatever direction the velocity has, it will be taken as a sum of two components, namely one parallel ($V_{\|}$) and one perpendicular ($V_{\perp}$) to the local magnetic field.

If the initial velocity $\bar{V}$ is along the magnetic field ($V_{\|} = V$; $V_{\perp} = 0$), then the particle will follow the magnetic field line and no force will act upon it. If the original velocity V is perpendicular to the magnetic field ($V_{\perp} = V$; $V_{\|} = 0$), the particle will start to follow a circular path around the magnetic field line, with the centre of the circle (guiding centre) remaining in the same position in space. Finally, if the initial velocity has non-zero parallel and perpendicular components, the path followed by the particle will be a helix, with a motion component forming a circle around the magnetic field line and, at the same time, the guiding centre of the particle moving with a constant speed along the field line (Figure 2.1).

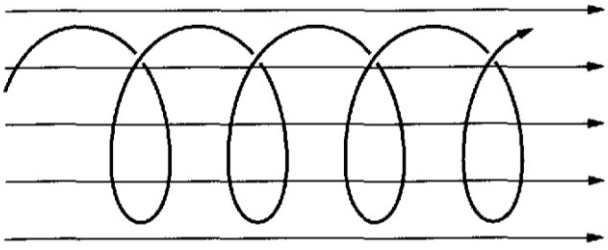

Figure 2.1: Helical motion of a charged particle in a uniform magnetic field (from Baumjohann and Treumann 1997).

If only the effect of an electric field is taken into account, it can be seen that a charged particle will always be accelerated in the direction of the electric field or in the opposite direction, depending on the sign of the charge.

The presence of both an electric and a magnetic field will cause the particle to undergo helical motion with a sideways drift. In the following section, some of the different drifts that a particle can undergo inside a planetary magnetosphere will be reviewed.

Drifts of charged particles in planetary magnetospheres

Most of the time in a magnetosphere, electric fields will be perpendicular to the magnetic field. This is caused by the fact that as soon as a component parallel to the magnetic field arises, the highly mobile electrons will re-arrange themselves in such a way that the effect of the electric field will cancel out. In the common case of an electric field perpendicular to the magnetic field, the drift mentioned in the previous section is known as the E x B drift (Figure 2.2), and it causes the particle's guiding centre to drift in a direction independent of its charge and that is perpendicular to both the magnetic and the electric fields with a guiding centre velocity given by Equation 2.6:

$$v_{gc} = \frac{\bar{E} \times \bar{B}}{B^2} \tag{2.6}$$

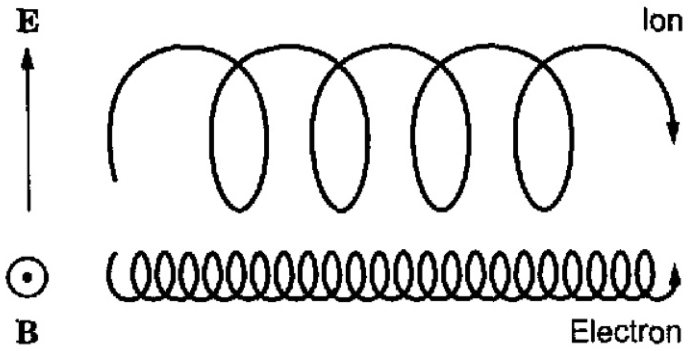

Figure 2.2: $E \times B$ drift for ions and electrons (from Baumjohann and Treumann 1997).

The drift arises from the fact that an ion (electron) will be accelerated (decelerated) when traveling in the direction of the electric field and decelerated (accelerated) when traveling in the opposite direction, leading to temporary changes in the gyroradius of the particle that result in a net drift of its guiding centre.

When analysing the motion of particles in a planetary magnetosphere, drifts

can occur not only due to the presence of an electric field, but also due to inhomogeneities in the magnetic field.

The first of these inhomogeneities is related to the particle's gyroradius. When a charged particle travels along a magnetic field line inside a magnetic field configuration with varying magnitude (such as that of a planetary dipole), its gyroradius will change with the magnitude of the magnetic field following Equation 2.7:

$$r_g = \frac{mv_\perp}{|q|B} \tag{2.7}$$

This will make the particle drift perpendicular the the local magnetic field in a similar way to the process shown in Figure 2.2, only that this time this change is due to the magnetic field gradient and, as shown in Figure 2.3, the direction of the drift will depend on the charge of the particle and will be given by Equation 2.8:

$$\bar{v}_\nabla = \frac{mv_\perp^2}{2qB^3}\bar{B} \times \nabla\bar{B} \tag{2.8}$$

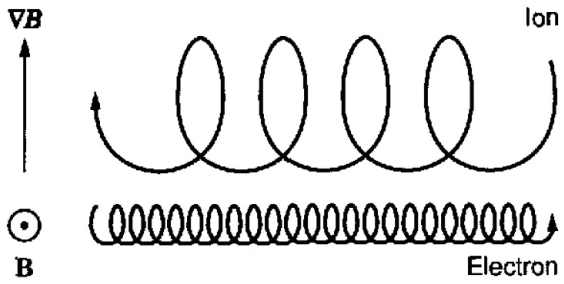

Figure 2.3: Gradient drift (from Baumjohann and Treumann 1997).

First adiabatic invariant: magnetic moment

An adiabatic invariant is a quantity that remains constant when the environment changes slowly with respect to a given parameter. In plasma physics, there are three of these invariants that are related to the motion of charged particles in electromagnetic fields.

The first of these quantities is the magnetic moment. It is related to the gyromotion of a particle in a magnetic field and is defined by Equation 2.9:

$$\mu = \frac{mv_{\perp}^2}{2B} \tag{2.9}$$

where m is the mass of the particle, $V_{\perp}$ is the perpendicular component of the particle's velocity and B is the magnitude of the magnetic field. Notice that, in order for the magnetic moment to remain constant, if the magnetic field magnitude increases, the perpendicular velocity must increase as well. When the total velocity of the particle is constant, e.g. in the absence of an electric field, the parallel component of the velocity must decrease. This can continue to happen until a point where the magnetic field strength is such that $V_{\parallel} = 0$ and then the particle reverses direction of motion. The point in space with this magnetic field magnitude is known as a magnetic mirror point (Figure 2.4).

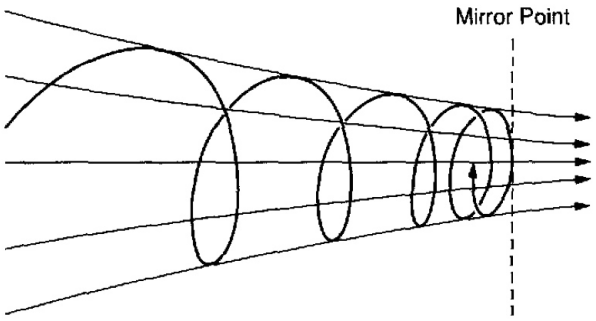

Figure 2.4: Trajectory change due to a mirror point (from Baumjohann and Treumann 1997).

For the first invariant to be valid, the frequency of changes in the field must be smaller than the gyrofrequency of the particle being considered. Otherwise, the path followed by the particle will change before completing a full gyration and the invariance of the magnetic moment will be violated.

Second adiabatic invariant: longitudinal invariant

The magnetic field of a planet, with converging field lines on each magnetic pole, converts the magnetosphere into what is known as a magnetic bottle, where particles can become trapped, bouncing back and forth between the two poles, while its guiding centre drifts azimuthally according to the polarisation of the magnetic field and the charge of the particle due to the gradient drift.

The second invariant is called the longitudinal invariant, and it is related with the drift that a particle undergoes when bouncing between two mirror points. It is defined by Equation 2.10.

$$J = \oint mv_{\parallel}\, ds \tag{2.10}$$

For this invariant, if the frequency of changes in the field is larger than the bouncing frequency, the invariant will be violated and the guiding centre of the particle will not follow a field line. This means that the guiding centre approximation will not hold true anymore.

Third adiabatic invariant: flux invariant

The third invariant is also related to the longitudinal drift of a trapped charged particle, specifically to the magnetic flux enclosed by a particle that completes a full orbit around a planet with an axisymmetric field due to the gradient drift. It is defined by Equation 2.11, where ϕ is the flux enclosed by the particle during one orbit, m is the mass of the particle and M is the magnetic moment of the axisymmetric field.

$$\phi = \frac{2\pi m}{q^2} M = const \tag{2.11}$$

If the time scale at which the field undergoes changes is smaller than the time a particle needs to complete an orbit, this invariant will be violated and thus, after completing one orbit, the particle will have drifted to another drift shell, which is the surface that contains all the locations of a particle's guiding centre while completing an orbit around the central body (Figure 2.5).

2.3 Describing the group behaviour of plasmas

When studying a plasma environment, the single particle behaviour described in the previous section sets a number of limitations that prevent an accurate description of the real motion, mainly due to the lack of self-consistent electric fields created by the simultaneous motion of many particles.

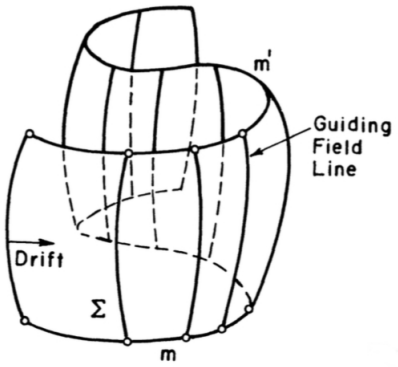

Figure 2.5: Example of a drift shell (from Roederer 1970).

In a magnetosphere, while the magnetic field configuration is maintained over long periods of time by the dynamo process inside the planet, any external electric field will almost instantly cause the electrons to move to restore the neutrality of the plasma. Nevertheless, the motion of charged particles along magnetic field lines, as well as the drifts described, are the origin of self-consistent electric fields that will in turn affect the motion of the same particles that originated them.

For this reason, when studying large amounts of particles (such as the case of the plasma confined inside a planetary magnetosphere), it is important to take into account the collective behaviour of all the particles as well as their interactions with each other.

There are different approaches to studying the collective behaviour of plasmas. Recent reviews on the topic are provided in Ledvina et al. (2008) and Kallio et al. (2011).

2.3.1 Kinetic description of a plasma

The most straightforward way to describe the group behaviour of plasmas is to self-consistently simulate the motion of individual charged particles on a background magnetic field as well as the fields that arise from that motion. This approach is known as particle-in-cell (PIC) and it consists of a particle mover that follows the motion of the particles being simulated and a field solver that consistently calculates the electromagnetic fields. Due to the high computational cost of the PIC methods, their application is usually constrained to small spatial scales.

An alternative approach, called kinetic theory, makes use of probability distribution functions to describe the positions and velocities of plasma particles. A commonly used equation to describe how a plasma distribution function evolves in time is the Vlasov equation. The distribution function of pickup ions at the Earth's moon, Titan and Venus was studied using the Vlasov equation, for instance, by Hartle et al. (2011).

2.3.2 Magnetohydrodynamics (MHD)

Another very useful way to study plasmas is by treating them as conducting fluids. The basic idea of the MHD approach is to combine the equations of fluid dynamics with those of electromagnetism (Maxwell's equations), to account for a fluid that is influenced by electromagnetic fields.

The main strength of the MHD approach is that solving the equations is relatively easy and computationally inexpensive compared to other approaches. This allows MHD simulations to be run in very large spatial domains but has the disadvantage that it cannot resolve processes happening at spatial scales smaller than the ion gyroradius or frequencies higher than the ion gyrofrequency.

There are different types of MHD simulations with different levels of complexity. The simplest one, called ideal MHD, assumes an infinite conductivity of the plasma and thus a perfect frozen-in condition. This approach does not take into account the diffusion of the magnetic field that arises from electron-neutral collisions and cannot describe certain aspects that can be important in some environments such as the reconnection of magnetic field lines.

Prior to the arrival of Cassini at the Saturnian system, ideal MHD simulations were used to study the interaction of Titan with the magnetosphere. Some of the early models include those by Ledvina and Cravens (1998), who studied the interaction under three different combinations of magnetosonic and Alfvénic mach numbers, and Kabin et al. (2000), who compared the interaction at Titan with that of an idealised case.

The impossibility of reconnection happening in ideal MHD can be solved by adding an extra term in the Ohm's law accounting for the finite conductivity. This

approach is called resistive MHD. Still, resistive MHD is a single fluid approach, meaning that the effects from mass loading from different ion species is not taken into account, making it impossible to study local structures and asymmetries.

A 3D resistive MHD model was used, for instance, by Backes et al. (2005) to reproduce the magnetic field data obtained during the first Titan encounter (TA). Their result provided one of the first confirmation by the Cassini mission of the absence of a significant internal magnetic field at the moon.

A more complex approach, multi-species MHD, includes a continuity equation for each ion species being considered. This accounts for the sources and losses of each of them. Still, the bulk velocity of the ions and electrons is assumed to be the same. This means that the Hall effect, which arises from the charge separation, is not accounted for.

The absence of the Hall term in the MHD equations does not allow the existence of ambipolar fields, meaning that the magnetic field is still tied to the plasma flow. This, in turn, makes it impossible for the simulations to account for the asymmetries that arise from a plasma flow encountering an obstacle such as a moon. It is for this reason that the Hall MHD approach includes it by assigning different velocities to the ions and electrons and thus introducing a further term in the Ohm's law.

Ma et al. (2007) used a multi-species Hall MHD simulation to study the wake region based on measurements from the T9 flyby. They found that including the Hall term improves the fitting to the data demonstrating the importance of kinetic effects at Titan. They also identified different regions in the vicinity of the moon where, based on the ion gyroradius at those regions, different approaches might be valid (Figure 2.6). They found, for instance, that the reproduction of the split signature of the tail reported in the literature (e.g. Coates et al. 2012) is beyond the capabilities of the fluid approximation.

The use of a multi-fluid MHD model also enabled the reproduction of the observed fossil fields during the T32 magnetosheath flyby, as reported by Ma et al. (2009).

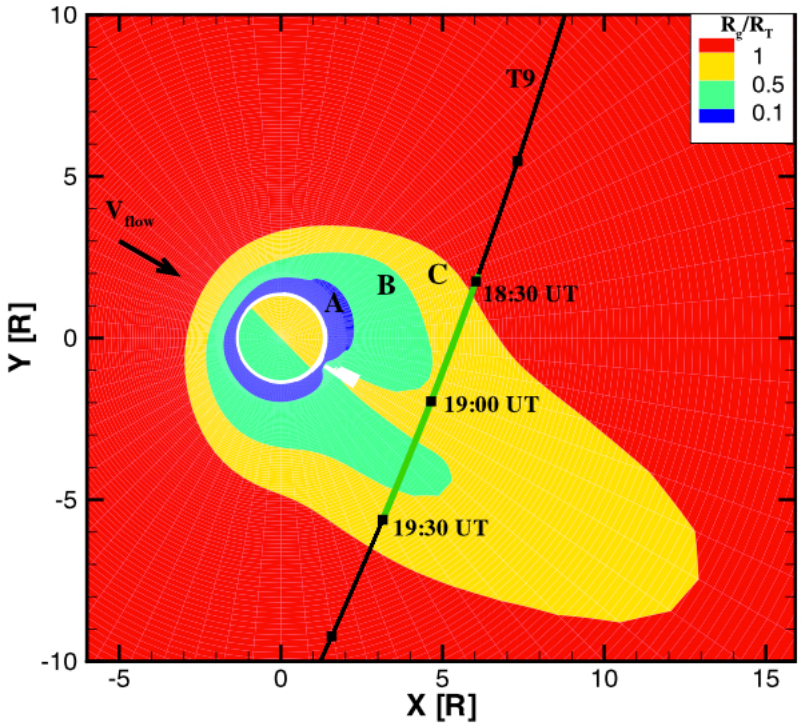

Figure 2.6: Regions close to Titan where different modelling approaches are valid, based on ion gyroradius (less than 0.1 R_T for A, less than 0.5 R_T for B and less than 1 R_T for C (R_T mean 1 Titan radius, 2576 km). In region A, the MHD assumptions are valid. In region B kinetic effects become important and thus the inclusion of the Hall effect is necessary. In region C (and for some processes within region B as well), a kinetic or hybrid approach is more appropriate. (From Ma et al. 2007).

2.3.3 Multi-fluid

For all the MHD approaches just described, only one momentum and energy equation is solved for the electrons and all the ion species considered. The multi-fluid approach solves all the equations separately for each ion and electron component of the plasma, allowing the model to include not only different species but also different populations. For instance, electrons can be simulated as being formed of cold and a hot populations.

Snowden et al. (2007) used a 3D multi-fluid approach to study the importance of gyroradius and heavy ion effects on the structure of the induced magnetosphere. They found that the large gyroradius of pickup ions induces asymmetries due to the directional nature of the corotation electric field (Figure 2.7).

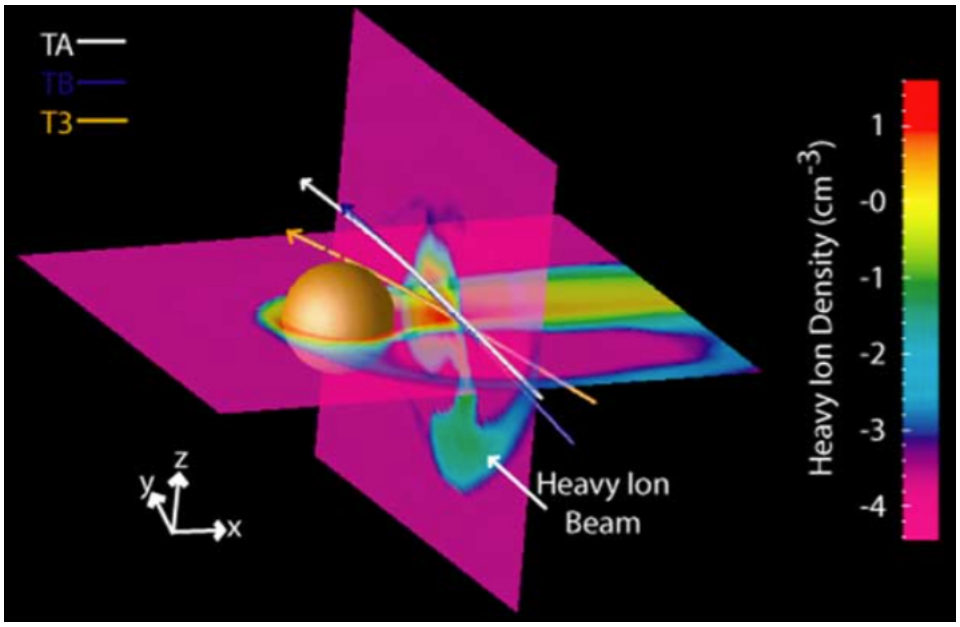

Figure 2.7: Heavy ion density around Titan showing asymmetries arising from gyroradius effects. (from Snowden et al. 2007).

Snowden and Yelle (2014) combined a multi-fluid model with an electron transport model to estimate where magnetospheric electrons deposit their energy with varying relative orientations of the sub-solar point and the corotation direction, finding significant differences for different cases.

2.3.4 Hybrid approach

The hybrid approach can be regarded as an intermediate case between the kinetic and MHD approaches. Given the importance of finite gyroradius effects in many plasma environments, the hybrid approach includes these by treating ions as individual particles and electrons simply as a massless, charge-neutralising fluid.

This approach gives good results when dealing with most of the plasma processes found in the magnetosphere, where the gyroradii of electrons are usually small enough to be neglected when studying their interactions with the different regions and the time scales are larger than the electron gyration period (Müller 2012). The computational resources required are also a compromise between the other two approaches and thus the global simulation domain is usually much smaller than that of MHD or multi-fluid models.

Hybrid simulations have been extensively used to study Titan's interaction with

the magnetosphere of Saturn. Modolo et al. (2007) used a 3D multi-species hybrid model to study the asymmetries observed in the plasma tail of Titan during the T9 flyby. They suggested that these asymmetries arise from the difference in ion and electron production rates and the observed magnetic field structure around the moon during the flyby.

Also for the specific case of the T9 flyby, Simon et al. (2007) used a hybrid code previously applied to the study of the interaction of Mars with the solar wind (Bößwetter et al. 2004). They found that a deviation of the incoming plasma flow of 34° from ideal corotation was able to reproduce the magnetic field signature, even though the magnitude of the distortions are overestimated under this scenario (Figure 2.8). The same code was also used to study the different scenarios that arise from the different relative positions of the corotating plasma and the sunlit face of the moon (Simon et al. 2006).

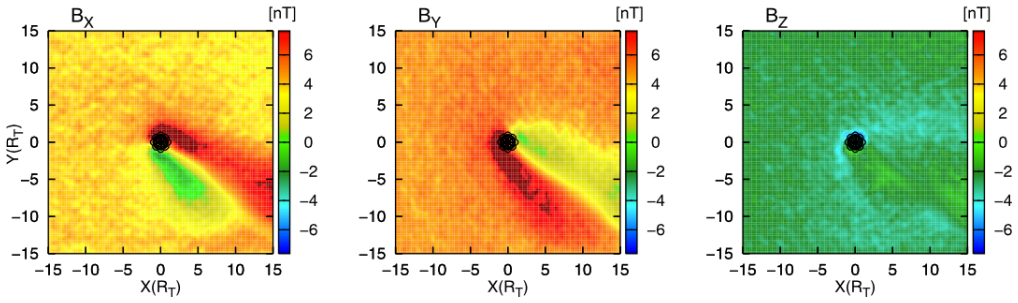

Figure 2.8: Equatorial magnetic field magnitude of Titan from a hybrid code simulation. (from Simon et al. 2007).

Using a combination of data from two of the instruments on board Cassini (the Cassini Plasma Spectrometer, CAPS and the magnetometer, MAG; see Chapter 3 for details on the instruments) during the T15 flyby and a global hybrid model, Sillanpää et al. (2011) showed that the extent of the induced magnetosphere at Titan is very sensitive to the abundance of O^+ ions in the upstream flow. More recently, using the same hybrid code, Sillanpää and Johnson (2015) analysed the effect of ion-neutral collisions in the magnetospheric interaction, showing that they have an important effect on the energy deposition by incoming ions.

The consequences of the complex chemistry of Titan's ionosphere in the mag-

netospheric interaction, specifically the presence of negative ions, was studied using a hybrid code by Ledvina and Brecht (2012). They found that the presence of these ions changes the conductivity of the ionosphere affecting the ion escape rates and the topology of the tail.

Adaptive Ion-Kinetic Electron-Fluid (A.I.K.E.F.)

A.I.K.E.F. is a hybrid code developed at the University of Braunschweig, Germany, aimed at modeling the interaction of magnetised plasmas with Solar System objects (Müller et al. 2011). The code treats ions as individual particles and electrons as a massless neutralizing fluid and has the ability of adapting the simulation grid to the particularities of the body for which the simulations are run.

By treating ions kinetically, the code is able to resolve physical procesess that occur on spatial scales smaller than the ion gyroradius. However, since the electrons are treated as fluid, any process occuring at spatial scales smaller than the electron gyroradius cannot be studied. Similarly, the code can resolve changes occuring in time scales larger than the electron gyroperiod.

Given the above conditions, the following set of equations is self-consistently solved.

$$\bar{E} = -\bar{u_i} \times \bar{B} + \frac{(\nabla \times \bar{B}) \times \bar{B}}{\mu_0 \rho_i} - \frac{\nabla p_e}{\rho_i} + \frac{\eta}{\mu_0} \nabla \times \bar{B} \tag{2.12}$$

$$p_e = p_{e0} \left(\frac{n_e}{n_{e0}} \right)^{\kappa} \tag{2.13}$$

$$\frac{\delta \bar{B}}{\delta t} = \nabla \times \bar{E} \tag{2.14}$$

$$\frac{d\bar{v}_i}{dt} = \frac{q}{m_i} \left(\bar{E}' + \bar{v}_i \times \bar{B} \right) \tag{2.15}$$

$$\frac{d\bar{x}_i}{dt} = \bar{v}_i \tag{2.16}$$

$$\bar{E}' = \bar{E} - \eta \nabla \times \bar{B} \tag{2.17}$$

Equation 2.12 is used to calculate the electric field ($\bar{E}$) taking into account the contribution of both ions ($\bar{u}_i$ and ρ_i are the mean ion velocity and ion charge density respectively) and electrons (p_e is the electron pressure). η is the plasma resistivity, μ_0 the permeability of free space and $\bar{B}$ the magnetic field.

The electron pressure is calculated using the equation of state (Equation 2.13) where p_{e0} and n_{e0} are the initial electron pressure and density respectively, and κ is the adiabatic exponent.

The magnetic field is calculated using Faraday's law (Equation 2.14) and the ion motion is obtained using Lorentz force (Equations 2.15 and 2.16). $\bar{E}'$ is the electric field at the ion position and is related to $\bar{E}$ by Equation 2.17.

The above set of equations is solved for each position and (in the case of ions) for each particle, giving a self-consistent description of the motion of particles and the generated electric fields. As mentioned before, given that the electrons are treated as a fluid and no equation of motion needs to be solved for them, the computational time is greatly reduced, allowing for a larger spatial scale than that achieved by a kinetic approach.

At the same time, by solving the equation of motion for ions, the finite gyroradius effects are taken into account, making it possible to study the asymmetries that arise in the vicinity of objects with radii comparable to the gyroradii of the particles being studied.

A.I.K.E.F. was originally developed to study the plasma environments of Mercury and Titan and, during the Cassini mission, different studies (including this thesis) made use of it to study several aspects of Titan's interaction with Saturn's magnetosphere.

The tail structure observed during the T9, T63 and T75 flybys including the observed split signatures was studied by Feyerabend et al. (2015) using the A.I.K.E.F. (Adaptive Ion Kinetic Electron Fluid) hybrid code (Müller 2012). They conclude that the split signatures are a consequence of a filamentation of the tail created by

light ionospheric species escaping along draped magnetic field lines.

The same A.I.K.E.F. code was used to study the interaction of Titan with the solar wind under the conditions observed during the T96 flyby (Feyerabend et al. 2016). With their simulations, they found evidence of fossil fields as the ones observed during the T32 magnetosheath flyby (Bertucci et al. 2008).

2.3.5 Test particle simulations

Even though test particle simulations are not a way to study the group behaviour of plasmas, when used in combination of field models provided by one of the previously described methods, they are a powerful tool to study specific processes under specific conditions.

By not dealing with the 3D self-consistent description of the electromagnetic fields, the simulation is relatively simple in computational terms. The method basically consists of the integration of the equation of motion (Lorentz force) for individual particles in a static background field. The main disadvantage of the method is that it does not take into account any temporal variation in the topology of the fields so its validity is restricted to processes that occur on timescales shorter than any expected changes in the magnetospheric structure. Additionally, it cannot self-consistently solve changes in the field and thus depends on an already available magnetic field model to propagate the particles upon.

This method has been used to study the generation of energetic neutral atoms (ENAs) in the vicinity of Titan by Wulms et al. (2010) (Figure 2.9). They propagated over 2.8 billion ions on a background field generated by an MHD model from Backes (2005) to study the evolution of the phase space density in order to reproduce all the possible ENA trajectories.

With an output from the A.I.K.E.F. code, Kotova et al. (2015) used a test particle simulation approach taking into account the look direction of the high-energy particle instrument (Magnetospheric Imaging Instrument, MIMI; for details on the instrument, refer to Chapter 3) on board Cassini to replicate the energetic ion and electron measurements obtained in the vicinity of Rhea. They found that even the slight draping of the field lines produced by the tenuous exosphere of the moon

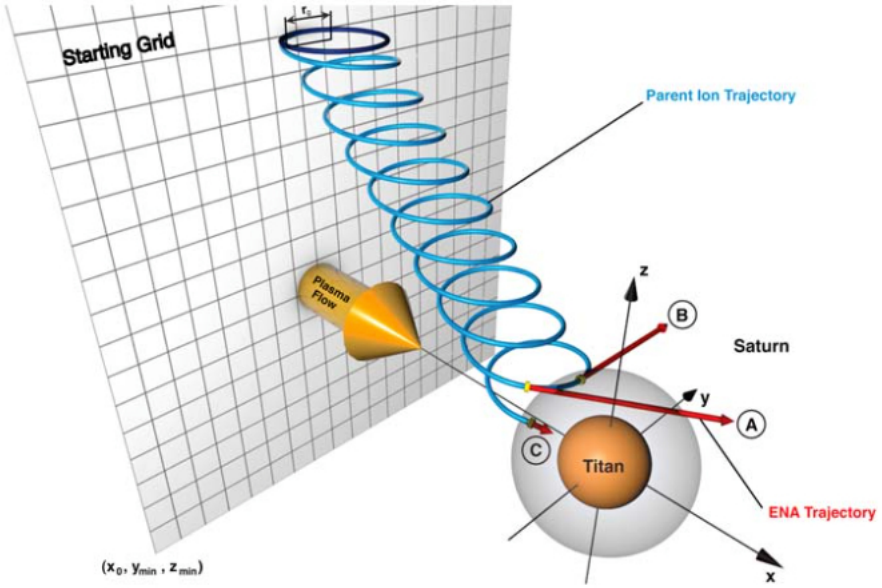

Figure 2.9: Trajectory of test ion in the vicinity of Titan and possible trajectories after the interaction. If the ion exchanges charge with a slow neutral, it will become an energetic neutral atom (ENA) that will subsequently travel on a straight line. (from Wulms et al. 2010).

causes changes in the ion distribution that can be measured by Cassini.

In Chapter 5 of this thesis, an A.I.K.E.F. output for the T9 flyby in combination with test particle simulations is used to study the effect of the draping of field lines around the moon on the local ionisation rates by energetic ions. In that same chapter, a full description of the test particle code developed throughout the duration of this thesis is given.

Chapter 3

Cassini - Huygens

The Cassini orbiter, together with the Huygens probe (both shown in Figure 3.1), were launched on October 15, 1997 and arrived at Saturn on July 1, 2004 when it performed the Saturn orbit insertion (SOI). Huygens separated from Cassini on December 25, 2004 and sampled for the first time with in-situ measurements the complex atmosphere of Titan, landing safely on the moon on January 14, 2005. The data gathered during the descent allowed the creation of a vertical profile of the moon's atmosphere as well as the study of the depth of penetration of different energetic particles.The images captured during the descent revealed a series of interesting features such as methane lakes and a topography similar to that of Earth.

Cassini completed its initial four-year mission in June 2008 and then its first extended mission (the Cassini Equinox mission) in September 2010. At the time of writing of this thesis, the Cassini Solstice mission is ongoing and the spacecraft is planned to be crashed into the planet's atmosphere in a controlled manoeuvre in September 2017. The last stage of the mission, called the 'Grand Finale', comprises a series of unprecedented orbits with periapsis between the inner edge of the ring system and the planet's atmosphere.

3.1 Instrumentation

The Cassini spacecraft is equipped with one of the most complete set of instruments of any planetary orbiter to date. The full instrumentation comprises 12 instruments: 6 remote sensing (between them covering microwave, infrared, visible and ultravio-

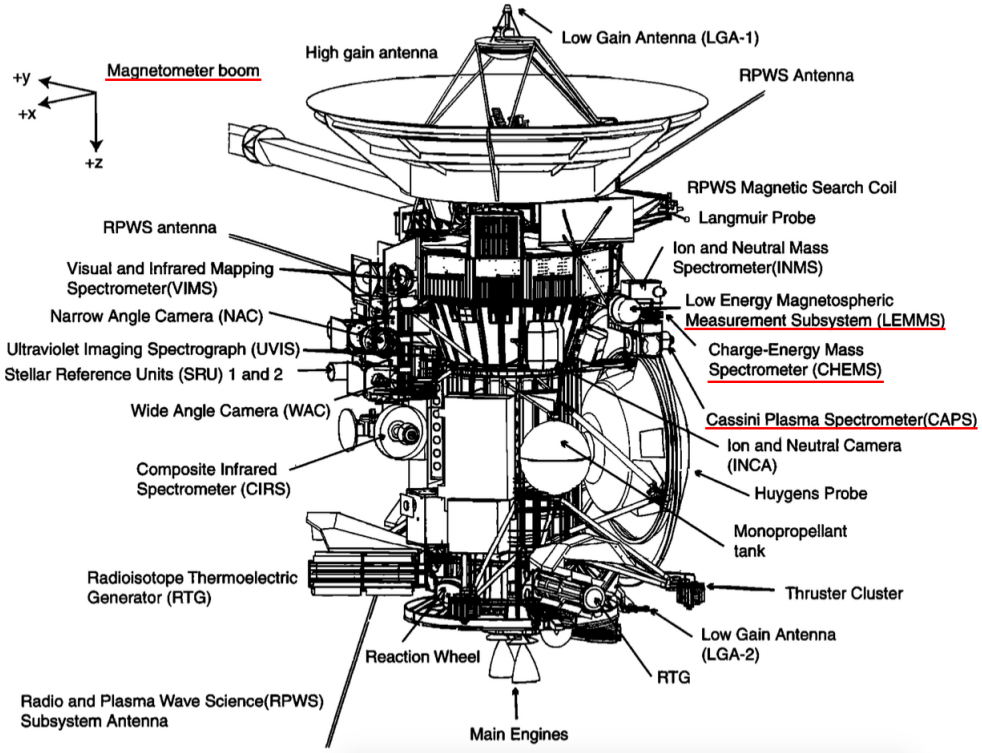

Figure 3.1: View of the Cassini spacecraft showing the different instruments with the Huygens probe attached (from Burton et al. 2001). The instruments used for the studies presented in this thesis are highlighted.

let wavelengths) and 6 in-situ instruments designed to measure fields, particles and waves.

Of special interest for this thesis is the set of instruments dedicated to fields and particles. These instruments were specifically designed to study the different plasma and neutral particle populations and electromagnetic fields present in the Saturnian magnetosphere. For this thesis, data from three of them were used, namely the Magnetometer (MAG), the Cassini Plasma Spectrometer (CAPS) and the Magnetospheric Imaging Instrument (MIMI).

3.1.1 Magnetometer (MAG)

The magnetometer on-board Cassini is an instrument developed by an international team led by Imperial College's Space and Atmospheric Physics Group (Dougherty et al. 2004). With the help of the magnetometer, a detailed study of the internal magnetic field of Saturn as well as its disturbances due to the different environments

inside the magnetosphere and its interaction with the solar wind and the interplanetary magnetic field (IMF) can be undertaken.

The instrument consists of a fluxgate magnetometer (FGM) and a vector helium magnetometer (V/SHM) that can provide both vector and scalar measurements. It is mounted along an 11 m boom (the V/SHM at the end and the FGM in the middle, shown in Figure 3.2) in order to isolate it from any electromagnetic disturbance caused by other instruments and subsystems on-board the spacecraft.

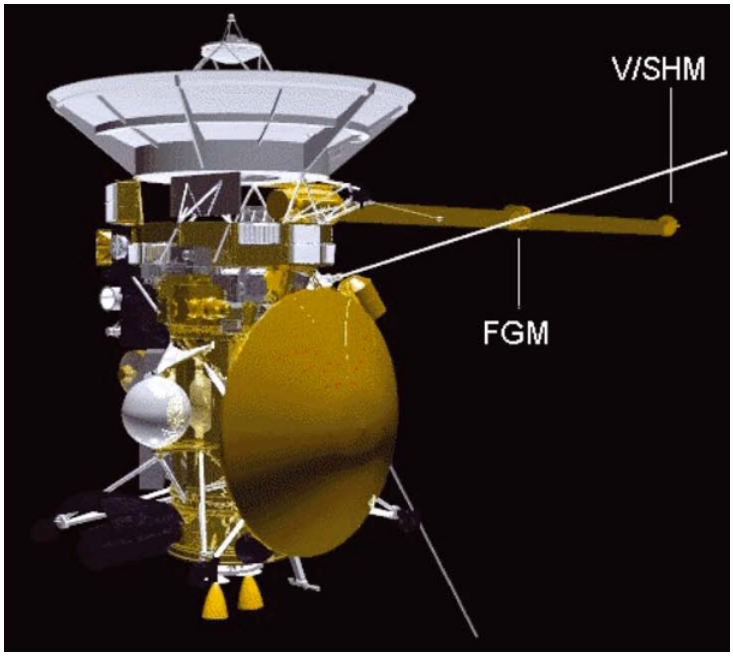

Figure 3.2: Location of the FGM and S/VHM along the magnetometer boom in the Cassini orbiter (taken from Dougherty et al. 2004).

Apart from providing measurement redundancy (in fact, the VHM stopped working on November 18, 2005), the inclusion of two different types of magnetometer facilitates cross-calibration and characterisation of the already mentioned perturbations of the field caused by the spacecraft itself. Additionally, while the FGM has a very wide dynamic range, it is less accurate than the VHM when measuring weak fields.

Table 3.1 lists the main instrument characteristics as taken from Dougherty et al. (2004).

Using magnetometer data, Dougherty et al. (2006) first identified the existence

Parameter	Value
Mass (kg)	
V/SHM Sensor	0.71
FGM Sensor	0.44
Power (W)	
Vector/Vector Mode (FGM + VHM)	11.31
Vector/Scalar Mode (FGM + SHM)	12.63
Dynamic range, resolution	
FGM	$\pm 40\ nT$, $4.9\ pT$
	$\pm 400\ nT$, $48.8\ pT$
	$\pm 10000\ nT$, $1.2\ nT$
	$\pm 44000\ nT$, $5.4\ nT$
VHM	$\pm 32\ nT$, $3.9\ pT$
	$\pm 256\ nT$, $31.2\ pT$
SHM	$256 - 16384\ nT$, $36\ pT$

Table 3.1: Main characteristics of the MAG instrument (from Dougherty et al. 2004).

of an atmospheric plume at Enceladus. The detection was possible due to localised perturbations near the south pole of the moon that were not consistent with the signature that would have been left by the draping of the field lines caused by a global atmosphere. Additionally, the observation of ion cyclotron waves close to the gyrofrequency of water group ions indicated that the moon was a major source of the magnetospheric plasma, something unsuspected before the arrival of Cassini at the Saturnian system.

Specifically for Titan, with the help of the MAG instrument some open questions from the pre-Cassini era were addressed. One of the most important aspects was the determination of an upper limit for the internal magnetic field of the moon, which is so small that for practical matters is treated as non-existent. Using MAG data for the first Titan encounter (TA), Backes et al. (2005) showed that any possible intrinsic magnetic field would have a magnitude which is weaker than the planetary magnetic field magnitude at the position of Titan, which for that specific flyby was of approximately 6.1 nT. Additionally, with the help of a magnetohydrodynamics (MHD) model, the draping of the lines already suggested by Neubauer et al. (1984) caused by the moon's ionosphere was clearly observed.

Using magnetic field measurements during the T32 flyby, the first dedicated

flyby to occur while Titan was located in the magnetosheath, Bertucci et al. (2008) reported the observation of fossil fields that remained above the collisional ionosphere from the moment when Titan was still inside the magnetosphere. Also using MAG data, Bertucci et al. (2015) reported a Mars-like interaction of Titan with the solar wind during the only close flyby during which Titan was observed to be outside the Saturnian magnetopause.

On the 26th of December, 2005, Cassini flew through Titan's tail at the equatorial plane (T9). The geometry of the flyby (a more detailed explanation of this flyby is given in Chapter 3) allowed the study of the magnetic structure of the mid-range tail. Bertucci et al. (2007) reported a highly asymmetric tail with two well-defined lobes and a corresponding current sheet in the centre.

For the studies presented in this thesis, the magnetic field data from the MAG instrument provided the pitch angle information that is crucial for the study of freshly produced pickup ions that is presented in Chapter 4. It also helped with the definition of Titan's interaction region when studying the energetic environment at Titan's orbit (4) and the energy deposition by energetic ions (Chapter 5). Additionally, the magnetic field data is critical to produce the hybrid code outputs that are used as background field during the test-particle simulations presented in Chapters 5 and 6.

3.1.2 Cassini Plasma Spectrometer (CAPS)

One of the main objectives of the Cassini mission was to study the different thermal ion and electron populations of the Saturnian magnetosphere as well as how Titan, the icy moons and the rings interact with it (Young et al. 2004). CAPS is an instrument formed of three subsystems, namely the Electron Spectrometer (ELS), the Ion Mass Spectrometer (IMS) and the Ion Beam Spectrometer (IBS) (since only CAPS/ELS and CAPS/IMS data are used in this thesis, the details of the CAPS/IBS instrument are not covered here). The instrument was developed by a wide group of institutions, led by the Southwest Research Institute (SWRI, Young et al. 2004) and with the Mullard Space Science Laboratory (MSSL) leading the development of CAPS/ELS.

Figure 3.3 shows a schematic of the CAPS instrument with the location of the three mentioned subsystems.

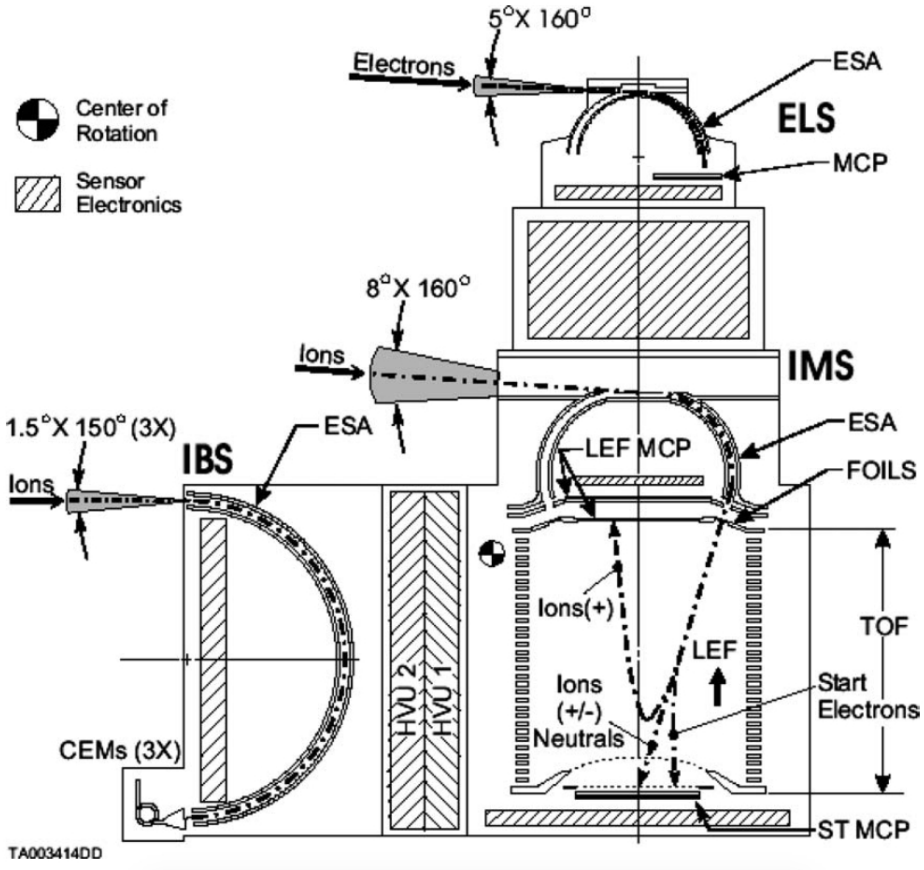

Figure 3.3: Side view of the Cassini CAPS sensor showing the key elements and the corresponding fields of view (from Young et al. 2004).

The whole instrument is mounted on a platform capable of rotating by $\sim$180° around the spacecraft's Z axis (Figure 3.1). The rate and range of rotation can be adjusted according to specific needs during the mission like for instance the observation of a given target or the study of Titan's ionosphere during a flyby.

The three sensors are based on electrostatic analysers (ESA) that guide particles of a given mass per charge (m/q) or energy per charge (E/q) to electron-multiplier detectors. Each of them, however, has specific characteristics.

Electron Spectrometer (ELS)

CAPS/ELS is a hemispherical top-hat ESA that can detect electrons with energies from 0.6 eV to 28250 keV. This range has an important overlap with the

MIMI/LEMMS detector, providing a full coverage for Cassini, without gaps, from 1 eV to 832 keV (only taking into account the low-energy telescope from MIMI/LEMMS, see below).

The instrument has two hemispherical concentric ESA plates that guide the incoming particle until it impacts on an annular micro-channel plate (MCP). The sensor can detect the energy and the elevation angle of the incoming particle. The energy is discerned by changing the voltage of the inner plate. For a given voltage, electrons with a higher energy than those intended to be detected will have an initial velocity when entering the instrument that will make them impact the outer plate, while those with a lower energy will be deflected in excess, thus impacting the inner plate.

CAPS/ELS has 64 energy levels with an energy resolution of $\Delta E/E \sim 0.17$. The integration time per energy level is of 31.25 ms, for a total energy sweep time of 2 s. Of this integration time, 25% is allocated to the readout of the accumulated data and the switching of the voltage for the next energy level.

In addition to the described energy scan mode (called Sweep Table A), three other modes were pre-programmed in the instrument. Sweep Table B is designed to scan 32 energy levels between 1 eV and 1 keV. Sweep Table C also scans 32 energy levels, but this time with energies from 1.8 eV to 22 keV; this mode provides a wide energy range with a better time resolution (1 s for the whole scan) by sacrificing energy resolution ($\Delta E/E \sim 0.36$). Finally, a fixed-step mode is available, specifically designed for calibration purposes or in case a single energy level is needed, providing the maximum time resolution.

The detector consists of 8 different anodes, each of them with a field of view of 20° by 5.24°. The elevation angle is determined by the anode at which a given electron impacts the detector, giving the instrument a total elevation angle coverage of 160°. Figure 3.4 shows a schematic of the 8 anodes and how the entrance elevation angle maps to them.

The elevation angle is defined by the grid located between the exit of the ESA and the MCP detector. Table 3.2 shows the main characteristics of the instrument.

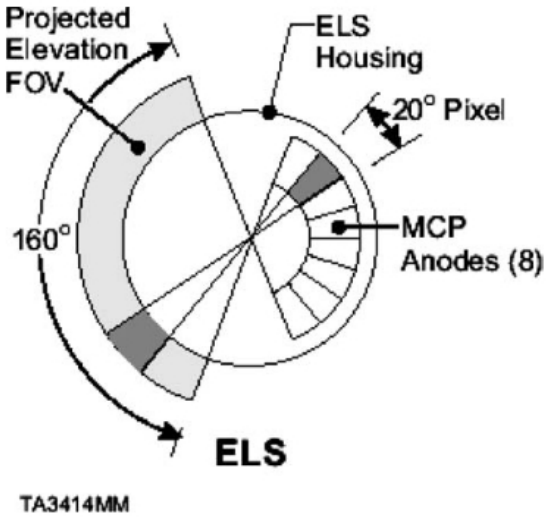

Figure 3.4: Mapping of elevation angle to ELS anodes (from Young et al. 2004).

Parameter	Value
Energy range (eV)	$0.6 - 28250$
Resolution $\Delta E/E$ (%)	16.75^a
Field of view (°)	$5.24^a \times 160$
Angular resolution (°)	$5.24^a \times 20$
Analyser constant measured on FM at 960 eV (ev/V)	6.31
Geometric factor^b (cm^2 sr eV/eV)	
Dynamic range, resolution	
(1) per 20° anode	8×10^{-4}
(2) per complete FOV	6.4×10^{-3}

Table 3.2: Main characteristics of the CAPS/ELS instrument. ^{a} Value from simulation. ^{b} Based on nominal MCP voltage setting. (From Young et al. 2004).

Ion Mass Spectrometer (IMS)

CAPS/IMS has the ability to measure velocity distributions of major ion species with energies ranging from 1 to 50280 eV as well as measuring the atomic and molecular composition of the different plasma populations encountered during the mission, with an atomic resolution of $M/\Delta M \sim 70$.

To achieve its science objectives, CAPS/IMS combines the energy discrimination provided by a toroidal ESA with the mass discrimination from the time-of-flight (TOF) analyser based on carbon foils. The carbon foils provide the timing signal to estimate the TOF of the particle being measured from the moment it enters the instrument until it hits the MCP (a schematic view is shown in Figure 3.3).

Once ions exit the ESA, they are accelerated by a negative potential making them go through the carbon foils at the entrance of the TOF analyser. Inside the analyser, a linear electric field (LEF) is maintained. This LEF will guide particles with different charge and energy in different ways.

Then, two different sensors can be reached, namely the straight-through (ST) and the LEF MCPs. Due to the LEF applied, the electrons generated in the carbon foil will be guided towards the ST MCP, providing the 'start' signal for the TOF measurement. Additionally, negative ions, neutrals and positive ions with energy higher than 15 keV will reach the ST MCP as well. Ions with E $<$ 15 keV will in turn be reflected and finally reach the LEF MCP. A particle hitting any of the two MCPs will trigger a 'stop' signal. The time difference between the start and stop signals is then used to get the m/q information.

For the 'stop' signal to be valid, it must be coincident with the corresponding 'start'. Otherwise, no m/q information is derived. This causes the measurements with species discrimination to be less sensitive and thus the instrument provides measurements without any m/q information that are much more sensitive.

In terms of energy, CAPS/IMS covers 63 energy steps (changing voltage in on the inner plate of the ESA) every 4 s and, similar to CAPS/ELS, it has 8 anodes that provide information on the elevation angle of the incoming ions.

Table 3.3 shows the main characteristics of IMS.

Parameter	Value
Energy range (eV)	$1-50280$
Atomic resolution $M/\Delta M$	70
Field of view (°)	8.3×160
Angular resolution (°)	8.3×20

Table 3.3: Main characteristics of the CAPS/IMS instrument.

Due to a malfunctioning in spacecraft power systems related to the instrument, CAPS was switched off in June 2012, after the T83 flyby. Data collected by CAPS until that moment proved to be invaluable in many aspects.

Thomsen et al. (2010) provided an overview of plasma parameters in the Saturnian magnetosphere using moment calculations and compositional analysis from

data obtained by the CAPS/IMS instrument. They found that, even when they are highly variable, the density of the species included in the analysis (H^+, W^+ and m/q = 2, interpreted as H_2^+) can in general be organised by L-shell and magnetic latitude. They also found that the H_2^+/H^+ ratio varies with L-shell distance with a peak near Titan's orbit, suggesting that the moon might be an important source of these ions in the outer magnetosphere. In terms of corotation velocities, they found that these are typically lower than full corotation for all the L-distances analysed with flow directions varying with SLT location.

Using CAPS/ELS and CAPS/IMS data, Teolis et al. (2010) found signatures of O_2^+, CO_2^+ and O^- ions during a close flyby of Rhea, leading to the first detection of an exosphere at Saturn's second-largest moon. More recently, using data from the Ion and Neutral Mass Spectrometer (INMS, Waite et al. 2004), Teolis and Waite (2016) confirmed the existence of a similar exosphere at another Saturnian moon, Dione. In the same paper, they also reported seasonal variations of the exosphere at both moons.

Specifically for Titan, using electron data from the CAPS/ELS instrument, Rymer et al. (2009) provided a characterisation of the plasma environment at Titan's orbit. This characterisation included four main categories, namely plasma sheet, lobe-like, bi-modal and magnetosheath. A better explanation of these categories is provided when studying the energetic environment at Titan's orbit in Chapter 5 of this thesis.

During the T9 flyby, the same split signature in the magnetic tail of Titan described using MAG data was observed using the CAPS/ELS instrument and reported by Coates et al. (2007b). Figure 3.5 shows an electron spectrogram from CAPS/ELS (top panel), and a singles data (no ion composition) spectrogram from CAPS/IMS (second panel) and calculated moments (namely electron density, ion density and ion velocity, three bottom panels) for the T9 flyby.

The moments are calculated using Equations 3.1 and 3.2 where $f(\bar{v})$ is the velocity distribution function (Thomsen et al. 2010).

$$n = \int_{all\ \bar{v}} f(\bar{v})\, d^3\bar{v} \tag{3.1}$$

$$\bar{V} = \frac{1}{n} \int_{all\ \bar{v}} \bar{v} f(\bar{v})\, d^3\bar{v} \tag{3.2}$$

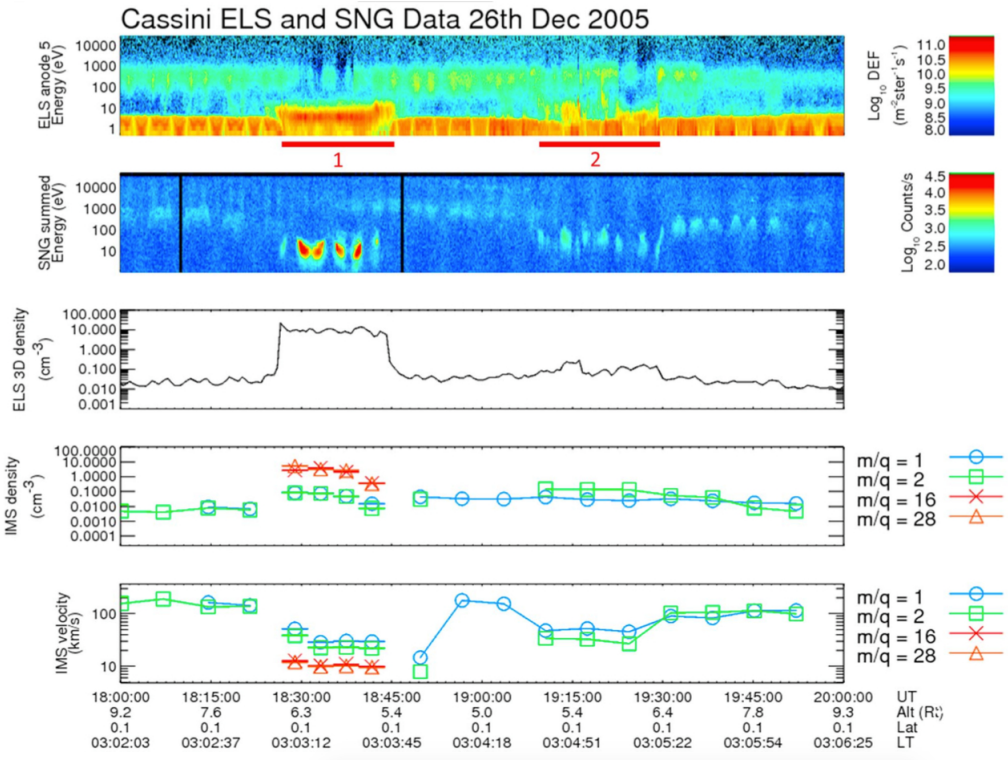

Figure 3.5: Electron and ion data from the CAPS/ELS and CAPS/IMS instrument on-board Cassini (from Coates et al. 2012).

The split signature can be observed in Figure 3.5 in both regions where the electron and ion energies and densities clearly change (marked with red lines 1 and 2 in top panel). Also, during both events, they reported the presence of ionospheric photoelectrons (electrons with a characteristic kinetic energy that result from the ionisation of neutral molecules by sunlight), visible in the top panel in the form of a population with peak energy of 21.4 eV. By calculating moments (ion densities and velocities) and looking at ion composition, they were also able to estimate ion losses through polar wind escape at 7 tons/day. A comparison of these escape rates with those from the ion pickup process is made in Chapter 6.

A remarkable discovery at Titan from the CAPS/ELS instrument was the pres-

ence in the ionosphere of heavy negative ions with molecular masses of up to 13800 amu. The discovery was first reported in Coates et al. (2007a) and a more detailed analysis of the molecular masses and their relation with the altitude of detection was presented by Wellbrock et al. (2013).

In Chapter 6, the production of pickup ions as well as their contribution to the atmospheric mass loss is investigated. For this, a complete survey of all the available ion data from the CAPS/IMS instrument is undertaken. Additionally, the plasma environment classification based on CAPS/ELS data made by Rymer et al. (2009) is used for the analysis of the results presented in Chapters 3 and 5.

3.1.3 Magnetospheric Imaging Instrument (MIMI)

While CAPS is an instrument designed to measure the distribution of plasma with relatively low energy (below 50 keV), Saturn's magnetosphere is also populated by energetic ions, electrons and neutrals (commonly known as energetic neutral atoms or ENAs). ENAs are generated when a high energy ion undergoes charge exchange with a slow neutral resulting in the creation of a slow ion and a fast neutral. Since they are unaffected by electromagnetic fields, after being created ENAs follow a linear trajectory making it possible to detect them and use them for remote sensing purposes.

MIMI is an instrument capable of performing remote sensing of ENAs as well as in-situ measurements of ion distributions, composition and charge state (Krimigis et al. 2004). The instrument is composed of three detectors, namely the Low Energy Magnetospheric Measurement System (LEMMS), the Charge-Energy-Mass Spectrometer (CHEMS) and the Ion and Neutral Camera (INCA). It was designed by a group of Universities and research institutions around the world with the Johns Hopkins University / Applied Physics Laboratory (JHU/APL) leading the development of the instrument as a whole and involving collaboration from the Max-Planck Institute for Solar System Research (MPS), leading the development of MIMI/LEMMS. Since no data from the MIMI/INCA instrument was using during the development of this thesis, the details for that instrument will not be presented here.

Low Energy Magnetospheric Measurement System (LEMMS)

MIMI/LEMMS consists of two oppositely directed sets of detectors with different fields of view (FOV) and energy ranges. The low-energy end has an aperture angle of 15° and is designed to measure ions with energies above 30 keV and electrons between 15 keV and 1 MeV. The high energy end is designed to measure high energy ions (1.5 - 160 MeV/N) and electrons (0.1 - several tens of MeV). The field of view of this end is of 30°.

Table 3.4 lists the ion (A0-A7) and electron (C0-C7) channels of the MIMI/LEMMS instrument that are used in this thesis.

Telescope	Channel	Species	E (keV)	Channel	Species	E (keV)
LE	A0	Ions	27-35	C0	Electrons	18-40
LE	A1	Ions	35-56	C1	Electrons	27-48
LE	A2	Ions	56-106	C2	Electrons	41-60
LE	A3	Ions	106-255	C3	Electrons	56-100
LE	A4	Ions	255-506	C4	Electrons	92-183
LE	A5	Ions	506-805	C5	Electrons	175-300
LE	A6	Ions	805-1600	C6	Electrons	265-550
LE	A7	Ions	1615-4000	C7	Electrons	510-832

Table 3.4: Ion and energy channels of the low end (LE) telescope of MIMI/LEMMS (with data from Krupp et al. 2009).

The instrument is looking into the -y direction and is mounted on a turntable capable of rotating about the y-axis (x-z plane) of the spacecraft. This was intended to provide angular distributions of ions and electrons with the possibility of 4π coverage when the spacecraft rolls about the z-axis. The rotating system was switched off due to mechanical issues on the 2nd of February, 2005. Fortunately, the operations team was able to further move MIMI/LEMMS to a position that avoids spacecraft obscuration, specifically pointing 77.45° away from the $-$z direction, as shown in Figure 3.6.

Figure 3.7 shows a schematic of the instrument showing the two ends as well as the position of the detectors inside and Figure 3.8 shows a simulation for the low-energy end showing sample trajectories of energetic ions and electrons as well as the position of the detectors.

Once charged particles enter the low-energy telescope, an inhomogeneous

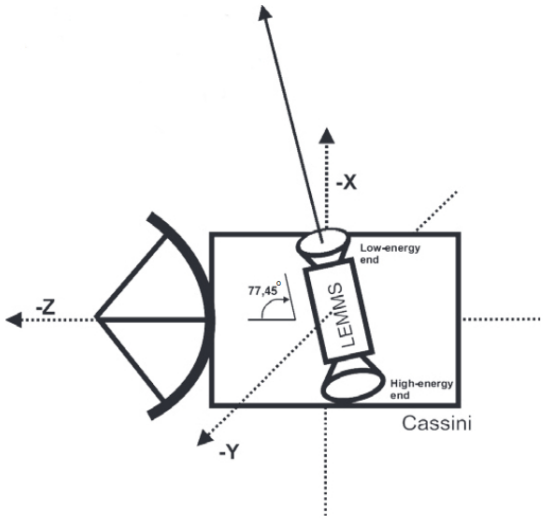

Figure 3.6: Position and look direction of the MIMI/LEMMS instrument after the turntable stopped working (from Krupp et al. 2012).

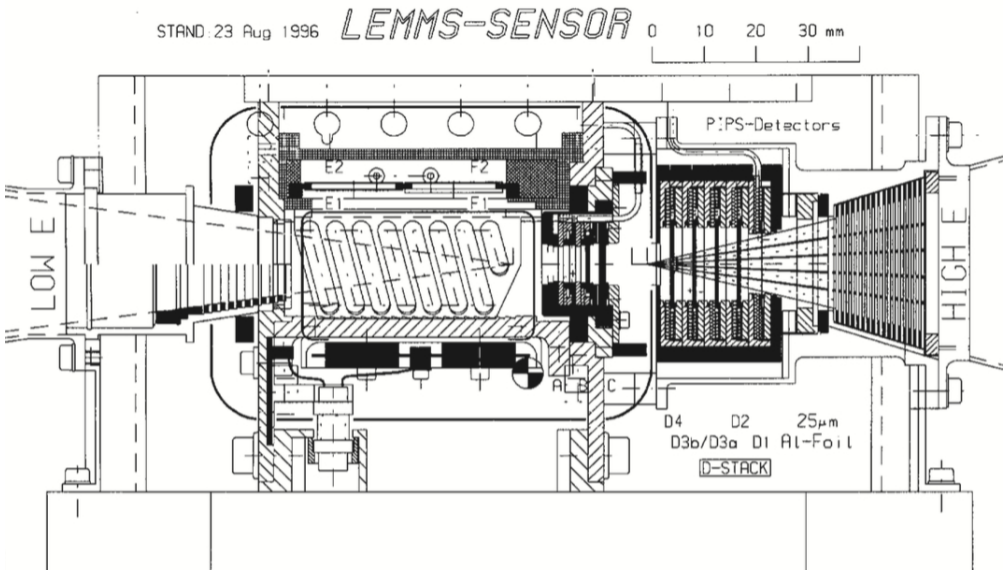

Figure 3.7: Side view of the Cassini MIMI/LEMMS sensor showing both (high- and low-energy) ends. The detectors are labeled as E1, E2, F1 and F2 for low-energy electrons and A and B for low-energy ions. The high-energy end consists of a stack of detectors labeled D1, D2, D3a, D3b and D4 (from Krimigis et al. 2004).

magnetic field guides ions and electrons in different directions, causing the ions to reach the A and B detectors and the electrons the E1, E2, F1 and F2 detectors. The specific detector that each particle will reach depends on the incident energy and entrance angle. The opening angle of the entrance collimator of the low-energy

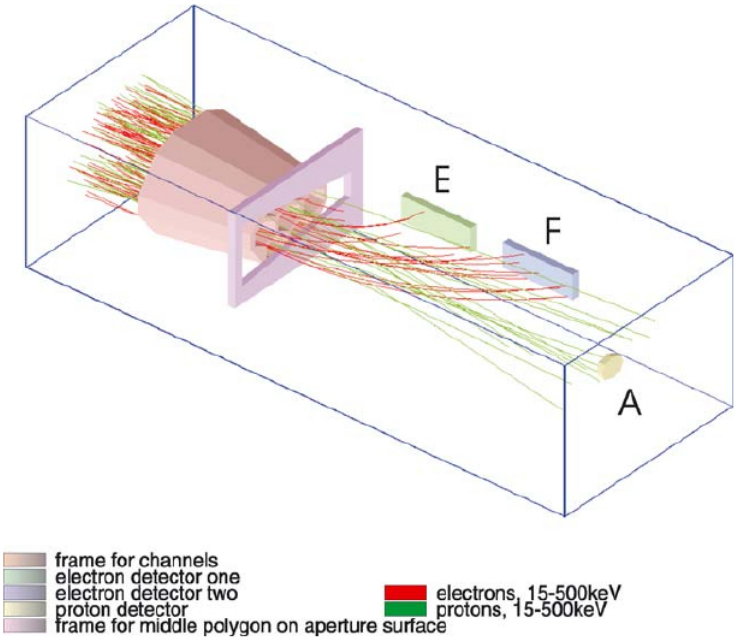

Figure 3.8: Simulated sample trajectories of energetic ions and electrons inside the low-energy end of the MIMI/LEMMS instrument (from Krimigis et al. 2004).

telescope is 15°.

The high-energy end consists of a stack of five detectors (D1, D2, D3a, D3b and D4). In front of the detectors, an aluminum foil is placed in order to prevent the entrance of light as well as low-energy ions and electrons.

Charge-Energy-Mass Spectrometer (CHEMS)

Designed to obtain 3D distribution functions and ion compositions, MIMI/CHEMS is a combination of an electrostatic deflector, serving as a UV trap and an energy per charge filter, and TOF vs. energy measurements. After a particle of a given energy enters the instrument, the TOF between the start and stop detectors, separated by 10 cm, is measured and, by measuring the residual energy of the particle when it reaches a solid state detector, the particle is identified.

Figure 3.9 shows a schematic of the instrument. In the same way as with the CAPS/ELS and CAPS/IMS instruments, a voltage applied in this case to both plates guides particles with a given m/q towards the detector. Once the particles exit the deflection analyser, they pass through a thin carbon foil that generates secondary electrons that impact the 'Start MCP'. This gives the starting signal for the TOF

measurement. Then, the particle travels a distance of 10 cm until it hits the detector, emmitting another electron that reaches the 'Stop MCP'. The speed of the ion is then calculated by the time difference between the 'start' and 'stop' signals.

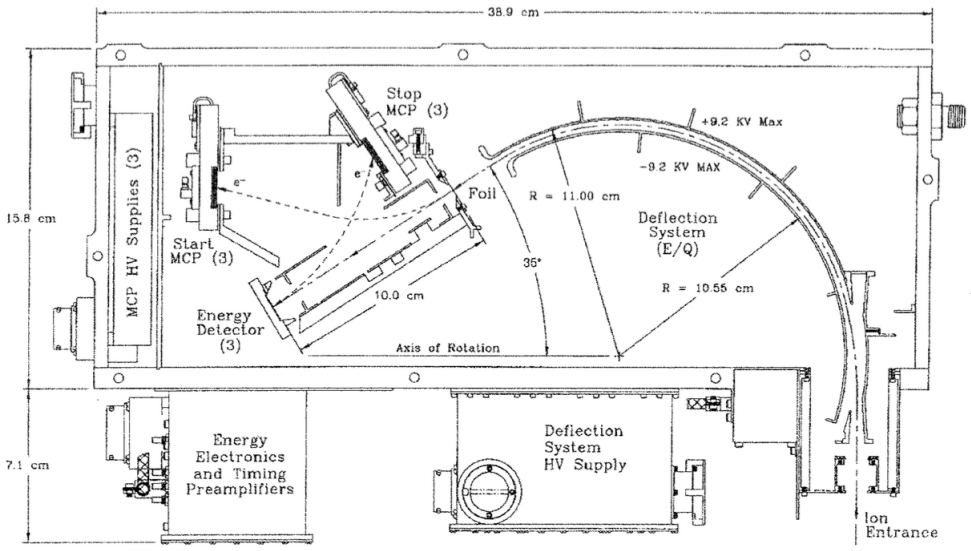

Figure 3.9: Schematic of the MIMI/CHEMS instrument (from Krimigis et al. 2004).

The detector measures the residual energy of the ion and with the available data (residual energy, time of flight and m/q), the mass, charge and incident energy of the ions can be determined.

The instrument has three independent TOF telescopes, each of them covering 53° in polar angle. In terms of azimuthal angle, each telescope has an acceptance of 4°. This large coverage in polar angle (159° in total) gives MIMI/CHEMS the ability to cover most of the 4π solid angle when the spacecraft rolls about the z-axis.

Table 3.5 lists the main characteristics of the instrument.

Component	Values
TOF Measurement	Three independent telescopes with 53° FOV each
	Flight path: 10.0 cm
	Min. TOF: 6 ns
	Max. TOF: 523 ns
Energy Measurement	Electronic threshold: 26 keV
	Maximum energy: 2455 keV

Table 3.5: Main characteristics of the MIMI/CHEMS instrument.

The inclusion of a high-energy particle instrument on Cassini allowed the

spacecraft to perform the most detailed analysis of radiation belts other than Earth. Already during Saturn's orbit insertion (SOI), the MIMI instrument provided an insight into the interaction of the main rings with energetic particles, showing that the radiation belts have an abrupt edge that coincides with the outer edge of the main rings (Krimigis et al. 2005, André et al. 2008). These early works also reported a nearly-equatorial confinement of the energetic plasma in the plasma sheet.

The existence of radiation belts at Saturn was already detected by the pre-Cassini flyby missions Pioneer 11 and the Voyagers 1 and 2 (Van Allen 1984). The corresponding energetic particle population was found to be located typically inside 6 R_S (Gombosi et al. 2009). Using the high energy ion channels of MIMI/LEMMS, Roussos et al. (2008) reported the discovery of a transient radiation belt, based on a series of sudden increases in the energetic ion intensity close to Dione and Tethys.

At Titan, the ENA emissions detected by the MIMI/INCA instrument were used to study the interaction of Titan's exosphere with the Saturnian magnetosphere (Garnier et al. 2007). Using data acquired during the first Titan flyby (TA), they confirmed the existence of asymmetries in the structure of the exosphere arising from finite gyroradius effects.

By taking advantage of the remote sensing capabilities of MIMI/INCA, Brandt et al. (2012) showed that the H_2 exosphere of Titan extends to an altitude of $\sim$50000 km. With a combination of remote sensing observations from MIMI/INCA, in-situ measurements from MIMI/LEMMS and an atmospheric model, Smith et al. (2009) were able to estimate energy deposition rates vs. altitude in Titan's atmosphere.

Using data from the MIMI/CHEMS instrument, Sergis et al. (2007) analysed the energetic particle pressure distribution at different locations of the Saturnian magnetosphere, specifically for low-latitude regions within an L-shell range of 5 to 20 R_S. They found that the plasma β increases with radial distance up to a maximum of $\sim$ 1 at L $\sim$ 13, with O^+ ions contributing more than 50% of the total pressure, thus confirming the existence of a ring current at Saturn. They found, however, that the ring current is highly variable, with a strong influence from injection events.

More recently, MIMI/CHEMS data also led to the observation of seasonal vari-

ations of mass 28 ions (Christon et al. 2014) and the discovery of ion species that had never been observed in the Saturnian magnetosphere before such as Fe^{+} (Christon et al. 2015).

In Chapter 4 of this thesis, a long-term survey of the energetic ion and electron data collected by the MIMI/LEMMS instrument is carried out to characterise the energetic environment at Titan's orbit. In Chapter 4, data from the MIMI/CHEMS instrument are used to obtain the incoming fluxes for the calculation of ionisation rates in Titan's atmosphere.

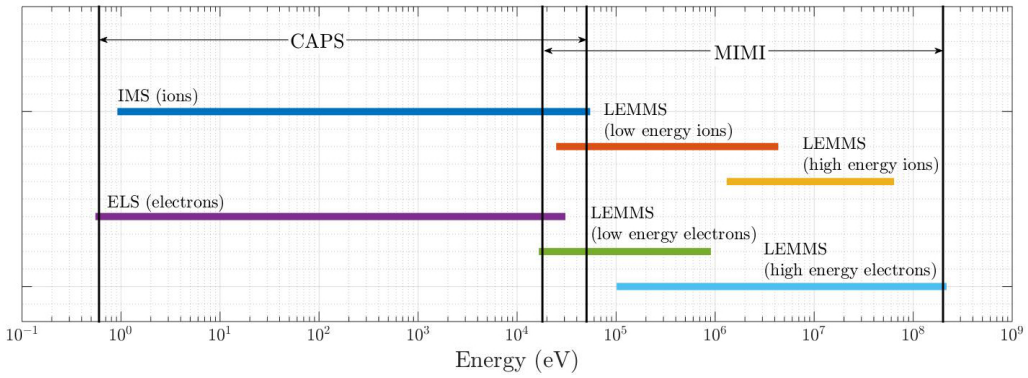

Figure 3.10: Combined energy coverage of the CAPS and MIMI instruments on-board Cassini.

The combination of the data provided by the CAPS and MIMI instruments provides an excellent coverage of the energy ranges of the plasma populations that can be encountered in Saturn's magnetosphere and Titan's ionosphere, as shown in Figure 3.10.

This wide energy range allowed the study of different processes such as the precipitation of energetic ions into Titan's atmosphere and the subsequent ionisation of atmospheric particles as well as the production of pickup ions that are observed in the low energy range.

Chapter 4

Energetic plasma environment at Titan's orbit

In this chapter, the energetic magnetospheric environment outside the interaction region of Titan is studied in order to characterise it and study its dependence on different factors such as SLT, position of the moon inside the magnetosphere and solar wind activity.

There have been some attempts to characterise the energetic environment at Titan's orbit, with Garnier et al. (2010) looking at energetic ions using the MIMI/LEMMS detector and energetic neutral atoms (ENAs) using the MIMI/INCA instrument. For the ions, they analysed data from the four lowest energy channels (A0 to A3) of LEMMS, covering energies from 27 to 255 keV for the close flybys and orbit crossings until January 2008. They focused their study on average fluxes and pitch angle distribution, finding higher fluxes in the dayside when compared to the nightside magnetosphere and a quasi-isotropic pitch angle distribution.

They also looked at ENA images corresponding to H atoms with energies from 24 to 55 keV and concluded that the observed variability in emission is linked to magnetospheric variability, with the exosphere being relatively stable.

The effect of the magnetospheric environment on Titan's ionospheric densities has been studied using Langmuir probe measurements by Edberg et al. (2015). Analysing data from the first 110 Titan flybys, they found enhanced electron densities in the altitude range of 1600 to 2400 km during the flybys when Titan was

located in the night sector. They also observed an increase in electron densities due to the location of Titan with respect to the magnetospheric current sheet. In general, they attributed the changes in electron density to changes in the pressure balance between internal and external sources.

4.1 Dataset

For this study, ion and electron data collected by the MIMI/LEMMS instrument on-board Cassini are used. The data correspond to all the dedicated flybys and Titan's orbit crossings from the first flyby (TA, 26th October 2004) until the end of 2015, with T114 being the last flyby included (13th November 2015). This gives a total of 114 close flybys and 189 orbit crossings which represents a significant increase in the statistics (192% for the flybys and 472% for the orbit crossings) when compared to the study from Garnier et al. (2010).

For each flyby or orbit crossing, all the data obtained within a time window of ± 3 hours from closest approach (CA) was used.

The definition of orbit crossings (also referred to as passes throughout the chapter) used in this study is similar to the one used by Smith and Rymer (2014). All the data obtained close to the equator at distances between 19 and 21 R_S were used. In terms of vertical distance from Titan's orbit, a margin of 1 R_S was used.

In terms of energy coverage, the ion channels A0 to A7 were used, while for electrons channels C0 to C7 were used. This gives an energy coverage of 27 keV to 4 MeV for ions and 18 to 832 keV for electrons (Krupp et al., 2009). The higher energy channels were not considered since in general the contribution of the particles detected by them to the overall energy flux is relatively low.

Since the interest lies on the magnetospheric environment, during the flybys the data obtained within the region where the presence of Titan affects the surrounding environment, from now on referred to as the interaction region, was not taken into account. In order to decide where the interaction region starts and ends, a visual inspection of all the 114 flybys was carried out. For this, the already mentioned ion and electron channels were used. Additionally, magnetic field data from the

MAG instrument were also considered. Figure 4.1 shows an example of how the interaction region for a specific flyby (T5 in this case) was defined.

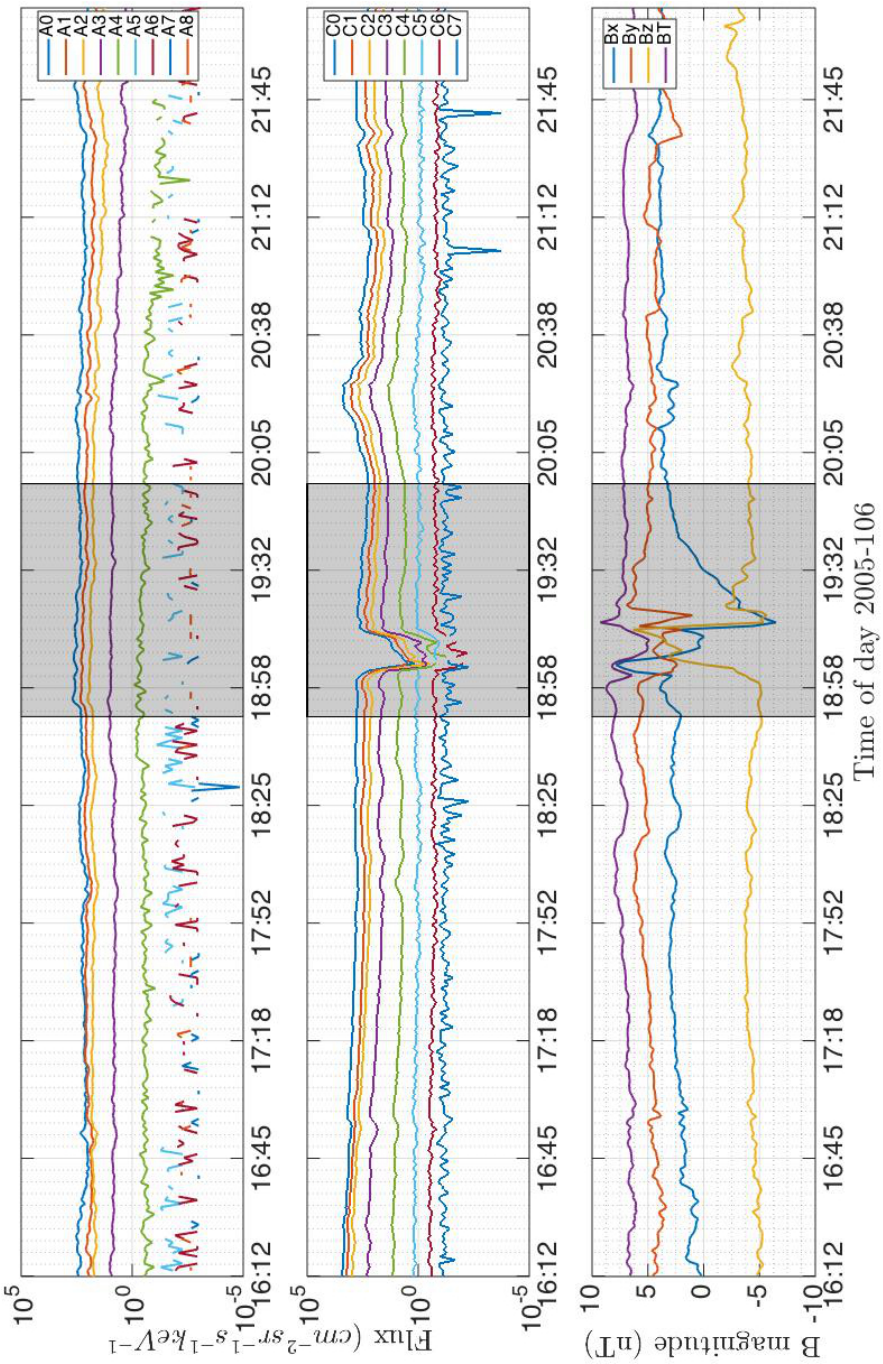

Figure 4.1: Ion (A0 - A8 channels, top panel), electron (C0 - C7 channels, middle panel) and magnetic field data (bottom panel) during the T5 dedicated flyby. The grey boxes in the middle indicate the selected interaction region that was left out during the analyis presented in the text.

The basic criterion for considering the data as obtained outside the interaction region is that no disturbance is present in any of the ion or electron channels. The most affected channels are usually the electron channels as it can be appreciated in the second panel (C0 - C7 channels), where a depletion is detected right after 18:58 UT. Given the high variability of the plasma environment, some dynamics can be observed close to the interaction region, like the increase in fluxes detected for the lowest energies electron channels between 20:05 UT and 20:38 UT but, since the variation is well detached from the main depletion at closest approach, it is assumed to not be related to the presence of the moon and is thus taken into account for the data analysis.

The inclusion of the magnetic field data is to make sure that small variations in the ion or electron data are not overlooked. In Figure 4.1, for instance, even though the disturbance in the electron data seems to be over at around 19:20 UT, the end of the interaction region is defined when the magnetic field data stabilises itself, close to 20:05 UT.

4.2 Relationship between thermal and energetic ion populations

Rymer et al. (2009) classified Titan's environment in four different categories based on thermal electron data from the CAPS/ELS instrument. The four categories they identified were plasma sheet, lobe-like, magnetosheath and bi-modal (Figure 1.1). Figure 4.2 shows sample spectra for these four environments.

According to the definition given in Rymer et al. (2009), plasma sheet encounters are characterised by a relatively dense population of high energy electrons with peak energy between 120 and 600 eV, lobe-like encounters have similar energies but much lower densities, magnetosheath encounters have lower peak energy but much higher densities (corresponding to the shocked solar wind plasma) and bi-modal encounters exhibit two distinct electron populations with different energies with the highest energy population being similar to that of the plasma sheet or lobe-like encounters with a lower density than that of the low energy population. The lowest

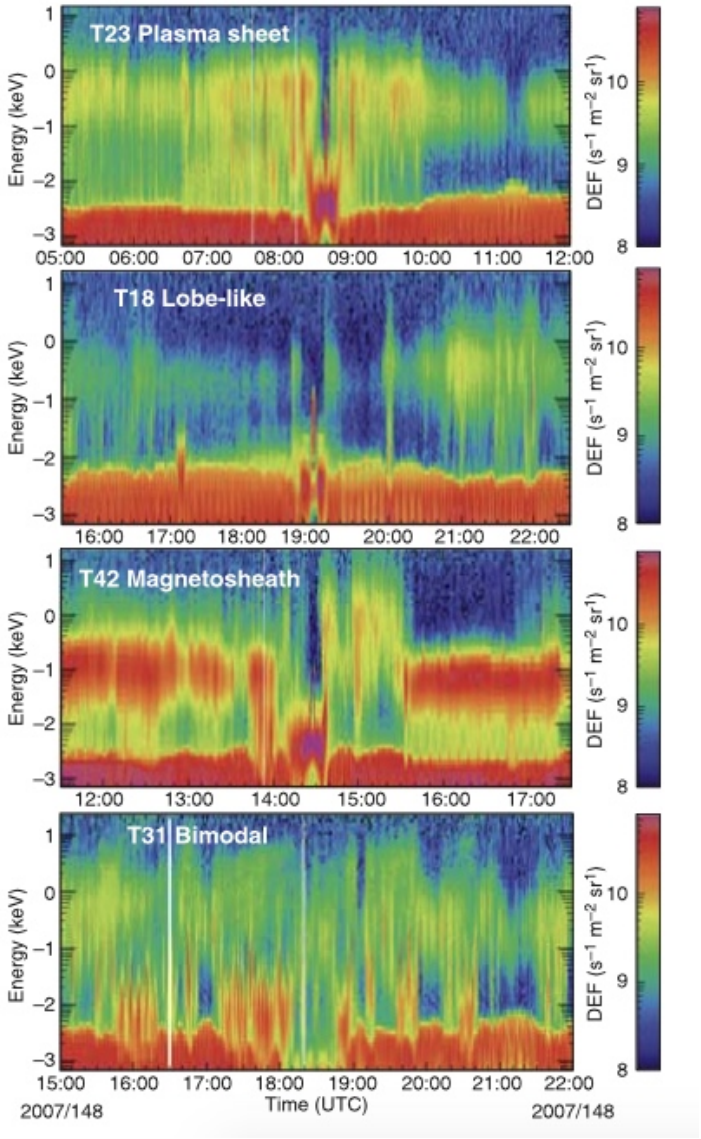

Figure 4.2: Sample electron spectra for the four categories identified by Rymer et al. (2009) while classifying Titan's environment using CAPS/ELS (taken from Rymer et al. (2009)).

energy population seems to correspond to local pickup from the distributed neutral cloud.

When the classification was made, Titan had been found twice in a magnetosheath-like environment (T32 and T42) and, even though it was accepted that if the solar wind dynamic pressure were high enough Titan could be located in the unshocked solar wind, this had not yet been observed. The study was extended to include all the flybys and orbit crossings with available CAPS data and was

reported in Smith and Rymer (2014).

By the time of this writing, another magnetosheath encounter has been identified (T85, Edberg et al. (2013)) and, additionally, Titan was encountered once in the solar wind (T96, Bertucci et al. (2015)). The detection of Titan in the unshocked solar wind introduces a new classification that is used in this study. Since all the remaining encounters are planned to happen with Titan far from noon SLT, it seems unlikely that any of these conditions will be repeated during the remaining time of the Cassini mission.

In this section, the relationship between the thermal environment described in Rymer et al. (2009) and Smith and Rymer (2014) and the energetic ion and electron environment is studied. Average fluxes and spectral indices of the data detected by the A0 to A7 and C0 to C7 channels are analysed and compared to the classification already mentioned. For this reason, during this section data until the last flyby with CAPS data (T83, 12th May 2012) plus T85 (magnetosheath flyby) and T96 (solar wind flyby) are taken into account.

The particles with the lowest energies will be the most affected by the magnetospheric environment since they follow more closely the field lines. This means that particles with higher energies will be less confined to the equator by centrifugal forces. Because of this, special emphasis is given to the lowest energy channels (A0, 27 - 35 keV for ions and C0, 18 - 40 keV for electrons) when looking at the average fluxes.

Figure 4.3 shows the average fluxes from the lowest energy ion channel for all the flybys mentioned above, organised by the plasma environment at which Titan was located according to the classification by Rymer et al. (2009) or Smith and Rymer (2014).

Even though an evident overlap exists between the different classifications, lobe-like encounters seem to exhibit the lowest high-energy ion fluxes. Magnetosheath fluxes seem to be in general higher than plasma sheet ones, but the overlap is significant. From all of them, the highest fluxes are detected during the solar wind flyby, something that might be expected since the fact that the magnetopause

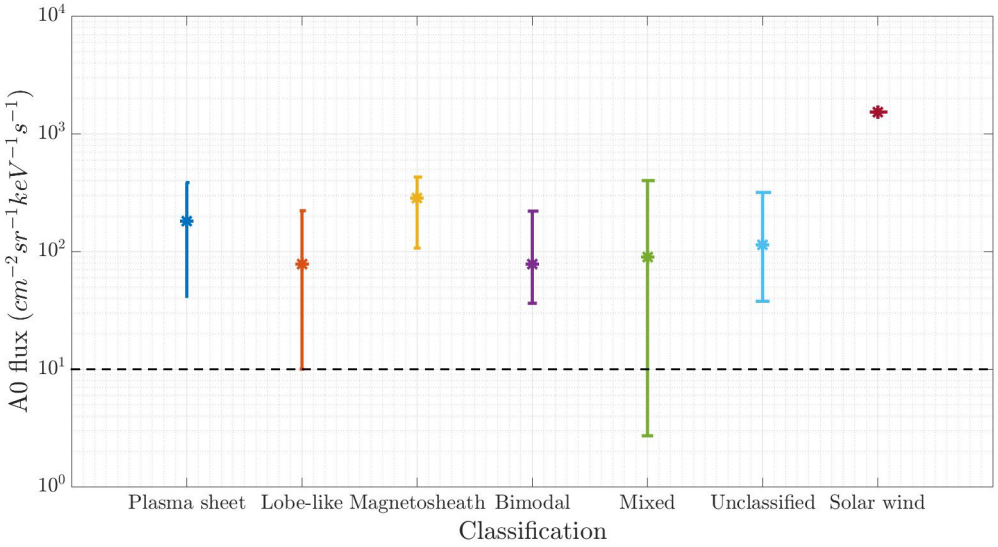

Figure 4.3: Average fluxes for the A0 ion channel (27-35 keV) at each of the plasma environment classifications from Rymer et al. (2009). The horizontal dashed line shows the background value for the A0 channel.

was much closer to the planet than usual indicates fast solar wind containing hot plasma, so the distribution extends to the tens of keV range, with both energetic H^+ and He^{++} ions contributing to the A0 signal.

Figure 4.4 shows the same type of plot but for the lowest energy electron channel. Here, the overlap is much more prominent, with even the solar wind encounter presenting fluxes similar to the lowest ones measured for magnetosheath encounters.

Apart from the solar wind encounter, the electron fluxes remain relatively stable with average values between 200 and 600 $cm^{-2}sr^{-1}keV^{-1}s^{-1}$, showing that the plasma environment does not affect the motion of energetic electrons in any appreciable manner.

In general, energetic ions seem to be affected by the magnetospheric environment in which Titan is encountered, even though no clear distinction can be made between the fluxes encountered during plasma sheet and lobe-like flybys. In the case of electrons, the relationship cannot be established for any of the classifications, a consequence of their much higher mobility compared to ions. This mobility allows them to move farther from the equator, where the flyby data are collected.

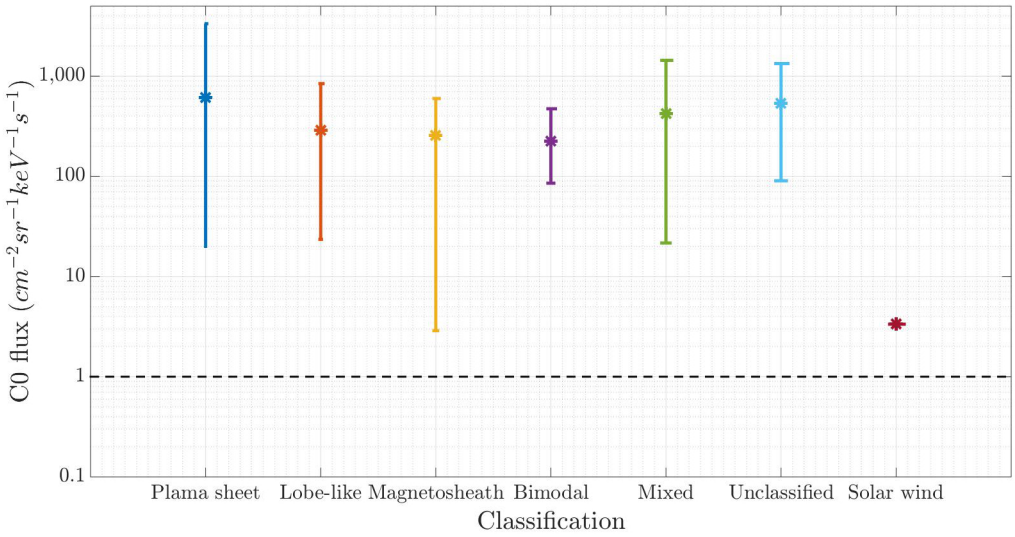

Figure 4.4: Average fluxes for the C0 electron channel (18-40 keV) at each of the plasma environment classifications from Rymer et al. (2009). The horizontal dashed line shows the background value for the C0 channel.

Region	Ions (A0)			Electrons (C0)		
	Min.	Avg.	Max.	Min.	Avg.	Max.
Plasma sheet	41.6	182	322.4	19.8	610.2	3342.2
Lobe-like	10.0	78.1	222.6	23.5	290.6	844
Magnetosheath	106.9	283.6	429.8	2.9	255.9	598.3
Bimodal	36.4	78.6	220.9	85.5	224.2	472.9
Mixed	2.7	90.1	401.4	21.6	426.4	1438.4
Unclassified	37.9	114.8	318.2	90.3	536.8	1337.4
Solar wind	-	1536	-	-	3.3	-

Table 4.1: Minimum, average and maximum A0 and C0 fluxes (in $cm^{-2}sr^{-1}keV^{-1}s^{-1}$) for the different plasma environments as classified by Rymer et al. (2009).

Table 4.1 lists the minimum, maximum and average ion (A0 channel) and electron (C0 channel) fluxes found for each region, as plotted in Figures 4.3 and 4.4.

Different plasma environments can affect particles with different energies in a different way. By performing a statistical analysis of energetic ions using the MIMI instrument, Dialynas et al. (2009) found that H^+ particles appear to be adiabatically heated while being transported throughout the magnetosphere, whereas O^+ particles appear to be heated locally. For the case of H^+ ions with energies between 30.7 keV and 2.3 MeV, they found a slow monotone decrease in spectral index with

increasing L-shell distance with a value of about 2.5 to 5 at Titan's orbit (20 R_S). For the case of O^+ ions, a constant but highly scattered distribution of values close to 5 was obtained for all L-shell distances. Based on this, the spectral slopes of a given species can also help characterise the local energetic environment.

In order to describe the middle and high energy ion spectra at the Earth's magnetosphere, Vasyliūnas (1968) introduced the so-called Kappa distribution, which basically consists of a Maxwellian-like distribution with the high energy tail modified to decrease according to a power law. Here, a modified version presented by Dialynas et al. (2009), given by Equation 4.1 is used, where E is the energy, kT is the ion temperature and γ_1 is the spectral index, which determines the slope of the high energy tail.

$$j = C \cdot E[E + kT(1+\gamma_1)]^{-(1+\gamma_1)} \tag{4.1}$$

With this in mind, spectra for all the available flybys and passes were analysed. In order to account for the magnetospheric variabilities close to Titan, eight different locations, four before and four after closest approach, were sampled and, at those locations, a modified Kappa distribution function was fitted to the data. The eight sampled locations during the TA flyby are shown in Figure 4.5 as an example.

One of the fits is shown in Figure 4.6, specifically for the case of the T5 flyby. The plot shows the data points from the ion channels (A0 - A7) for the eight data points (DP1 - DP8). During the fit, the four channels with higher energies were at background level. This situation arises quite often and thus more weight is given to the lowest energy channels (A0 to A3 in this case).

Additionally, the fits within a flyby can change according to the fluxes on the different channels at each of the eight selected position. In the example from T5, only considering the γ_1 coefficient, the values range from 1.93 for DP5 (data point right after CA) to 3.36 for DP2 and, while some of them are well constrained, with a variation of less than 1 for a confidence level of 95%, for some the variation can be as large as 30. The main factor controlling this variation seems to be the ability of the fitting routine to properly bound the value of the second coefficient, kT.

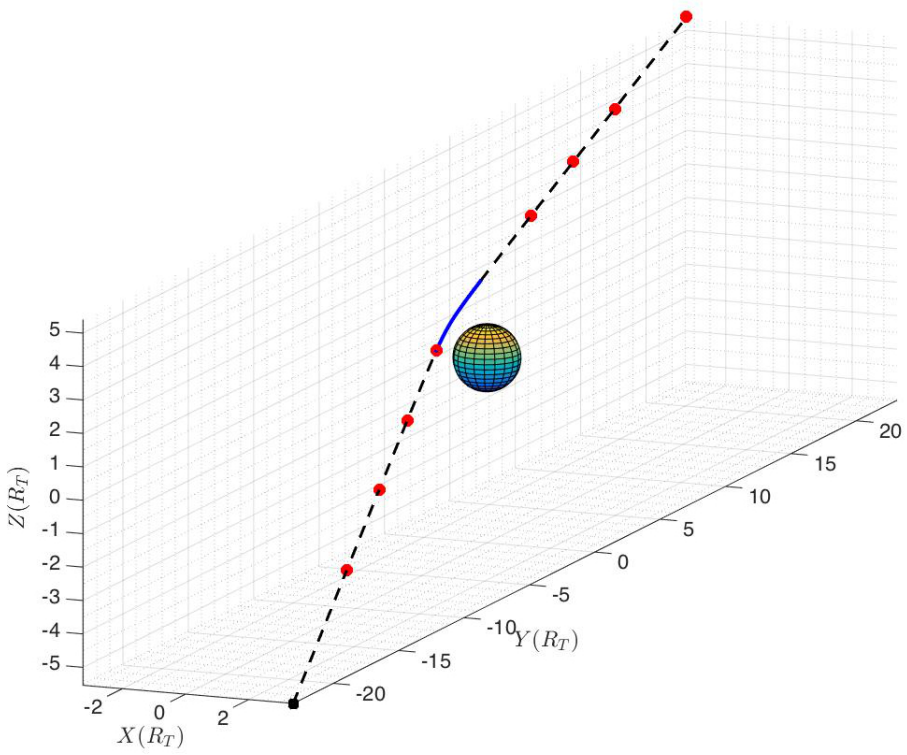

Figure 4.5: Locations where spectra were taken for spectral index analysis (red points). The black point shows the entry point of the trajectory. The sphere at the centre represents Titan, the black dashed line represents Cassini's trajectory during the flyby (TA depicted), the blue solid line being the interaction region excluded for all the analyses presented on this chapter. The plot is shown in TIIS coordinates, with the X-axis pointing into the ideal corotation direction, the Y-axis pointing towards Saturn and the Z-axis completing the right handed triad.

Figure 4.7 shows the average of the spectral indices obtained at the eight chosen locations for each of the flybys for which a classification based on ELS spectra has been made. The colours correspond, once again, to the Rymer et al. (2009) classification. The error bars correspond to the maximum and minimum values after averaging the eight data points.

Even though the average spectral indices lay within values that are in agreement with those presented by Dialynas et al. (2009) for orbital distances close to 20 R_S, the scatter is quite large within the flybys, a further indication of the dynamic nature of Titan's magnetospheric environment. In addition, the differences in the quality of the fits needs to be further analysed in order to better constrain the results.

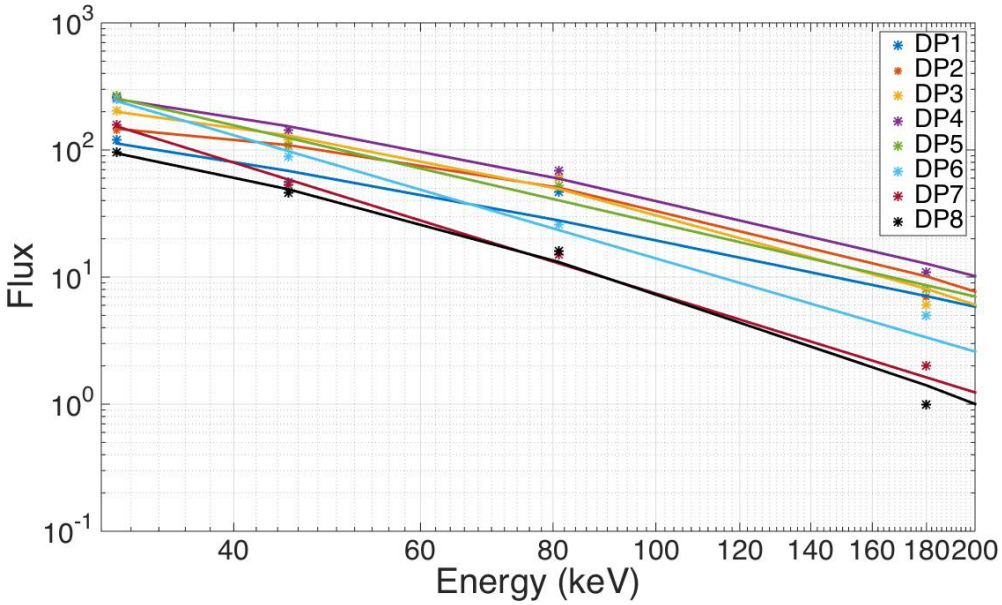

Figure 4.6: Ion fluxes from the ion channels A0-A7 obtained at four locations before (DP1-DP4) and four locations after (DP5-DP8) closest approach during the T5 flyby. The solid lines represent the fits using a modified Kappa disribution.

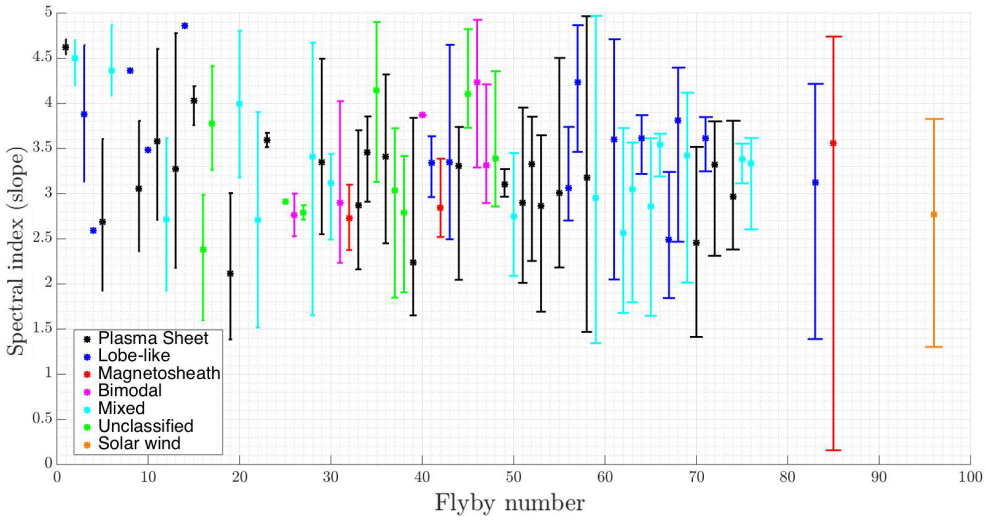

Figure 4.7: Spectral indices obtained from fitting a modified Kappa distribution (Dialynas et al., 2009) to the ion data vs. flyby number.

When comparing between different flybys, the scatter is significant as well, with values ranging from about 2.1 for T19 (a plasma sheet flyby) to about 4.8 for T14 a lobe-like flyby). Even if two flybys falling in the same category are compared to each other, the values between two plasma sheet flybys can range from 2.1 (T19) to 4.6 (TA) and between two lobe-like flybys can range between 2.5 (T67) and 4.8

(T14).

In general, when looking at the indices and the variabilities indicated by the error bars, there seems to be no clear dependence on the magnetospheric environment, indicating that other factors might be playing a more dominant role.

4.3 Saturn local time (SLT) dependence

Garnier et al. (2010) investigated the local time dependence of the proton fluxes as measured by the A0 to A3 LEMMS channels. They found a day-night asymmetry with fluxes about 50% higher on the dayside when compared to the nightside. They interpreted this as a result of the geometry of the plasma sheet, which is thinner on the nightside (Sergis et al., 2009).

Moreover, they found larger fluxes in the magnetospheric region comprising the post-midnight to noon sector. However, the statistics of their analysis were relatively poor with only two events in the dusk sector.

In this section, the analysis performed by Garnier et al. (2010) is extended by taking advantage of the many new flybys and orbit crossings with available data since the publication of that work. The selection of the data is slightly different than the one used in Garnier et al. (2010). While they defined a time window of 1 h around CA, in this study a significantly larger window covering 6 h was used. The reason for chosing a larger time window was to get smoother results by averaging over a longer period while still being within a distance of 1 R_S from the moon. This helps limit the influence of some short-lived events with significantly higher or lower fluxes than the average.

Due to the difference in the dataset selection just explained, a direct comparison between both works is not possible. However, the improved statistics of the analysis presented here contributes to the exclusion of any bias that could be present in the results from Garnier et al. (2010), especially in some sectors where the coverage by Cassini was rather poor by the end of 2007 (e.g. the dusk sector).

Figure 4.8 shows the average ion fluxes detected by MIMI/LEMMS for the ion channels A0 - A2 (A3 to A8 are left out for clarity; their inclusion affects the scaling

of the plot). The average values were calculated among all the available data points, regardless of Cassini's location in terms of magnetospheric environment (plasma sheet, lobes, etc.). In the lower panel, the number of data points at each local time bin is plotted. At some SLT bins, two data points can be observed. This is because for some of the flybys, some of the channels do not have valid data, while the others do. The colour of the markers corresponds to the colour of the two lowest energy channels (A0 and A1 for ions and C0 and C1 for electrons).

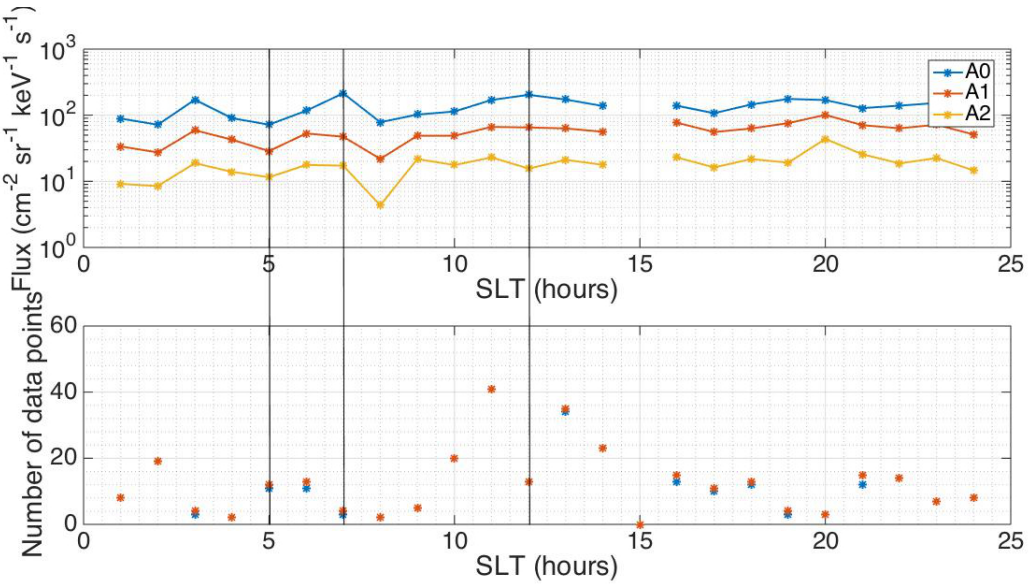

Figure 4.8: Average ion fluxes vs. Saturn local time (SLT) taking into account all the available data (top panel). Number of available data points for a given local time (bottom panel). Only the three lowest energy channels (A0 - A2) are shown for clarity.

The highest mean average for A0, obtained at SLT = 7 (with a similar value for the regions around SLT = 12), is a factor of four larger than the lowest value, obtained at SLT = 5. This variation is smaller than the one reported in Garnier et al. (2010). They also found the fluxes to be higher in the post-midnight sector, a trend that was not encountered in this study with the extended data set. Figure 4.9 shows a circular plot showing average ion fluxes from the lowest energy channel (A0) at different local times.

With the exception of the fluxes at SLT = 3 and SLT = 7, there seems to be a trend of higher fluxes in the noon to dusk side when compared with the midnight to

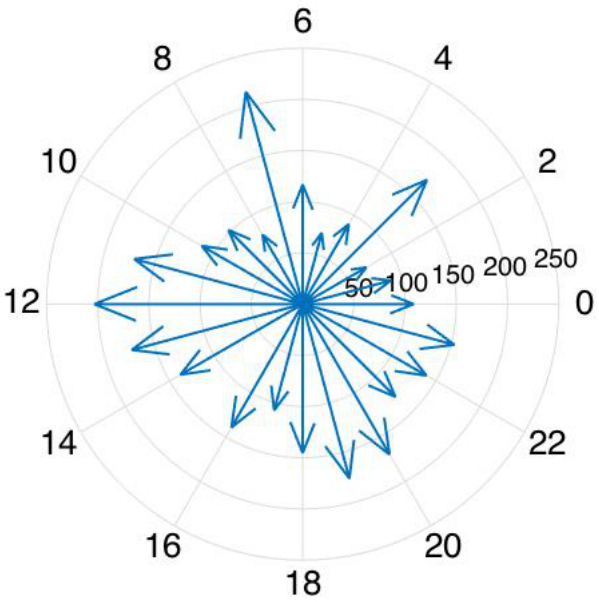

Figure 4.9: Circular plot showing average ion fluxes from the A0 channel at different local times. The length of the arrows represents the fluxes in $cm^{-2}sr^{-1}keV^{-1}sec^{-1}$ with the values indicated at the different concentric circles.

dawn.

An important factor that needs to be taken into account when correlating in-situ data with magnetospheric local time is the difference in coverage. While some SLT bins have only two data points (SLT = 4 and SLT = 8) or no data points at all (SLT = 15), some others, especially close to noon, have up to 46 (SLT = 11).

Figure 4.10 shows the average electron fluxes detected by MIMI/LEMMS for the C0 - C2 channels, once again with the number of data points at each local time bin.

For the case of electrons, the average fluxes at different locations seem to vary much more, with a difference between the minimum (SLT = 8) and maximum (SLT = 9) of almost two orders of magnitude. Once again, the difference in sample size might play an important role in this. For instance, for the the minimum at SLT = 8 and the two surrounding maxima at SLT = 7 and SLT = 9, the number of data points is low, between two and four.

Figure 4.11 shows a circular plot with the average electron fluxes for the lowest energy channel (C0). The variability is so large that the two highest fluxes at SLT =

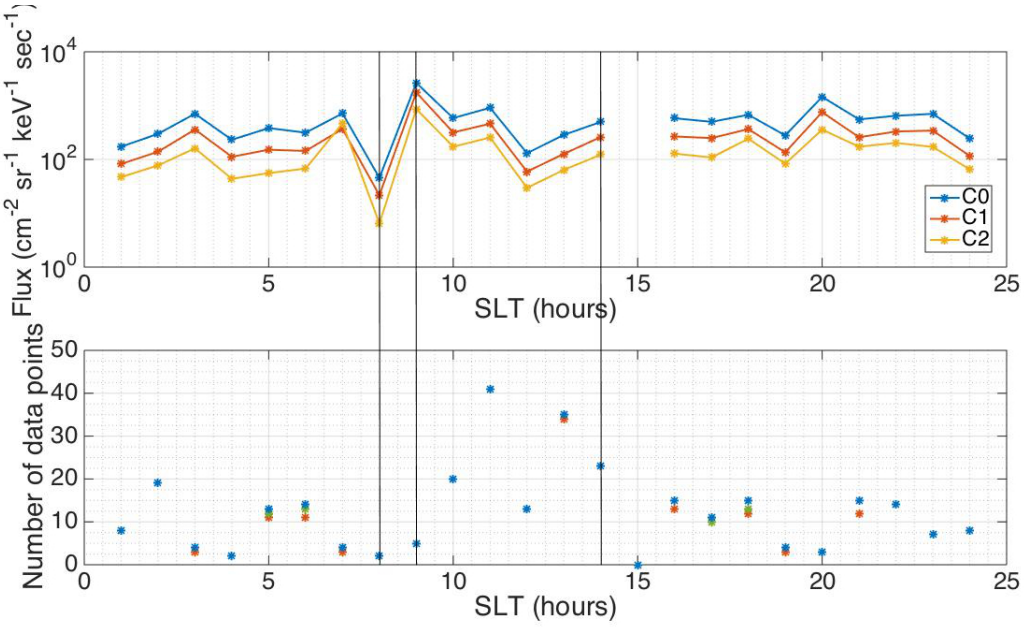

Figure 4.10: Average electron fluxes vs. Saturn local time (SLT) taking into account all the available data (top panel). Number of available data points for a given local time (bottom panel). Only the three lowest energy channels (C0 - C2) are shown for clarity.

and SLT = make it impossible to distinguish many of the other fluxes.

To appreciate the values at all the SLT, instead of using a logarithmic scale that would make it difficult to make a direct comparison with the ion fluxes, the two SLT bins with the highes fluxes were removed and the data is shown in Figure 4.12.

From Figure 4.12 it is impossible to derive any local time dependence. This is caused by the fact that electrons can move away from the equator much more easily than ions can lead to larger variabilities from one flyby to another. This will be tested in the next subsection by looking at the values from different flybys occuring at the same SLT.

To further study the influence of the location in the energetice particle fluxes, the extended data set was used to obtain spectral indices of a fitted modified Kappa distribution as a function of SLT.

Figure 4.13 shows the spectral indices for all the flybys and passes ordered by local time. For this plot, no discrimination between the plasma environment is made, so all the possible environments within the magnetosphere as well as outside are mixed. This is because for many of the data points, no classification in terms of

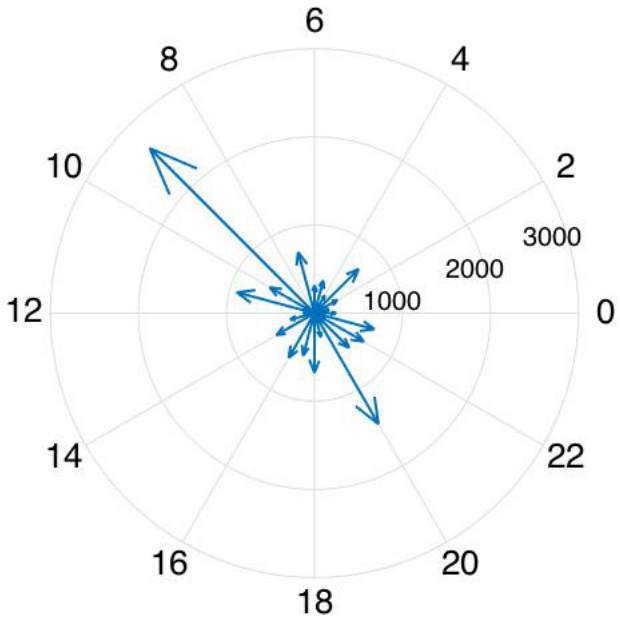

Figure 4.11: Circular plot showing average electron fluxes from the A0 channel at different local times. The length of the arrows represents the fluxes in $cm^{-2}sr^{-1}keV^{-1}sec^{-1}$ with the values indicated at the different concentric circles.

plasma environment is available.

Once again, no trend is obvious from the data, indicating that the spectral shape, while having an L-shell dependency as described in Dialynas et al. (2009), does not have a clear SLT dependency.

4.3.1 Variability between flybys occuring at the same SLT

As shown in Figures 4.8 and 4.10, the amount of data points available at each SLT bin varies significantly. A comparison between different flybys at selected SLT bins can help determine how statistically relevant this difference in coverage might be for the final results.

Ions

Table 4.2 shows the minimum, maximum and average ion fluxes for the A0 channel for all the flybys (T) and passes (P) with valid data that occurred at SLT = 5 and Figure 4.14 shows a graphical representation showing the mean of all the averages, which is the same value shown in Figure 4.8 at the respective SLT position. The data

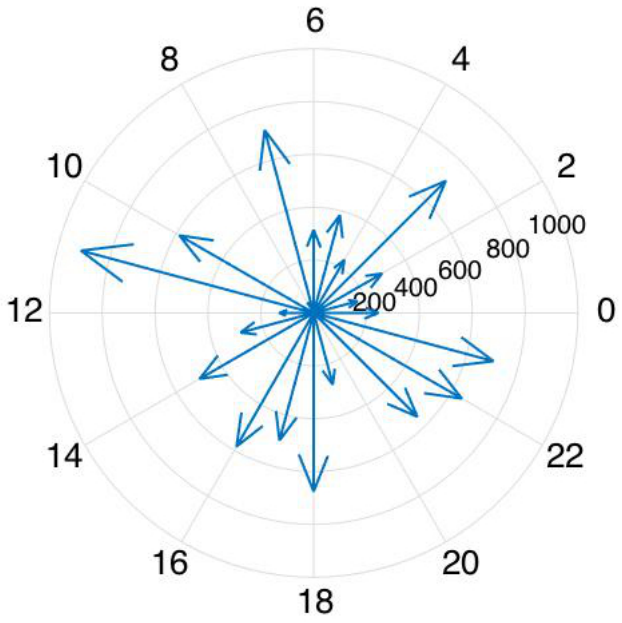

Figure 4.12: Circular plot showing average electron fluxes from the A0 channel at different local times. The length of the arrows represents the fluxes in $cm^{-2}sr^{-1}keV^{-1}sec^{-1}$ with the values indicated at the different concentric circles.

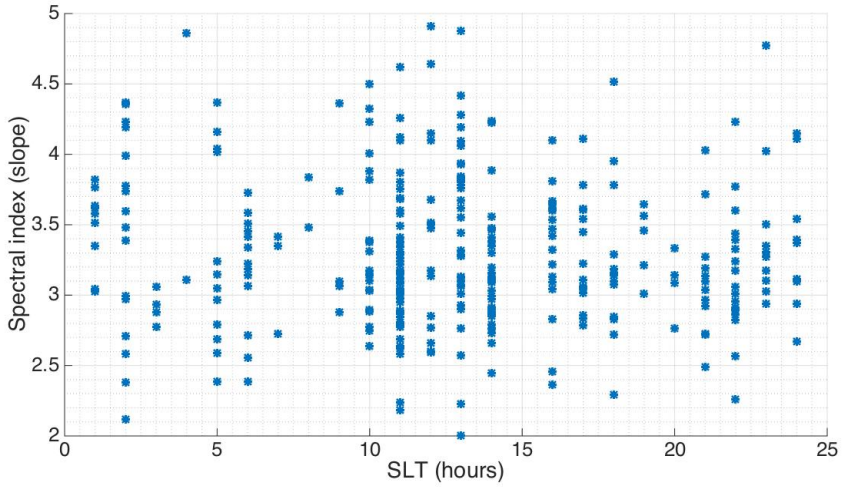

Figure 4.13: Spectral indices obtained for all the available data points vs. Saturn local time (SLT). At each SLT bin, the spectral indices obtained for all the flybys/orbit crossings that happened at that specific local time are plotted.

points for the plots presented in this section are organised by time in order to identify any time dependence on the fluxes such as seasonal effects or the occurrence of flybys or passes during periods of enhanced solar activity.

Flyby	Min. flux	Max. flux	Avg. flux
T4	0.1	83.8	10.0
T5	62.7	408.4	188.5
T6	2.4	130.8	37.7
P2	0.5	214.2	54.9
P4	0.3	200.1	79.1
P6	1.2	191.4	69.9
P7	31.1	456.5	132.5
P8	32.0	211.9	106.6
P11	0.3	151.7	43.8
P13	0.3	208.0	24.1
P15	0.1	280.5	44.5
Avg. values	12	230.7	71.9

Table 4.2: Minimum, maximum and average ion fluxes (channel A0 in $cm^{-2}sr^{-1}s^{-1}keV^{-1}$ for flybys at 5 SLT.

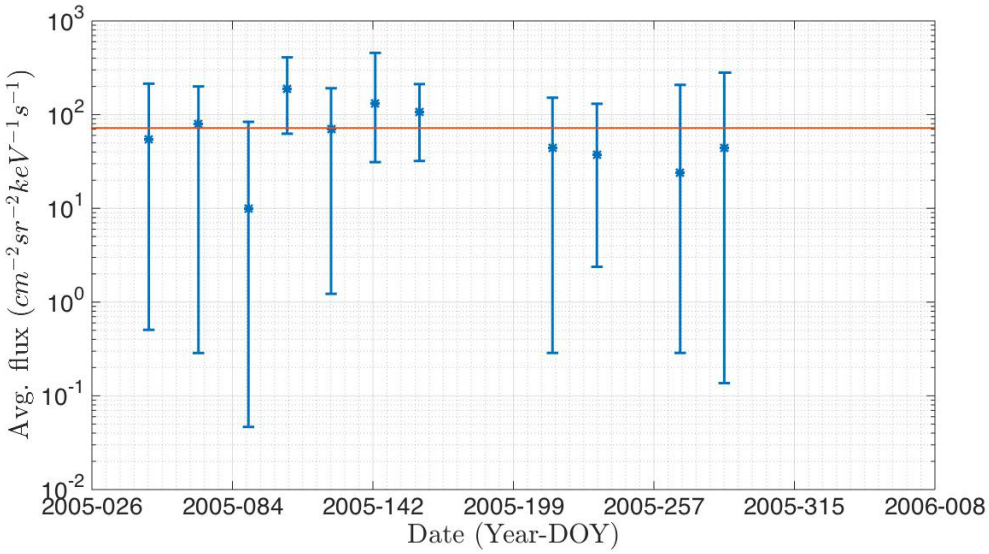

Figure 4.14: Spectral indices obtained for ion data at SLT = 5. The red line shows the average value.

In general, even though some variability is present, the calculated mean seems to be a good representation for all the flybys, lying within the errorbars of each data point. The lower limit of the second data point in Figure 4.14 is almost above the calculated mean but still falls inside. This data point corresponds to the T5 flyby, which was a plasma sheet flyby with relatively high ion fluxes as reported in Cravens et al. (2008).

In terms of local dependence, the coverage is quite uniform with the 11 data

points almost uniformly spread over a period of almost a year. Since all the coverage happened in a relatively short period of time, no seasonal effects can be analysed.

With 11 data points, the SLT = 5 case is one with relatively good statistics. The situation is different for some other regions in the magnetosphere. Table 4.3 shows the minimum, maximum and average A0 ion fluxes for the SLT = 7 bin. The data is plotted in Figure 4.15.

Flyby	Min. flux	Max. flux	Avg. flux
T113	95.9	1321.3	563.8
P171	0.4	171.9	33.4
P175	3.1	175.7	46.4
Avg. values	33.1	556.3	214.5

Table 4.3: Minimum, maximum and average ion fluxes (channel A0 in $cm^{-2}sr^{-1}s^{-1}keV^{-1}$ for flybys at SLT = 7.

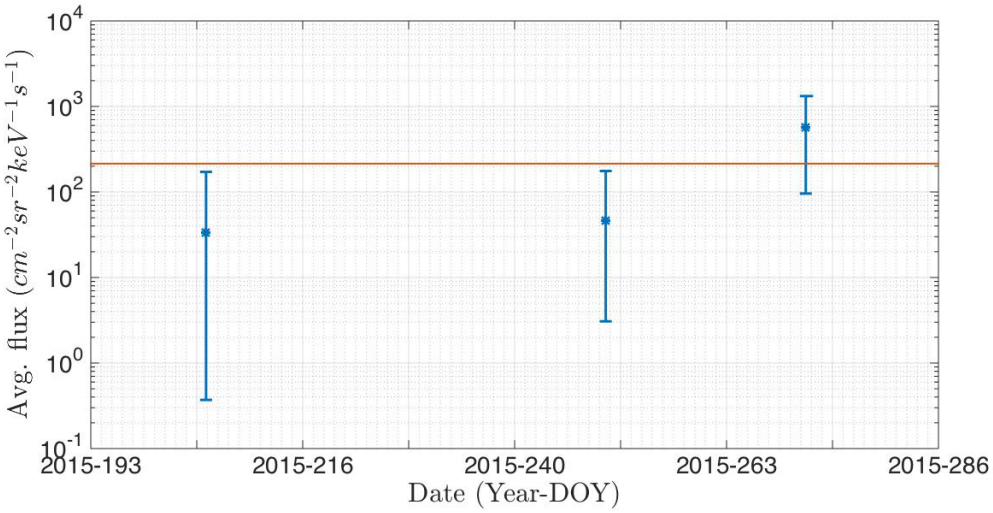

Figure 4.15: Spectral indices obtained for ion data at SLT = 7. The red line shows the average value.

In this case, the statistics are significantly poorer with only three data points. In Figure 4.15 it can be seen that the average value is greatly influenced by the high fluxes from the first data point, T113. This has the effect that the calculated mean value does not properly represent all the measurements but, since the number of data points is so low, considering one as an outlier is not an appropriate approach. Once again, seasonal effects cannot be analysed since the time difference between the first and last data point is of less than one year.

A different situation arises when looking at local times close to noon. At SLT = 12, the spatial coverage by Cassini is significantly better with 13 data points for which the ion fluxes from the A0 channel are presented in Table 4.4. Once again, the data are represented in Figure 4.16 as well.

Flyby	Min. flux	Max. flux	Avg. flux
T35	1.7	286.1	70.3
T77	11.13	435.0	170.4
T96	11.0	10811.0	1536.0
T97	29.7	297.8	110.4
T98	0.1	337.2	63.3
T99	8.5	168.5	84
T100	0.1	55.6	20.1
P33	1.1	389.2	53.8
P111	0.3	808.1	90.1
P114	31.1	632.5	85.0
P116	35.9	957.5	238.9
P118	0.1	342.7	38.0
P162	21.4	154.3	82.0
Avg. values	11.7 (11.8)	1205.8 (405.4)	203.2 (92.2)

Table 4.4: Minimum, maximum and average ion fluxes (channel A0 in $cm^{-2}sr^{-1}s^{-1}keV^{-1}$ for flybys at SLT = 12.

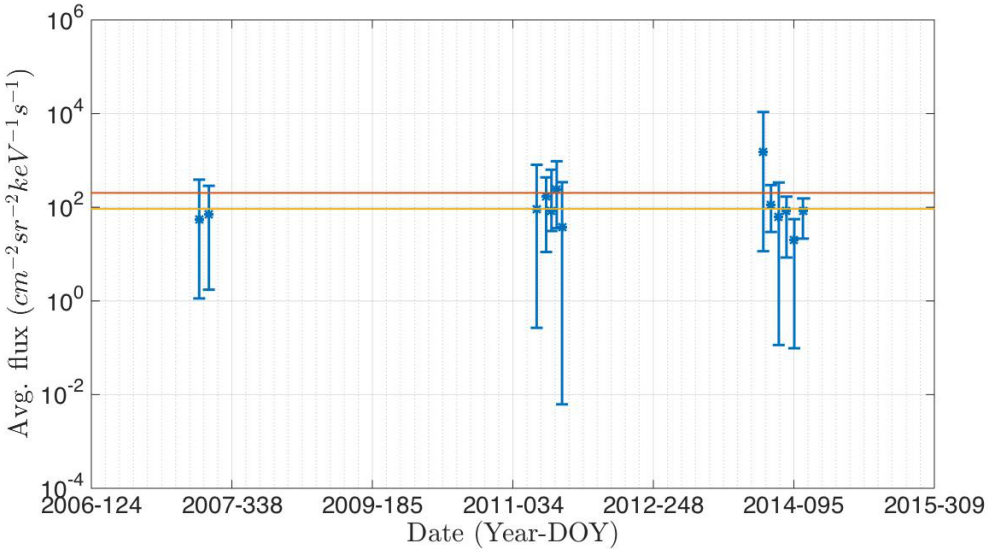

Figure 4.16: Spectral indices obtained for ion data at SLT = 12. The red line shows the average value with all the data points and the yellow line shows the average value after removing the third data point (corresponding to T96).

A significant outlier can be detected in the data which corresponds to T96, the

only solar wind flyby. This can be observed in the large peak at the third data point in Figure 4.16. If the mean of all the average fluxes is taken (red horizontal line), three data points are outside the calculated value. If the mean value is then calculated without taking into account the data from T96, the situation improves with only one data point lying outside of the calculated value. This point corresponds to the T100 flyby.

In general, removing the fluxes of the T96 flyby seems to give a good representation of the energetic ion fluxes within the magnetosphere for the SLT = 12 bin.

For this case, the temporal coverage is quite good in the sense that almost seven years passed between the first and the last data point, but the distribution is quite sparse, with three clear groups happening at the end of 2007, beginning of 2011 and beginning of 2015.

The first group of two data points occurred two years before equinox while the second group occurred two years after equinox. Even though the fluxes of the second group seem to be higher, the number of data points available is not large enough to draw conclusions regarding a seasonal effect. Additionally, being both goups almost equally separated from equinox and given the axisymmetric field configuration of Saturn, no significant diffence should be expected.

Electrons

For the case of electrons, once again the variability present in the data makes it more complicated to get an average value that serves as good representation of the fluxes encountered at any given SLT with a simple approach, even for bins with a large number of data points.

Table 4.5 and Figure 4.17 show the case of an SLT bin with very poor statistics and corresponds to the global minimum depicted in Figure 4.10.

With only two data points, it is impossible to define a strategy that gives a good representation of the local fluxes. From Figure 4.17 it can be seen that the mean fluxes are significantly different between both data points (an order of magnitude) without any overlap of the error bars.

Flyby	Min. flux	Max. flux	Avg. flux
T10	43.2	144.4	83.9
P21	0.1	28.5	7.0
Avg. values	21.7	86.5	45.5

Table 4.5: Minimum, maximum and average electron fluxes (channel C0 in $cm^{-2}sr^{-1}s^{-1}keV^{-1}$ for flybys at SLT = 8.

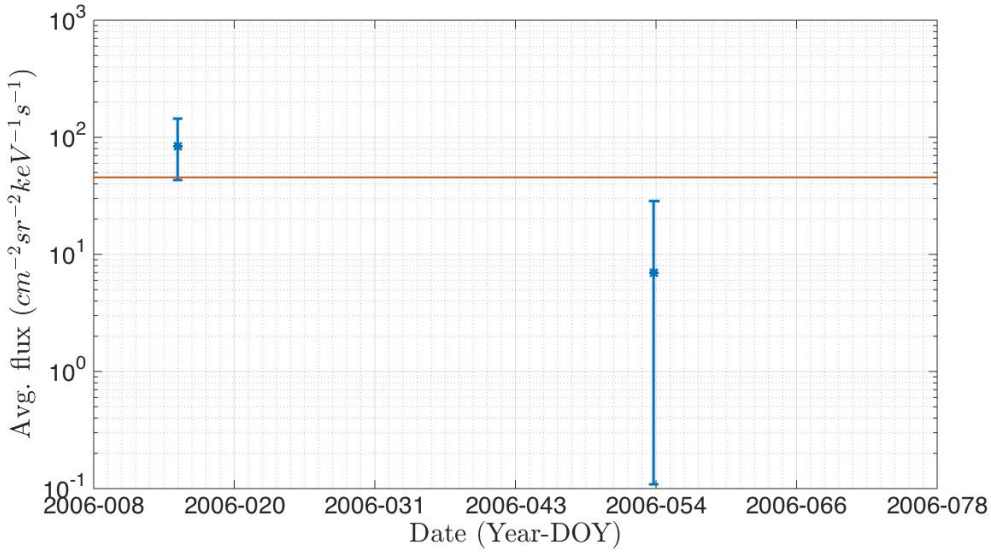

Figure 4.17: Spectral indices obtained for electron data at SLT = 8. The red line shows the average value.

Table 4.6 and Figure 4.18 show the case for the global maximum right next to the minimum from SLT = 8.

Flyby	Min. flux	Max. flux	Avg. flux
T8	4.9	362.8	39.7
P12	1071.0	22041.0	11897.0
P14	0.2	147.5	17.0
P17	2.7	220.8	50.4
P19	67.9	5097.2	1222.0
Avg. values	229.34 (2.6)	5573.9 (243.7)	2645.2 (35.7)

Table 4.6: Minimum, maximum and average electron fluxes (channel C0 in $cm^{-2}sr^{-1}s^{-1}keV^{-1}$ for flybys at SLT = 9.

For this case, even though statistics are slightly better, with five data points still two show fluxes that are significantly higher than those of the remaining three points. Additionally, being located relatively far from the sub-solar point, it is hard to explain the high fluxes from the first data point (corresponding to the orbit cross-

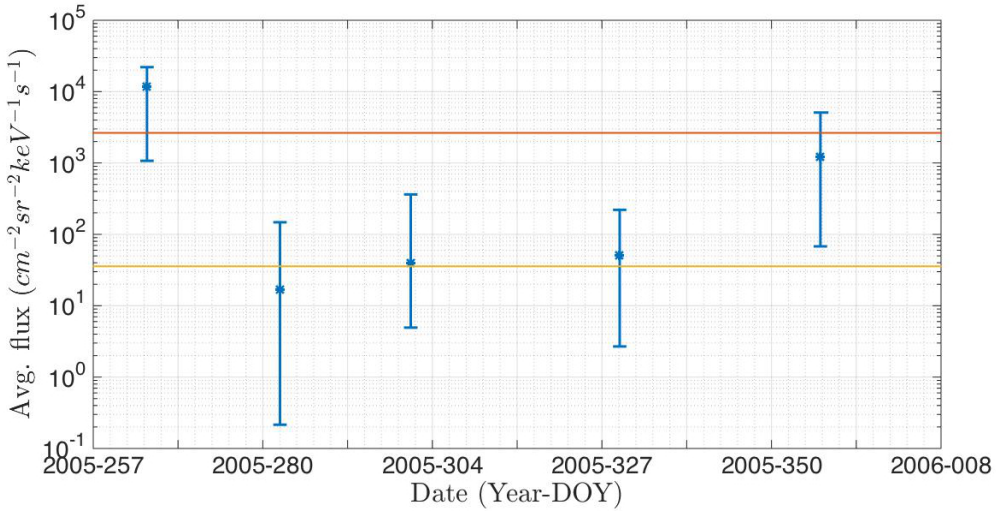

Figure 4.18: Spectral indices obtained for electron data at SLT = 9. The red line shows the average value with all data points and the yellow line shows the average value after removing the first and last data points (corresponding to orbit crossing P12 and P19 respectively).

ing P12) in terms of location of Cassini inside or outside the magnetosphere. An analysis of the magnetic field data similar to the one performed by Simon et al. (2013) could help in establishing the location with respect to the plasma sheet but, on the one hand, that analysis is beyond the scope of this thesis and, on the other hand, the analysis presented earlier in the chapter showed no correlation between the plasma regions and the energetic electron fluxes.

Even by removing the two data points with the largest fluxes and re-calculating the mean fluxes, the result gives only a marginally better representation, this time covering three of the five data points available.

A case with significantly better statistics is presented in Table 4.7 and Figure 4.19. These present the C0 fluxes for the SLT = 14 bin, which has 23 data points in total.

Still, the variations are significant and even by removing the data point with the largest fluxes (P133), a simple mean value fails to represent five of the 23 data points.

In general, all the analyses presented in this chapter indicate that the energetic magnetospheric environment at Titan's orbit is highly variable. There is also a sig-

Flyby	Min. flux	Max. flux	Avg. flux
T25	4.9	282.1	127.8
T26	30.9	185.3	85.5
T27	90.8	304.3	207.6
T28	22.8	475.4	102.2
T29	3.5	283.4	72.1
T30	48.3	3207.1	1008.1
T31	12.5	1534.4	219.9
T32	0.1	1124.1	166.5
T33	8.9	4090.7	387.7
T75	195.0	1068.4	482.1
T83	75.9	500.2	201.6
T84	25.7	411.4	80.4
T85	0.1	59.2	2.9
P30	92.7	2201.5	780.1
P107	1.0	192.7	43.5
P109	16.4	71.9	32.3
P131	1.5	10.1	4.4
P133	191.3	15627	5480.2
P135	5.1	415.3	53.4
P137	86.4	552.7	291.3
P139	10.3	2150.8	672.0
P141	0.3	1678.9	135.2
P142	63.4	2505.3	824.7
Avg. values	42.9 (36.2)	1692.7 (1059.3)	498.3 (271.9)

Table 4.7: Minimum, maximum and average electron fluxes (channel C0 in $cm^{-2}sr^{-1}s^{-1}keV^{-1}$ for flybys at SLT = 14.

nificant difference between the overall behaviour of ions and electrons which is attributed to the higher inertia of ions due to their larger mass which causes them to remain closer to the equator due to centrifugal forces. This makes it easier to classify the environment based on the fluxes, even though the correlation is far from that observed with the thermal plasma data.

In terms of local time dependence, the noon-midnight asymmetry reported in Garnier et al. (2010) is observed. However, while a dawn-dusk asymmetry was also detected, it is contrary to the one reported by Garnier et al. (2010). While they found larger fluxes in the post-midnight sector, in the analysis presented here higher fluxes were detected in the dusk sector when compared to dawn. When looking at all local times, for the lower energy ions the fluxes are in general higher on the noon-to-dusk

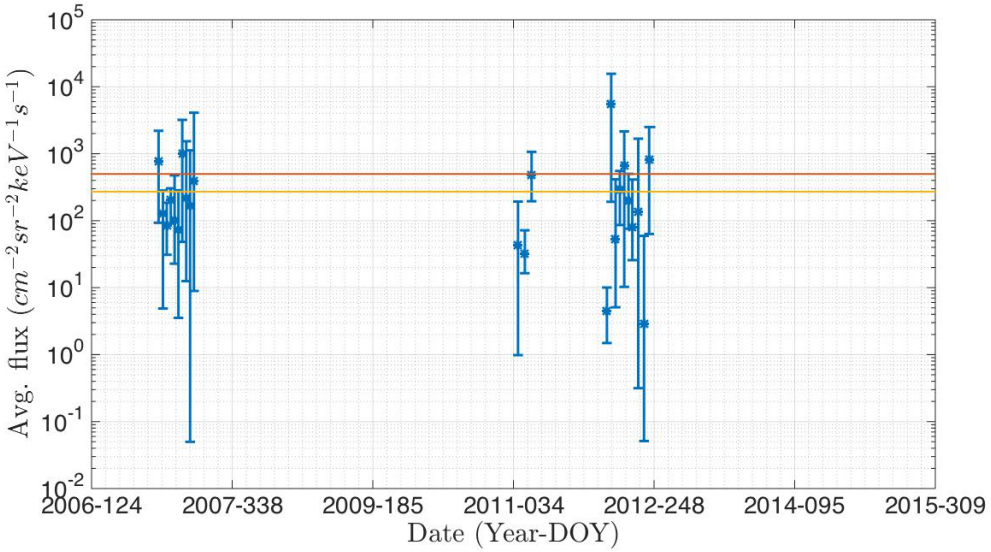

Figure 4.19: Spectral indices obtained for electron data at SLT = 14. The red line shows the average value with all data points and the yellow line shows the average value after removing the 18th data point (corresponding to orbit crossing P133).

sector with lower fluxes in the midnight-to-dawn sector, with the exception of SLT = 3 and SLT = 7, even though both local time bins only contain three data points.

In general, the explanation for these asymmetries can be manifold and it is beyond the scope of this analysis. Some of the aspects that could play a role include transport processes (e.g. Dungey or Vasyliūnas cycles with depleted field lines after crossing reconnection regions) or large-scale electric fields that induce asymmetries in the magnetospheric flows such as the noon-to-midnight described by Andriopoulou et al. (2012).

For the electrons, no SLT dependence is observed in any of the channels, indicating that the high variabilities encountered might have their origin in non-local processes like for instance injection events or changes in the overall structure of the magnetosphere due to solar wind activity.

A combination of the data analysis presented here with test particle simulations like the ones presented in Chapter 5 could help establish typical energy deposition rates at Titan for the different possible scenarios.

Due to the presence of very high energetic ion fluxes encountered when Titan is located in the solar wind, it is expected that the ionisation of the atmosphere

due to precipitating ions can be more significant than when Titan is inside the magnetosphere. This might also have an effect on the atmospheric losses, so a more detailed multi-instrument analysis of the plasma data combined with simulations needs to be performed to further extend the knowledge of how Titan interacts with the surrounding magnetospheric environment.

Chapter 5

Energy deposition and ionisation rates by energetic ions at Titan

The contents of this chapter were published in Regoli et al. (2015).

Titan is immersed in a very complex and dynamic plasma environment that, together with its dense atmosphere and chemically rich ionosphere, creates a unique interaction region that needs to be analysed on a case-by-case basis.

The interaction region at a given time will not only affect the convection of charged particles in the vicinity of the moon, but also on the location and incidence angle at which those particles will interact with the moon's atmosphere. This will in turn affect the energy deposition and ionisation rates and thus the local densities of the ionosphere.

In this chapter, the effect that the incidence of energetic particles have on the ionosphere is studied in detail by investigating a specific flyby using a local magnetospheric model based on a hybrid code simulation.

First, basic concepts of energy deposition and ionisation rates in planetary atmospheres are introduced, followed by an explanation of the techniques used to estimate ionisation rates at Titan for the specific case of the ninth dedicated flyby by Cassini (T9).

5.1 Energy deposition by energetic ions

The partially corotating plasma of Saturn's magnetosphere interacts with Titan's atmosphere depositing energy at altitudes that depend on various factors such as species, energy and incidence angle. Through this interaction, this incoming plasma will contribute to the ionisation of the atmosphere and, therefore, to the local ionospheric densities.

Where a given ion will deposit its energy or, in other words, how deep in the atmosphere a given ion will penetrate, depends on the collision cross section of the atmospheric constituents, which is in turn dependent on the precipitating ion species and energy. In the outer magnetosphere of Saturn, the plasma is mostly composed of H^+, H_2^+ and W^+ (Thomsen et al. 2010). Even though energies can be as low as 1 eV, for this study only energetic ions are considered, with energies from 1 keV to 1 MeV.

In a more global scale, another factor that determines where ions deposit their energy is the configuration of the electromagnetic fields at any given time because this configuration affects the way particles are conveyed around the moon to ultimately reach the exobase at a specific position.

To calculate the energy deposition, the stopping power of a given ion in the gas that composes the atmosphere in units of energy per mass density (e.g. $MeV \cdot cm^2/mg$) is needed. This stopping power can be obtained by direct measurements in the lab, by Monte Carlo simulations or by a combination of both. Additionally, a density profile of the atmosphere being studied is needed as well.

With this, ions of a specific energy are propagated by using numerical integration from the exobase downwards. With each altitude step, the ion being propagated loses a fraction of its energy given by Equation 5.1 where dE is the energy lost, $S(E)$ is the energy-dependent stopping power and $n(h)$ is the altitude-dependent neutral density of the atmosphere. This process continues until a threshold in energy or altitude is reached. These thresholds depend on what is being studied like for instance the energy deposition at a given altitude or the contribution of ions of cetrain energy to the ionisation rates. Additionally, the availability of stopping powers will

set a strong limitation as well, since these are not available for every species at any energy.

$$dE = S(E) \cdot n(h) \tag{5.1}$$

To calculate integrated ionisation rates (in $cm^{-3} \cdot s^{-1}$) from ions with energies higher than E_i and lower than E_f, Equation 5.2 is used. The upper and lower energy levels are defined according to the application in scope. In the case studied here, the upper level is the maximum energy of a distribution (i.e. 1 MeV) and the lower level is the minimum energy for which stopping powers are available (5.17).

$$IonRate = \int_{E_i}^{E_f} \frac{\phi_{ions}}{E_{ion}} dE \tag{5.2}$$

The energy deposition for each energy (dE, in eV/cm) is divided by the ionisation energy (E_{ion}, the energy required to strip an electron from a given atom or molecule, given in eV) of the molecular component of the atmosphere and multiplied by the initial fluxes (ϕ_{ions}, in $cm^{-2} \cdot s^{-1}$). This gives the total ionisation

5.2 Particle tracing software

To study the way in which Titan interacts with the surrounding magnetospheric plasma, a particle tracing software package was developed based on a code from Kotova et al. (2015) used to study the interaction of Rhea with the Saturnian magnetosphere. The basic aim of the code is to be able to perform both forwards and backwards tracing of charged particles in the vicinity of the moon, taking into account the specific conditions encountered by Cassini for specific flybys.

The basic working principle of the tracing code is the integration in three dimensions of the Lorentz force (Equation 2.5) to study how charged particles propagate in a background electromagnetic field configuration. The integration is made using a fourth order Runge-Kutta numerical method.

Different background field models are implemented, namely a dipole field with an offset of 0.036 R_S shifted northwards along the planet's spin axis (Burton et al. 2010), the global magnetospheric model known as Khurana model (Khurana et al.

2006), the output of a hybrid code (kinetic ions, fluid electrons) developed at the University of Braunschweig named A.I.K.E.F. (Müller et al. 2011, Feyerabend et al. 2015) or any combination of these (e.g. hybrid code in the vicinity of the moon and Khurana's model outside the interaction region).

The propagation can be carried out forwards or backwards in time by changing the sign of the time step for the numerical integration. The idea of a forward tracing simulation is to place many particles with different initial positions in phase space throughout the 3D simulation grid with a given distribution of pitch angles and energies and propagate them forwards to study how the simulated population evolves in time.

Backward tracing in turn is used to study how a given population reached a specific position in space. The principle is the same as for forward tracing: a population of particles with specific initial conditions is propagated in space, only that it is done with a negative time step. This approach can save a significant amount of computational time, because a large amount of the forward-traced particles will not reach the final position of interest and thus will have no effect on the final result. Furthermore, given that the simulations presented in this chapter are run in a non-collisional environment (above the exobase), there are no statistical errors introduced, something that could affect the results obtained at the end of the tracing process (Marchand 2010).

The tracing software can also work with the guiding centre approximation (GCA; see Chapter 2 in this thesis), which is useful when dealing with particles with small gyroradius (mostly electrons) that closely follow the magnetic field lines.

Figure 5.1 shows the capabilities of a tracing software. The image depicts the trajectory of four different test particles (protons) with different initial energies, all of them starting at the same position close to the moon. During the simulation, all the particles were launched from the same position and with the same initial pitch (polar) and phase (azimuthal) angle. However, the difference in gyroradius causes one of them to hit the moon before completing a gyration (10 keV, blue curve) while the others drift away from the moon but all of them following a completely

different trajectory, with the ones with lower energy more closely following the magnetic field lines (1 keV, red curve).

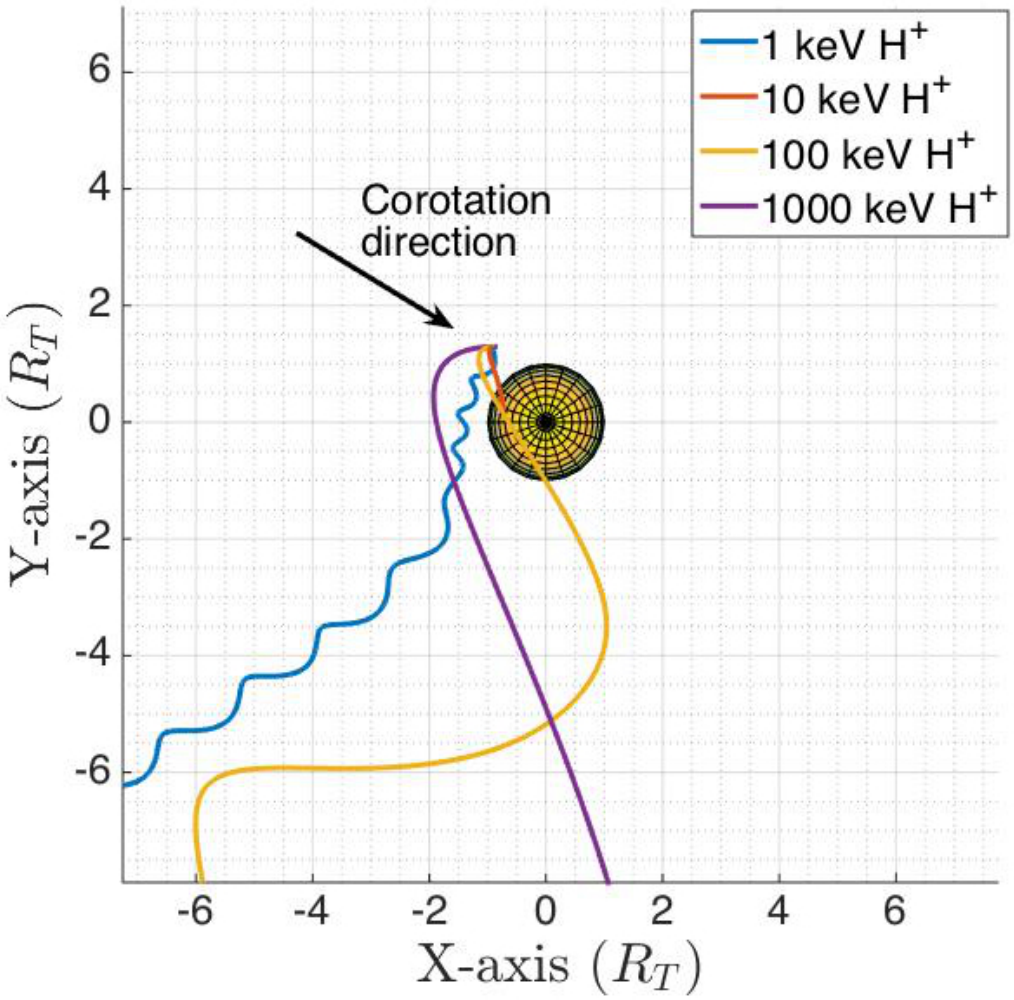

Figure 5.1: Illustration of the principle of a particle tracing software code. The circle at the centre represents Titan (as seen from the north pole). Each of the four solid lines represent the trajectory of charged particles with different energies, all of them with the same starting position. The black arrow shows the corotation direction during the simulated environment which corresponds to Cassini's T9 flyby.

For most of the simulations presented in this chapter, the electromagnetic field configuration was taken from an output of the hybrid code specifically produced for the T9 flyby (see sub-section 3.3). The output is available for a limited region around Titan, specifically inside a simulation box of 15 Titan radii on each side. The tracing code then takes the output of the hybrid code for a specific flyby and

traces particles with a set of characteristics that are given as an input. These are initial position, type of particle (electron or ion), mass (for ions), energy and initial pitch and phase angles.

As described before, the magnetospheric environment in the vicinity of Titan is heavily influenced by the presence of the moon itself. This creates a complicated electromagnetic configuration that is highly variable, both in time and space. For this reason, the way charged particles behave close to Titan changes from one flyby to the next, making it necessary to study each flyby separately.

By understanding the way charged particles move close to the moon, it is possible, with the help of the tracing software, to predict where different particles will deposit their energy in Titan's atmosphere and how they contribute to local ionisation rates.

Appendix A presents a validation test run of the tracing software and an analysis of the results.

5.3 Case study: T9 flyby

The T9 flyby took place on the 26th of December 2005 at approximately 19 hours UT. It was a mid-distance tail flyby, with an altitude at closest approach of 10411 km. According to the plasma environment classification by Rymer et al. (2009), Titan was located in the plasma sheet, specifically below the current sheet as indicated by the magnetic field and thermal plasma data collected by Cassini (Sittler et al. 2010).

Figure 5.2 shows the equatorial magnetic field in TIIS coordinates as obtained from the A.I.K.E.F. hybrid simulation and Figure 5.3 shows the comparison between the measured magnetic field magnitude and the three components, again in TIIS coordinates, and the output of the hybrid code along Cassini's trajectory

The equatorial trajectory of the flyby (shown in Figure 5.4) was ideal for the study of the mid-range tail of Titan (Bertucci et al. 2007) and led to the observation of a number of interesting phenomena, such as a split tail and also the presence of photoelectrons, both reported by Coates et al. (2007b).

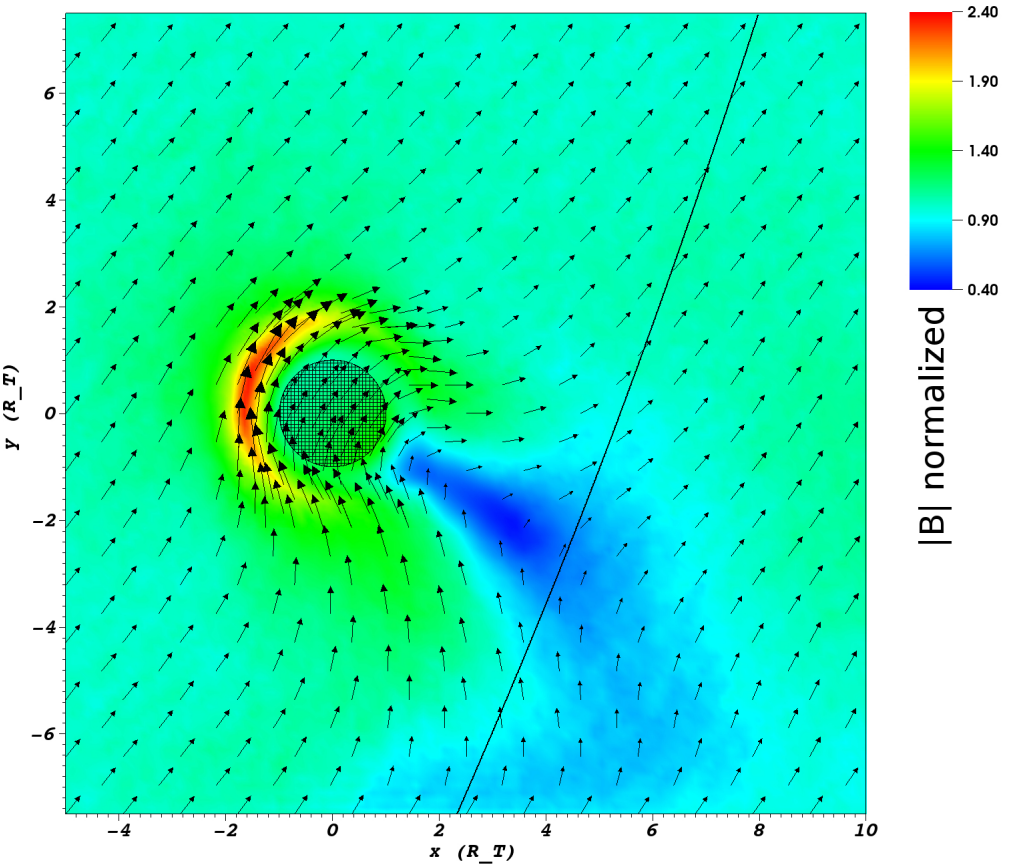

Figure 5.2: Output of the A.I.K.E.F. code for the equatorial magnetic field configuration during the Cassini T9 flyby in the Titan Interaction System (TIIS) coordinate system (Neubauer et al. 2006) with the X-axis pointing in the ideal corotation direction, the Y-axis towards Saturn and the Z-axis completing the right-handed system along the spin axis of the moon. The colour code represents the magnitude of the magnetic field normalised to the upstream field magnitude (6.37 nT). The arrows show the direction of the magnetic field. The black solid line represents Cassini's trajectory during the flyby.

The specific magnetic field configuration observed during the T9 flyby was far from the ideal north-south configuration. This enables the analysis of ion trajectories in a complex electromagnetic environment to study how these trajectories affect the location where particles reach the moon and further deposit their energy.

5.4 The simulations

To analyse the access of energetic particles to the exobase, ions with $m/q = 1$ (H^+) and $m/q = 16$ (O^+) with energies ranging from 1 keV to 1 MeV were backtraced starting at the exobase of the moon (set for this study at 1450 km; test runs to study

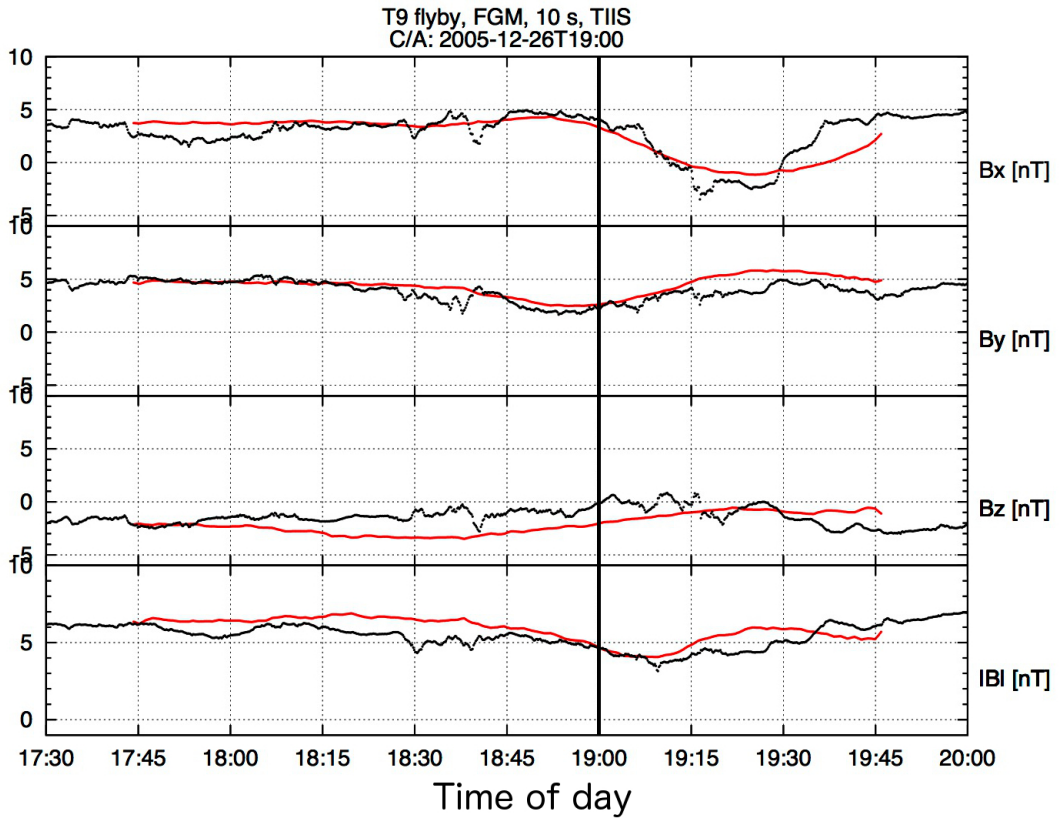

Figure 5.3: Magnetic field measured by Cassini during the T9 flyby (black lines) and output of the A.I.K.E.F. hybrid code for the same flyby (red lines; M. Feyerabend, private communication).

the validity of this choice are presented in appendix B). The use of backtracing instead of forward tracing prevents the simulation of a large number of particles that would never reach the exobase and therefore would not add any valuable information to the study.

The basic idea behind the backtracing is to start the particles at the exobase and, after being backtraced, two possible situations arise:

- If the particle being simulated impacts the moon before leaving the simulation domain, it means that the path that a magnetospheric particle would have to follow in order to reach the exobase at the location where the simulation was started with the given energy, pitch and phase angles is forbidden. In this scenario, the particle is not taken into account in the subsequent analysis.

- If the particle is able to escape the simulation domain given by the boundary

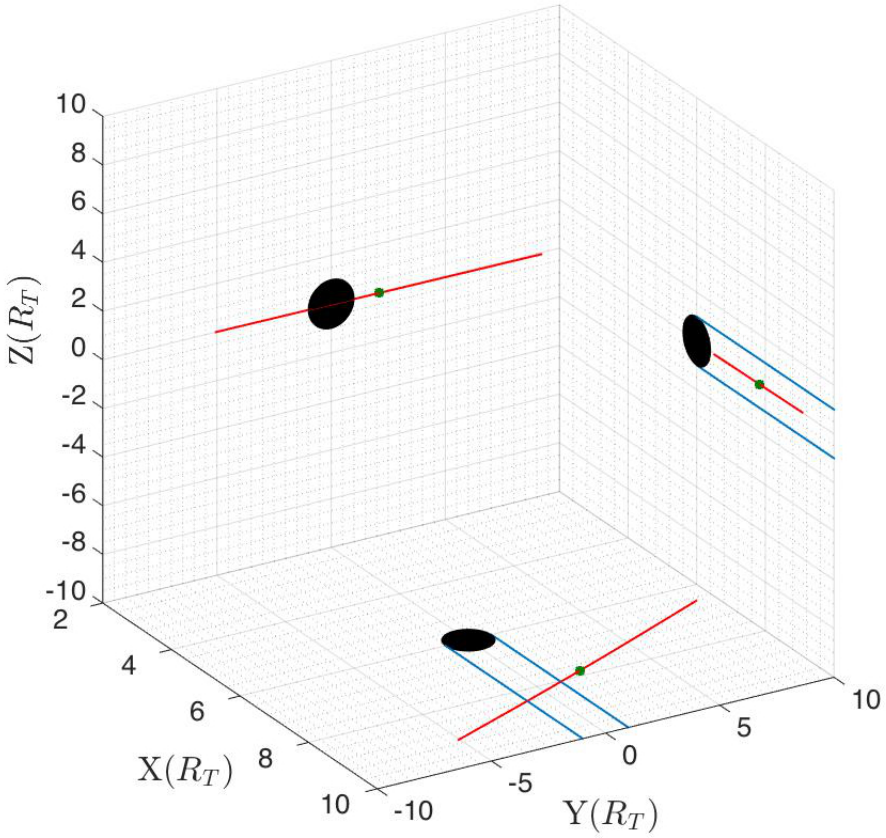

Figure 5.4: Cassini trajectory (red line) during the T9 flyby represented in TIIS coordinates. The blue parallel lines show the location of the ideal corotating tail.

conditions (the choice of the boundary conditions is explained below), the path that a magnetospheric particle would need to follow to reach that location with the given energy, pitch and phase angle is assummed to be valid. In this scenario, the particle is taken into account in the subsequent analysis.

By using the backtracing method, an underlying assumption of isotropy in the upstream flow is made. While the assumption is not explicit as it would be in the case of forward tracing, the only factor being taken into account for a particle to be considered is the fact that it can reach a given location far from the moon, no matter its velocity. By looking at pitch angle distribution of energetic ions at Titan's orbit, Garnier et al. (2010) concluded that the distributions are indeed quasi-isotropic.

At each position, particles with all the pitch angles (from 0° to 180°) and phase angles (from 0° to 359°) were launched. The properties of the particles that were

changed during the simulations are:

- Starting position: as mentioned before, the starting positions were all at an altitude of 1450 km (exobase of Titan) and were chosen to cover all the latitudinal and longitudinal positions around the moon. The step was set at 1° both for latitude and longitude change, giving a uniform grid for a 2D representation of the data (see results below).

- Pitch (polar) angle: for each starting position and each energy, the pitch angle was changed from 0° to 180° with a linear step of 2°.

- Phase (azimuthal) angle: especially important when dealing with large gyroradii (higher energies), the phase angle was changed from 0° to 359° with a linear step of 5°.

Since the step in polar and azimuthal angles is invariant, this gives a better coverage near the poles. This, however, does not affect the validity of the results, since no abrupt changes in the access of particles can be observed, as shown in the results section of this chapter.

The conditions just described give a total number of approximately 70 million particles for each energy and each species being simulated. For each simulation run, two different boundary conditions needed to be defined. These boundary conditions will define when to stop the simulations.

The first one is necessary for when particles reach the close proximity of the moon. Since only individual particles are considered, once they reach this boundary they can be removed from the simulation without introducing discontinuities in the overall particle density. Once a particle reaches the exobase (1450 km), instead of stopping the simulation right away, the particle is allowed to penetrate slightly further to avoid removing particles that could escape and that are only penetrating deeper than 1450 km due to gyroradius effects. This inner boundary is then set at 1400 km, a region that is still considered collision-free by many authors who actually set the exobase at that altitude (Ledvina et al. 2012, Wulms et al. 2010, Sittler et al. 2009).

The second boundary condition is necessary to decide when to stop tracing particles that drift away from the moon. This condition needs to be defined carefully since particles can reach large distances from the moon and still come back because of gyroradius effects or due to the bouncing motion at magnetospheric mirror points.

First, simulated particles need to reach a location in space with undisturbed magnetic field, i.e. outside the interaction region. This, however, is not sufficient since the simulated particle may have a gyroradius large enough, so that even after reaching this location it might come back and still reach the exobase, as shown in Figure 5.5.

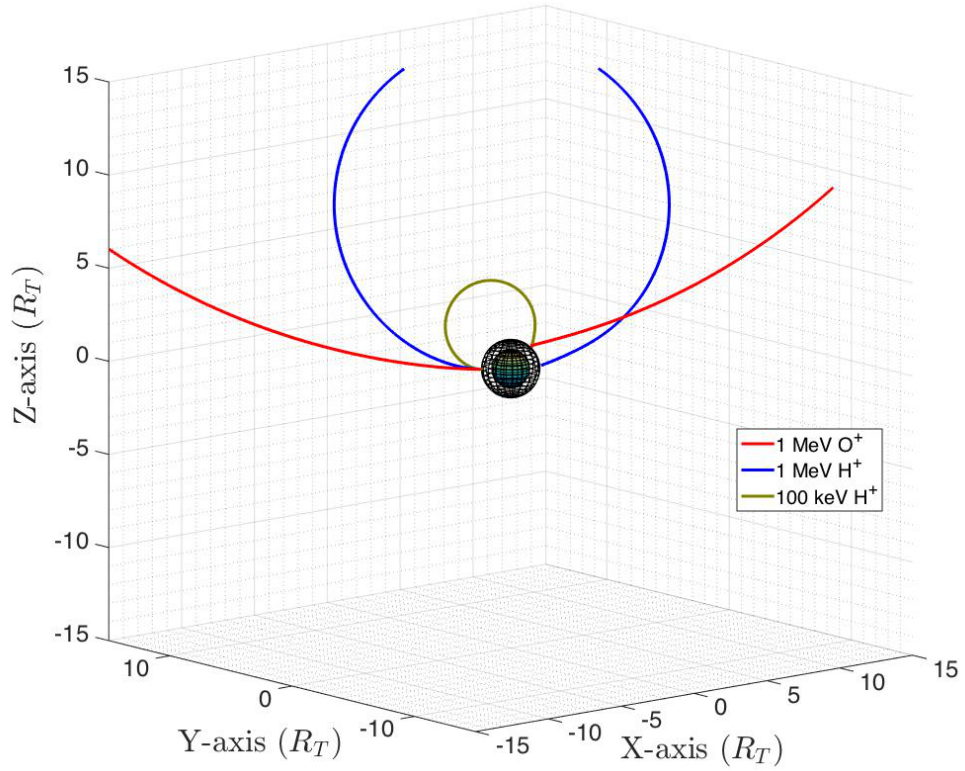

Figure 5.5: Trajectories of three different ions starting at the same position and hitting the exobase after one gyration at different locations. Titan is located in the centre surrounded by the exobase (transparent grid). The plot is shown in TIIS coordinates.

A further consideration arises from the fact that, after leaving the interaction region, particles can travel along the field lines all the way to the mirror points, come back and still hit the moon's atmosphere. To rule out this possibility, the half-

bounce equatorial displacement for the simulated particles was calculated using the method described in Roederer (1967) and the magnetospheric model of Khurana et al. (2006).

The method consists of calculating the equatorial displacements due to the magnetic and electric fields separately and then combining them to obtain the full displacement. To calculate the magnetic field-related drift, Equation 5.3 is used, where m_o is the the particle's mass, q is the elementary charge, c is the speed of light in vacuum, B_{eq} is the equatorial magnetic field at the L-shell where the calculation is made, γ is the relativistic Lorentz factor and I and S_b are line integrals that are related to the length of the magnetic field lines through which the particle would have to travel and are calculated using Equations 5.4 and 5.5. The limits of integration in Equations 5.4 and 5.5 (λ_m) are the latitudes of the mirror points, B_m is the magnetic field magnitude at those mirror points and $B(s)$ is the magnetic field magnitude at the position where the integral is being calculated.

$$v_m = \frac{m_0 \cdot c^2}{q \cdot B_{eq}} \cdot \frac{\gamma^2 - 1}{\gamma} \cdot \frac{\nabla I}{S_b} \tag{5.3}$$

$$I = \int_{-\lambda_m}^{\lambda_m} (1 - \frac{B(s)}{B_m})^{1/2} ds \tag{5.4}$$

$$S_b = \int_{-\lambda_m}^{\lambda_m} (1 - \frac{B(s)}{B_m})^{-1/2} ds \tag{5.5}$$

For the electric field-related drift, the normal $E \times B$ drift as defined in Chapter 1 of this thesis and given by Equation 5.6 is used.

$$v_e = \frac{E \times B}{B^2} \tag{5.6}$$

If the equatorial displacement after half a bounce is larger than the gyroradius of the particle, then the latter will be the one defining the location of the outer boundary. The displacement was calculated for the ions covered in this study (H^+ and O^+ with energies from 1 keV to 1 MeV) and the results are plotted in Figure 5.6. The two curves show the equatorial displacement (black) and the particle's

gyroradius (red) and it can be seen that the gyroradius is consistently the smallest quantity. Thus, the outer boundary will be defined by the gyroradius and once the particles reach distances farther than this boundary they are simply removed from the simulation. The drift and gyroradius for different energies are presented in Table 5.1.

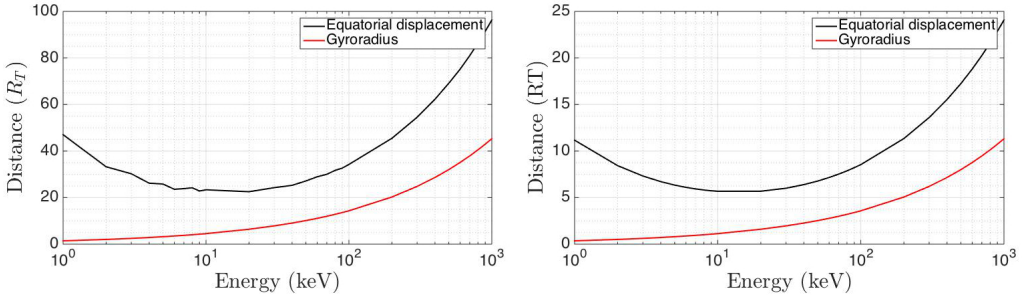

Figure 5.6: Equatorial half-bounce drift and gyroradius of O^+ (left) and H^+ (right) ions with respect to energy.

E (keV)	ED O^+ (R_T)	R_G O^+ (R_T)	ED H^+ (R_T)	R_G H^+ (R_T)
1	47.02	1.43	11.17	0.36
5	25.83	3.20	6.35	0.80
10	23.36	4.53	5.68	1.13
50	27.16	10.13	6.78	2.53
100	34.25	14.33	8.55	3.58
500	69.13	32.04	17.25	8.01
1000	96.28	45.3	24.07	11.32

Table 5.1: Equatorial displacement (ED) and gyroradius (R_G) for O^+ and H^+ ions with different energies.

Since the magnetospheric environment outside the interaction region but close to Titan is expected to be relatively stable, for the simulations, once the particle leaves the 15 R_T cube where hybrid code values are available, a simple extension of the upstream values given by the hybrid code output are used. A summary of these values is given in Table 5.2.

5.5 Results

The access of particles of different species and energies are presented here in the form of 2D equirectangular projections of Titan's exobase. Each map shows, in the

Parameter	Value
Saturn local time	3:00
Latitude of subsolar point	-19.06°
Upstream magnetic field vector	(3.73, 4.7, -2.15) nT
Upstream magnetic field strength	6.37 nT
Number density of upstream O^+	0.2 cm^{-3}
Number density of upstream H^+	0.1 cm^{-3}
Upstream plasma bulk velocity	120 km/s
Alfvénic Mach number	2.22
O^+ gyroradius	1.21 R_T
H^+ gyroradius	0.08 R_T

Table 5.2: Upstream plasma parameters for the hybrid code output (Feyerabend et al. 2015).

colour scale, the percentage of simulated particles that were able to reach the outer boundary as defined in the previous section. Since the tracings were performed backwards in time, a particle reaching this boundary (i.e. escaping the simulation domain) is equivalent to that particle being able to reach the exobase when coming from the magnetosphere.

The axes represent longitude (X-axis) and latitude (Y-axis) in Titan interaction system (TIIS, Neubauer et al. 2006; in TIIS, the X-axis points into the ideal corotation direction, the Y-axis towards Saturn and the Z-axis completes the right-handed system along the spin axis of the moon). The white vertical line represents the direction of the upstream flow as determined by the hybrid code simulations (ideal -34°, i.e. 146°) and the black vertical line represents the position of the magnetic tail (upstream flow + 180°, i.e. 326°). For each set of maps presented, the colour coding is represented using the same scale to easily visualise the effect that changes in energy and species have on the access of particles.

For all the maps presented in this section, the maximum access is always smaller than 100%. This is a consequence of using the backtracing technique, since some of the particles with initial velocity pointing towards the moon will reach the lower boundary and thus will be removed from the simulation.

5.5.1 Changes due to the distortion of the magnetic field

As previously mentioned, the distortion of the electromagnetic field arising from the presence of the conducting ionosphere has a noticeable effect on how the particles move around the moon and where they reach the exobase. To help visualise this effect, Figures 5.7 and 5.8 show the result of tracing 10 keV O^+ and H^+ ions respectively. Each figure is formed by three panels with the left panel showing the results for an uniform vertical field, the middle panel an uniform rotated field given by the upstream field of the hybrid code simulations and the right panel the full hybrid code output.

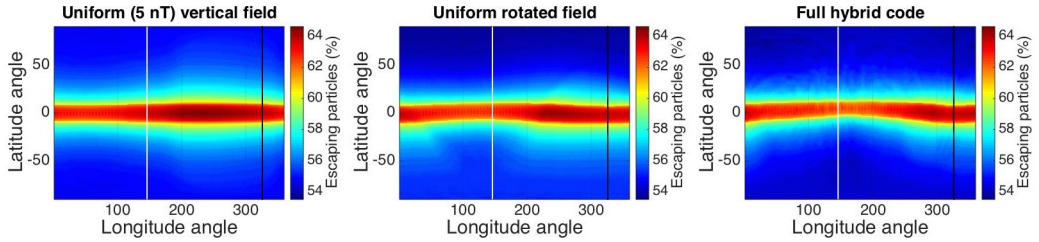

Figure 5.7: Access of 10 keV O^+ ions to Titan's exobase under three different magnetic field configurations: uniform vertical field (left panel), uniform rotated field (central panel) and full hybrid code representation (right panel). The white vertical line represents the location of the observed corotating flow and the black vertical line represents the location of the tail.

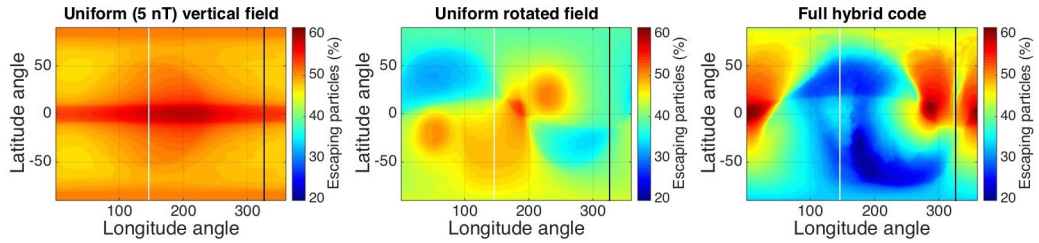

Figure 5.8: Access of 10 keV H^+ ions to Titan's exobase under three different magnetic field configurations: uniform vertical field (left panel), uniform rotated field (central panel) and full hybrid code representation (right panel). The white vertical line represents the location of the observed corotating flow and the black vertical line represents the location of the tail.

For both species, a symmetry with respect to the equator is present when the uniform vertical field is used but this symmetry starts to break down when the field is rotated. This changes are more visible for the case of H^+ ions due to the smaller gyroradius which causes the particles to follow more closely the magnetic field

lines. Furthermore, particles with smaller gyroradius are more affected by the enhancement of the magnetic field present in the pile-up region upstream of the moon, which is evident from the shielding observed for the case of H^+ ions with the full hybrid code output (right panel of Figure 5.8) and that has been described in previous works (Ledvina et al. 2005, Shah et al. 2009).

Since the geometry of the maps does not change significantly for the case of O^+ ions, using simpler descriptions of the field might be a sensible approach when studying particles with large gyroradii obtaining results that do not differ greatly from those obtained using a full hybrid code model at a much lower computational costs.

5.5.2 Access of particles with the full hybrid code output

The following maps show how energy-dependent the trajectories of charged particles in the electromagnetic field around the moon are. For all the maps in this sub-section the full hybrid code output was used for the background field and simulations for all the energy range (from 1 keV to 1 MeV) with logarithmic steps were run, even though only a limited set of results are presented since they fully illustrate the mentioned effect.

Figure 5.9 shows the results of the simulation of O^+ ions with four different energies, namely 1 keV, 10 keV, 100 keV and 1 MeV.

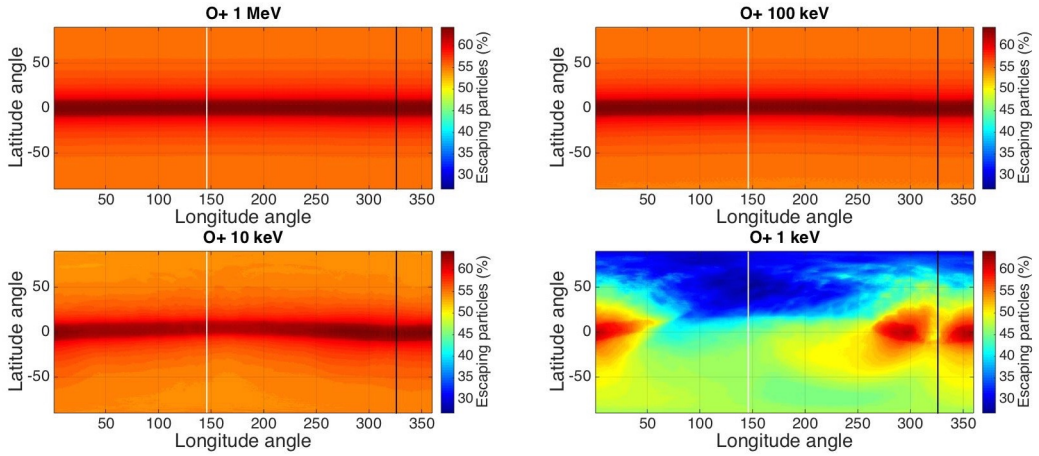

Figure 5.9: Access of O^+ ions with different energies to Titan's exobase. The white vertical line represents the location of the observed corotating flow and the black vertical line represents the location of the tail.

The same effect already shown in Figures 5.7 and 5.8 of the symmetry with respect to the equator is visible for the larger energies. The symmetry starts to break down at 10 keV with the appearance of a wave-like shape on the narrow band centred at 0° and for the lowest energy simulated (1 keV) the shielding effect is clearly present with a reduced access on the leading hemisphere.

The same effect is much clearer already for higher energies for the case of H^+ ions, depicted in Figure 5.10.

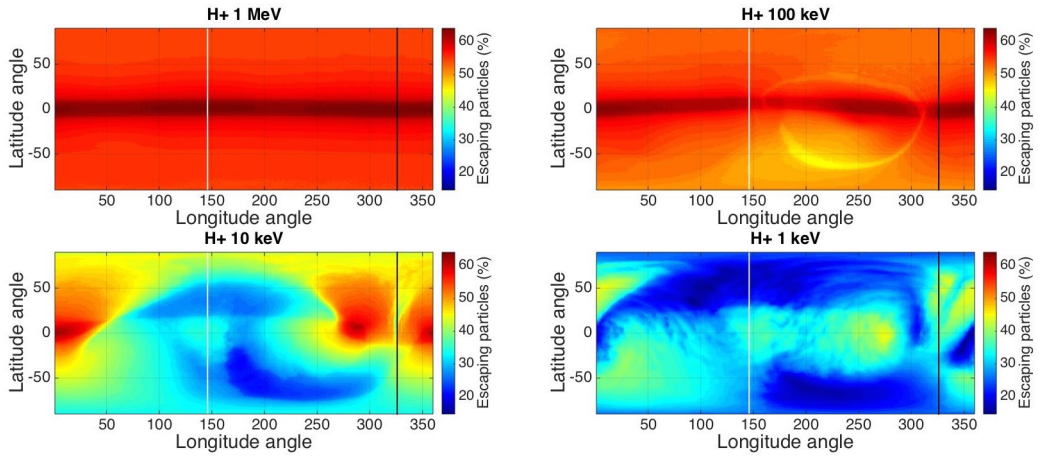

Figure 5.10: Access of H^+ ions with different energies to Titan's exobase. The white vertical line represents the location of the observed corotating flow and the black vertical line represents the location of the tail.

At 100 keV, the wave-like shape structure of the narrow band at the equator is already visible and the shielding is noticeable at 10 keV, with most of the moon shielded to the incoming ions of 1 keV.

The shielding has the effect of allowing more particles to access the trailing hemisphere compared to the leading hemisphere, something that, although counter-intuitive, has been reported before (e.g. Sillanpää et al. (2007)). By examining the magnetic field magnitude at the exobase (Figure 5.11), a correspondence between the areas with larger magnetic field and lower access can be observed.

All the plots presented show that the sole presence of Titan and the draping of the magnetic field around it has the ability of guiding particles of different species and energies in different ways and thus affecting the location around the moon where these particles will deposit their energy.

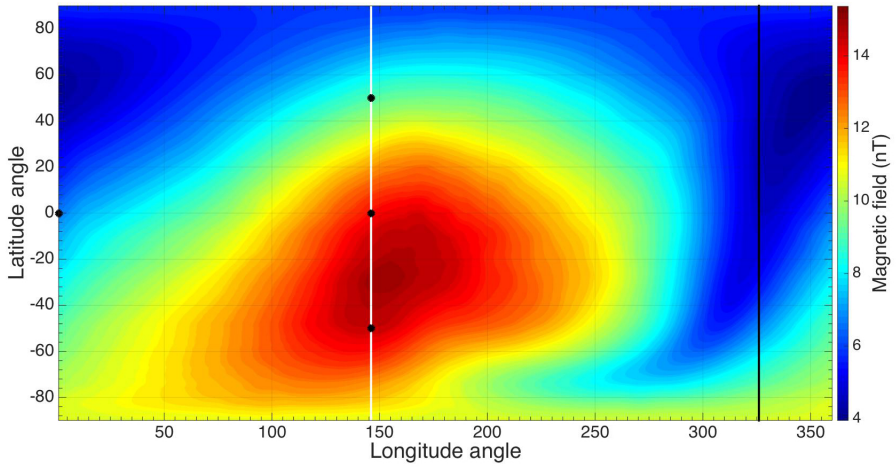

Figure 5.11: Magnetic field magnitude at the exobase as obtained from the A.I.K.E.F. code. The white vertical line represents the location of the observed corotating flow and the black vertical line represents the location of the tail. The four black marks correspond to the location where ionisation rates were calculated (see next section).

5.6 Calculating the incoming fluxes

To study the energy deposition and ionisation rates, four different positions around the moon were selected. These positions are indicated with the black markers in Figure 5.11. The locations were selected on the basis of how much variation the access of particles presents throughout the energy range covered. The latitude and longitude of the selected positions are listed in Table 5.3.

Position	Latitude (°)	Longitude (°)
Position 1	0	146
Position 2	50	146
Position 3	-50	146
Position 4	0	0

Table 5.3: Selected positions at the exobase around the moon for ionization rates analysis. The locations are indicated with black marks in Figure 5.11.

The variation in the access for each species at each of the selected positions is shown in Figure 5.12 with O^+ ions on the left panel and H^+ ions on the right. By comparing both plots, it is evident that the way the electromagnetic field affects each species is different. While the access remains relatively constant between 60° and 65° for O^+ ions at Position 4, at the same position, for the case of H^+ ions a

variation from around 20° for the lower energies up to more than 60° is obtained.

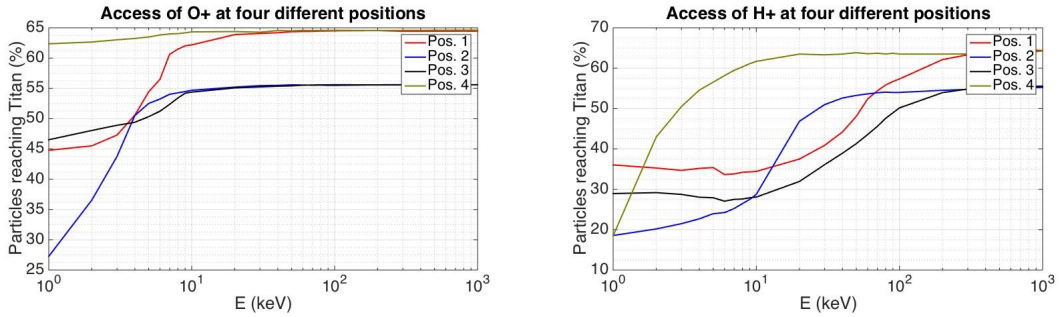

Figure 5.12: Access of particles (O^+ on the left, H^+ on the right) at selected positions around the moon as a function of energy. The indicated positions correspond to the ones listed in Table 5.3.

Figure 5.13 shows the upstream O^+ and H^+ fluxes as detected by the Cassini MIMI/CHEMS instrument together with fitting curves. The fluxes shown are averaged over a period of one hour before CA, specifically between 17:00 and 18:00. This time window was chosen specifically to avoid Titan's interaction region, that can be distinguished by the region with highly disturbed magnetic field data near closest approach in Figure 5.14.

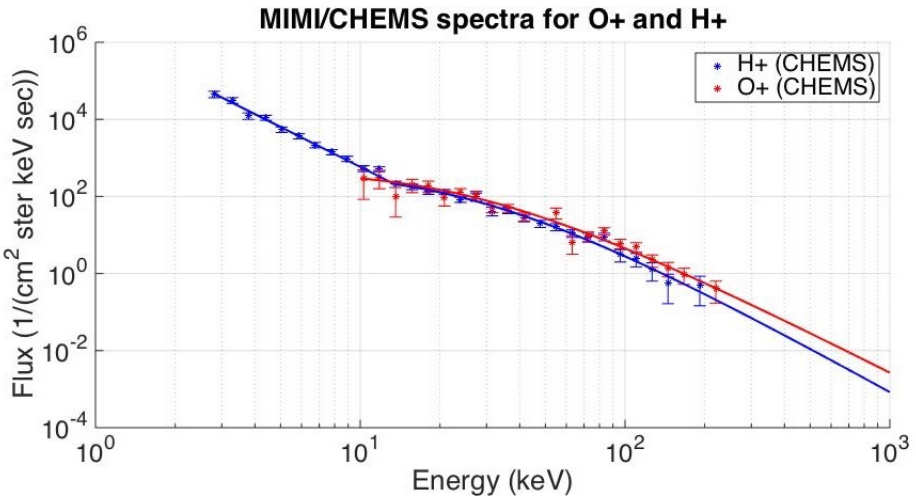

Figure 5.13: Upstream O^+ and H^+ fluxes during T9 flyby as captured by the MIMI/CHEMS instrument onboard Cassini. The markers show the data points and the solid lines are modified Kappa distribution fittings to the data.

A modified Kappa distribution (Dialynas et al. 2009, Equation 5.7) was fitted to the data points obtained by the instrument for all the energy range covered in the

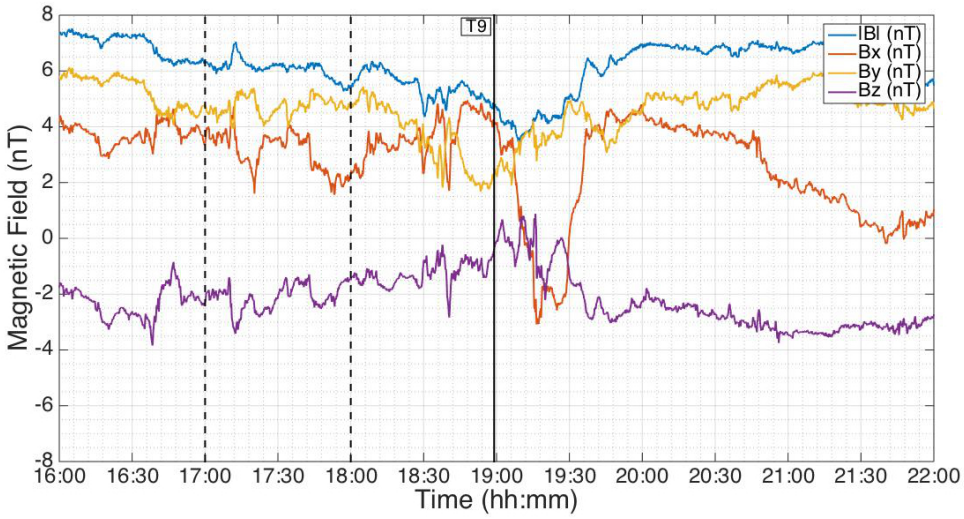

Figure 5.14: Magnetic field data in TIIS coordinates three hours before and after closest approach. The dashed vertical lines indicate the boundaries of the time period from which the MIMI/CHEMS spectra shown in Figure 5.13 were obtained.

case O^+ ions and a combination of a power law for the low energies and the same modified Kappa distribution for the higher energies in the case of H^+ ions.

$$j = C \cdot E[E + kT(1+\gamma_1)]^{-(1+\gamma_1)} \tag{5.7}$$

The energy range varies between both species because the low energy O^+ ions cannot be sufficiently deflected inside the instrument to allow detection (2.8 keV to 220 keV for H^+ ions and from 10.3 keV to 220 keV for O^+ ions). The fit was then extrapolated to cover the energies up to 1 MeV.

By combining the spectra presented in Figure 5.12 with the ones presented in Figure 5.13, the expected fluxes at the selected positions around the moon can be obtained.

5.7 Energy deposition and ionisation rates

For each of the four selected positions shown in Figure 5.11, one spectrum for the access of H^+ and one for the access of O^+ throughout the energy range covered in the study were obtained. These spectra are shown in Figure 5.12.

From the plots is visible the role that the gyroradius plays on the access of particles. For all the cases, as the energy increases (gyroradius becomes larger), the

access increases asymptotically until it reaches a maximum value that depends both on particle species and location on the moon.

In order to calculate the energy deposition and ionisation rates, the estimated incoming fluxes were calculated for each one of the four selected positions by combining the spectrum obtained by MIMI/CHEMS shown in Figure 5.13 with the spectra from Figure 5.12, giving the normalised spectra shown in Figure 5.15.

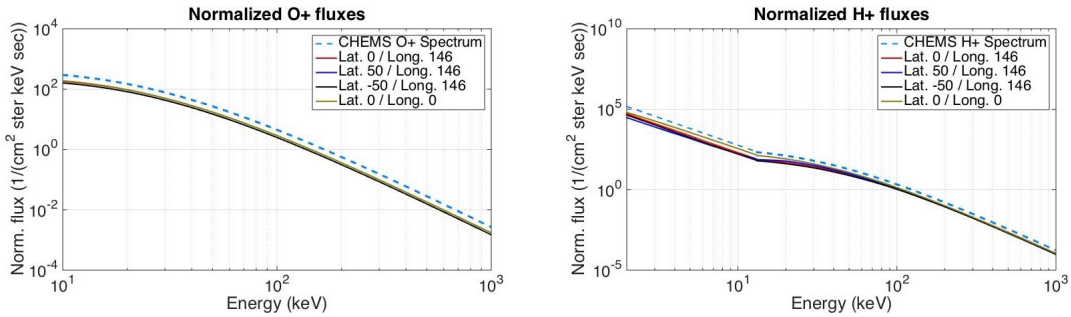

Figure 5.15: Estimated incoming fluxes at the four selected positions (solid lines) showing the upstream fluxes measurement from the MIMI/CHEMS instrument (dashed line).

These fluxes are then taken as an energy input into the atmosphere and are propagated directly downwards at the exobase to calculate the energy deposition and ionisation rates at the given locations.

For the atmosphere, a single species model consisting of molecular nitrogen (N_2) was considered. The altitude profile, shown in Figure 5.16, was taken from an engineering model developed by Yelle et al. (1997) as a preparation for Cassini's arrival at Saturn.

Stopping powers for H^+ and O^+ ions in molecular nitrogen obtained from the SRIM (Stopping and Range of Ions in Matter) software (Ziegler et al. 2010) were used. The stopping powers are calculated by combining experimental data with Monte Carlo simulations, providing values for energy ranges where purely experimental data are not available.

The values used for the calculations presented here are shown in Figure 5.17, with the ones for O^+ ions shown in blue and those for H^+ ions shown in red.

From Figure 5.17 it can be seen that the overall behaviour of the stopping powers for both ion species differs with energy. Whereas for the case of H^+ the stopping

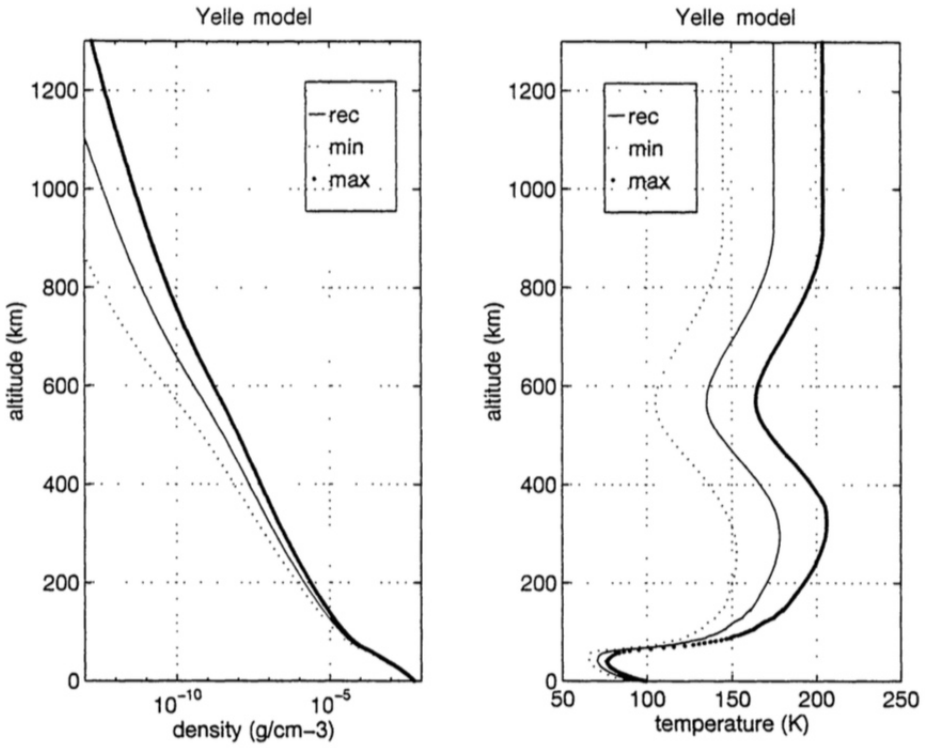

Figure 5.16: Density and temperature profiles from the Yelle engineering model (Yelle et al. 1997). The three curves on each panel correspond to three cases provided on the model, namely minimum (min), maximum (max) and recommended (rec). For the present analysis the recommended density profile was used.

power of N_2 reaches a maximum close to 100 keV for O^+ there is a steep increase right after that same energy. Additionally, due to the smaller cross section, the stopping power for H^+ is lower throughout the whole energy range which translates into the possibility for H^+ ions to penetrate deeper into the atmosphere and thus to deposit their energy at lower altitudes.

Using the method described at the beginning of this chapter, integrated energy deposition and ionisation rates for O^+ and H^+ ions with energies larger than 10 keV were calculated. The results are shown in Figures 5.18 and 5.19 respectively.

The left panel of each figure shows the ionisation rates (X-axis) vs. altitude (Y-axis) while the right panels show a weighted difference between the different positions that help illustrate the influence of the magnetic field lines draping.

A difference that is present between both species at every position is the altitude. While the peak in ionisation rates by O^+ ions lies at approximately 900 km,

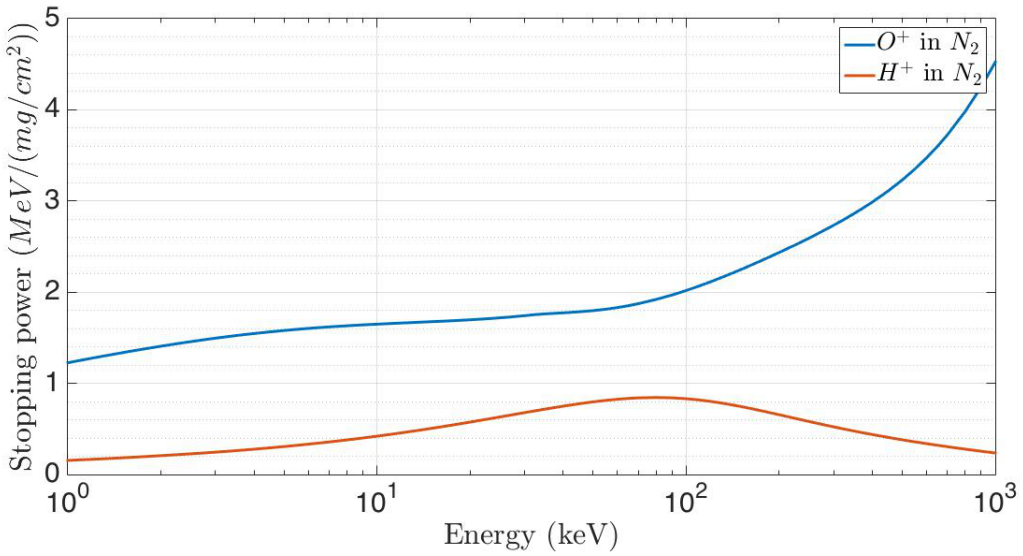

Figure 5.17: Stopping powers of O^+ (blue curve) and H^+ (red curve) in molecular nitrogen (N_2) as obtained from the SRIM software (Ziegler et al. 2010).

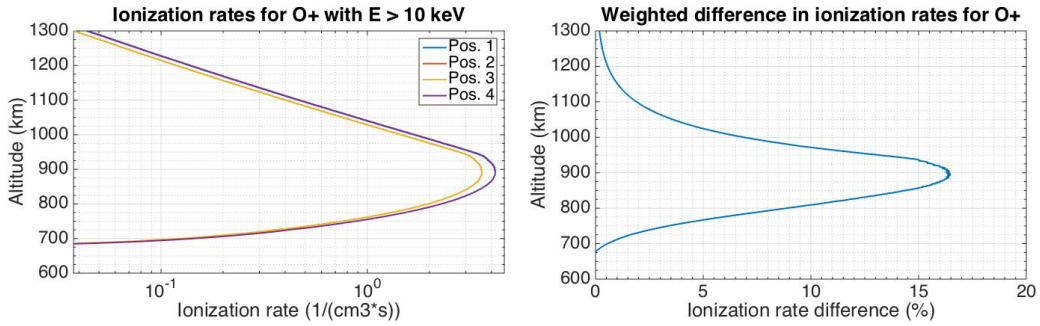

Figure 5.18: Ionisation rates of N_2 by O^+ ions at the four selected positions (left) and weighted difference between the location with the highest and lowest ionisation rates (right).

for the case of H^+ ions it lies at approximately 825 km. This difference in altitude is a consequence of the larger stopping power of the atmosphere against O^+ compared to H^+, thus allowing the lighter ions to penetrate deeper into the atmosphere before loosing its energy.

The ionisation rate values for both species are similar, with the peak for Position 4 (the maximum peak) at around 4 $ions/(cm^3 \cdot s)$. A large change is present in the difference between the maximum and the minimum ionisation rate peaks for the different positions. While the difference between Positions 3 and 4 for the case of O^+ ions is less than 1 $ions/(cm^3 \cdot s)$, for the case of H^+ it is almost 2 $ions/(cm^3 \cdot s)$.

To better illustrate this last point, a weighted difference between the maximum

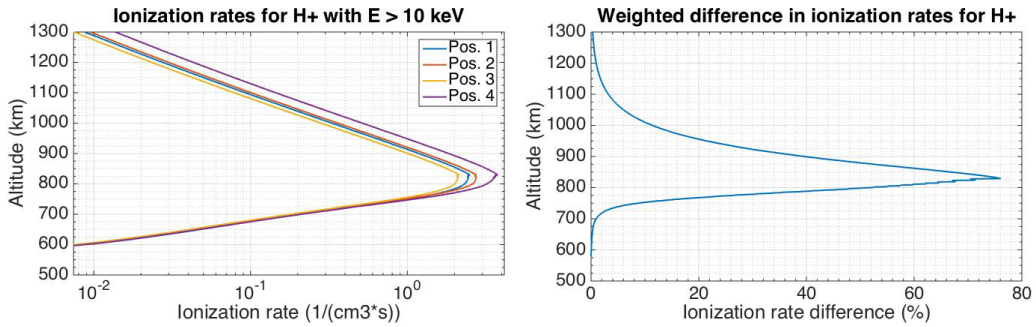

Figure 5.19: Ionisation rates by H^+ ions at the four selected positions (left) and weighted difference between the location with the highest and lowest ionisation rates (right).

and minimum ionisation rate curves was calculated for both species. This weighted difference was calculated for each species by taking the maximum and minimum value at each altitude between the four ionisation rate curves and then applying Equation 5.8, where w_δ represents the altitude-dependent weighted difference, R_{max} and R_{min} represent the altitude-dependent maximum and minimum ionisation rate and R_{MAX} represents the absolute maximum of the ionisation rate for all the altitudes (maximum ionisation rate peak).

$$w_\delta(h) = R_{max}(h) \cdot \frac{R_{max}(h) - R_{min}(h)}{R_{min}(h)} \cdot R_{MAX}^{-1} \tag{5.8}$$

The reason for not using simple differences is because these can be rather large at higher altitudes where the ionisation rates are low and thus the result would not be representative of the overall difference in ionisation rates.

From both weighted difference curves (right panels in Figures 5.18 and 5.19) it can be seen that by only taking into account the draping of the field lines and the local disturbances of the electromagnetic field, both included in the hybrid code output, a significant difference in ionisation rates from energetic ions can be expected at different regions around the moon.

For the case of precipitating O^+ ions, a difference of about 15% at the peak altitude of 900 km is observed. This difference is even larger for the case of H^+ ions, with a value of almost 80% at the peak altitude of 820 km.

The significance of these results in relation to the local ionospheric densities

needs to be evaluated by taking into account the importance of the ionisation rate by energetic ions with respect to, for instance, magnetospheric electrons or solar extreme ultraviolet (EUV). This can be seen in Figure 5.20, where data for solar EUV (on the dayside) as well as from electrons and protons for T5 conditions are shown together with the curves calculated in this thesis. The curves for solar EUV, electrons and protons for T5 were obtained by a digitisation of Figure 3 from Cravens et al. (2008).

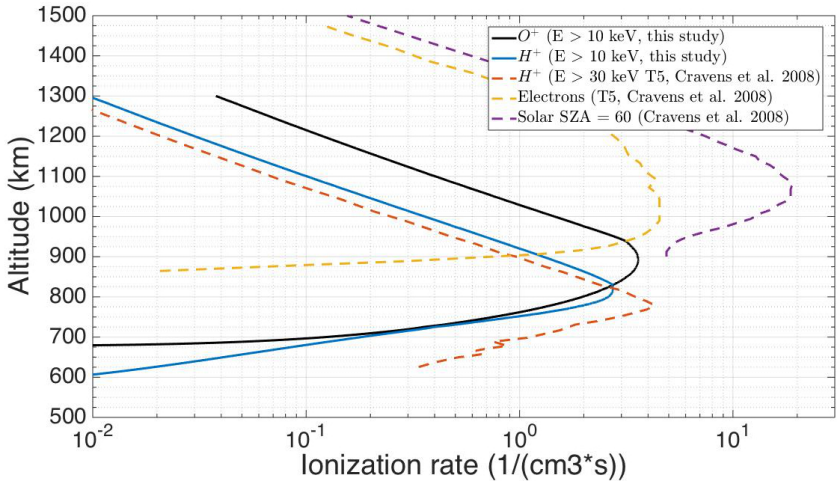

Figure 5.20: Ionisation rates by altitude from different sources. The two solid lines show the results presented on this thesis for O^+ (black) and H^+ (blue). The dashed lines show values presented in Cravens et al. (2008) for solar EUV with a solar zenith angle (SZA) of 60° (purple), H^+ for T5 conditions (red) and electrons for T5 conditions (yellow).

Above 900 km, on the dayside photoionisation dominates over any other process by more than an order of magnitude. However, the situation is different below 900 km, where the contribution of magnetospheric ions and electrons becomes comparable, even though each of them peaks at different altitudes.

A further analysis including the contribution by electron impact ionisation needs to be undertaken in order to estimate the real impact of the results presented in this chapter, especially for the low altitude nightside ionosphere.

Chapter 6

Pickup ions in the vicinity of Titan

The contents of this chapter were published in Regoli et al. (2016).

A fundamental process among all the Solar System bodies with an atmosphere or even a tenuous exosphere is the loss of mass to the surrounding environment through different physical processes. These processes can be divided into atmospheric (for neutral particles) and ionospheric (for charged particles) escape.

When dealing with atmospheric escape, the Jeans parameter is useful to characterise the dynamics of the escape processes. The Jeans parameter represents the ratio of gravitational bound to thermal energy of a given population. It is represented by λ and is calculated using Equation 6.1 (Strobel and Cui 2014), where v_{esc} is the escape velocity, U is the particle's most probable velocity, G is Newton's gravitational constant, M is the mass of the planet, m is the mass of the particle, k is the Boltzmann's constant and T is the atmospheric temperature.

$$\lambda(r) = \frac{v_{esc}^2}{U^2} = \frac{GMm}{kT(r)r} \tag{6.1}$$

The lower the value of λ, the easier it is for a given species to escape from the planet's gravitational pull. For small values of λ ($\lambda <\sim 50$, Johnson et al. 2009), a constant outflow of neutrals is present in what is called a hydrodynamic escape. For larger values, the escape happens in a more random way with individual particles reaching escape velocity in what is known as Jeans escape.

Table 6.1 shows values of λ at the exobase for the main constituents of Titan's exosphere for different temperature values (Strobel and Cui 2014). In general at

Table 6.1: Values of Jeans parameter (λ) for different exospheric constituents at Titan's exobase (Strobel and Cui 2014).

Temperature (K)	H	H_2	CH_4	N_2
110	2.4	4.8	39	67
140	1.9	3.8	30	53
190	1.4	2.8	22	39

Titan λ is relatively large, with the lowest value for atomic hydrogen being close to the lower boundary of $\lambda = 2.1$ for an atomic gas as reported by Volkov et al. (2011). This results in Jeans escape being the dominating escape process and has been further confirmed by Tucker and Johnson (2009) using the direct simulation Monte Carlo (DSMC) method to study the escape process.

Recent reviews of atmospheric escape rates can be found in Johnson et al. (2009) and more recently in Strobel and Cui (2014). Due to the differences in Jeans parameter values, there is a large variation between the escape rates of different species. While the thermal escape of N_2 has been estimated to be of the order of $10^{11} N_2 \cdot s^{-1}$, H_2 molecules, due to their lighter molecular mass, experience a much larger escape rate with its mean value estimated at $9.2 \times 10^{27} H_2 \cdot s^{-1}$ by Cui et al. (2011) and Strobel (2009) using two different methods. For the case of H atoms, the Jeans escape rate was estimated by Hedelt et al. (2010) to be $1.74 \times 10^{27} H \cdot s^{-1}$.

For CH_4, the second main constituent of Titan's atmosphere, escape rates of the order of $10^{27} CH_4 \cdot s^{-1}$ were inferred by Yelle et al. (2008) and Strobel (2009). This is, however, not consistent with observations made by Cassini and the possibility of chemical losses from interactions with magnetospheric particles seems to be ruled out by the relatively low particle fluxes detected by Cassini at Titan's orbit (Strobel and Cui 2014).

In terms of ionospheric escape, there are three main processes contributing to mass loss, namely bulk ionospheric escape (low-energy ion escape along the tail), polar wind and pickup ion escape. Polar wind is a process by which photoelectrons escape along magnetic field lines creating an ambipolar field that helps accelerate ions to velocities that are larger than the body's escape velocity, thus creating a con-

stant outflow of ions of different species. Finally, ion pickup is a process by which ions of initially relatively small velocity are affected by the local electromagnetic field and consequently accelerated in the direction of the local electric field (which is nominally in quadrature with the magnetic field). The particles are then picked up by the magnetic field, leaving the body on a cycloidal trajectory according to the Lorentz force. In an homogeneous magnetic field configuration, this means that recently created pickup ions will have a pitch angle of 90°, assuming a pickup ion velocity much larger than the thermal velocity.

Pickup ions have been extensively studied at many solar system objects including comets (e.g. Coates et al. 1993, Coates and Jones 2009), some of the Jovian moons (e.g. Huddleston et al. 2000, Crary and Bagenal 2000) and the Saturnian moons (e.g. Teolis et al. 2010, Tokar et al. 2012). They can also contribute further with atmospheric escape by precipitating back into the moon due to gyroradii effects and further heating the exosphere and sputtering neutral particles (Tseng et al. 2008, Michael et al. (2005)).

Figure 6.1 shows the trajectories of H_2^+ and O^+ pickup ions at Titan on the TIIS coordinate system. The simulation was run using the background electromagnetic fiels for the T70 flyby from a hybrid code run (A.I.K.E.F., Müller et al. (2011), Feyerabend et al. (2015)). For the case of Saturn, the corotation electric field ideally points away from the planet (negative Y-axis) and thus an asymmetry arises since ions that are picked up on the Saturn side of the moon have a higher probability to re-enter the atmosphere (especially heavier ions with larger gyroradius) further contributing to the energy deposition (Tseng et al. 2008).

Polar wind ionospheric escape has been studied using data from three distant tail flybys (T9, T63 and T75) by Coates et al. (2012). By estimating plasma densities (n_{ELS}) using CAPS/ELS, velocities (v) using numerical calculations of the ion moments from CAPS/IMS (Thomsen et al. 2010) and an escape area (A) constrained by the width of the tail crossing, they estimated the ionospheric escape rate (Q) to be of the order of $10^{24} ions \cdot s^{-1}$ using Equation 6.2.

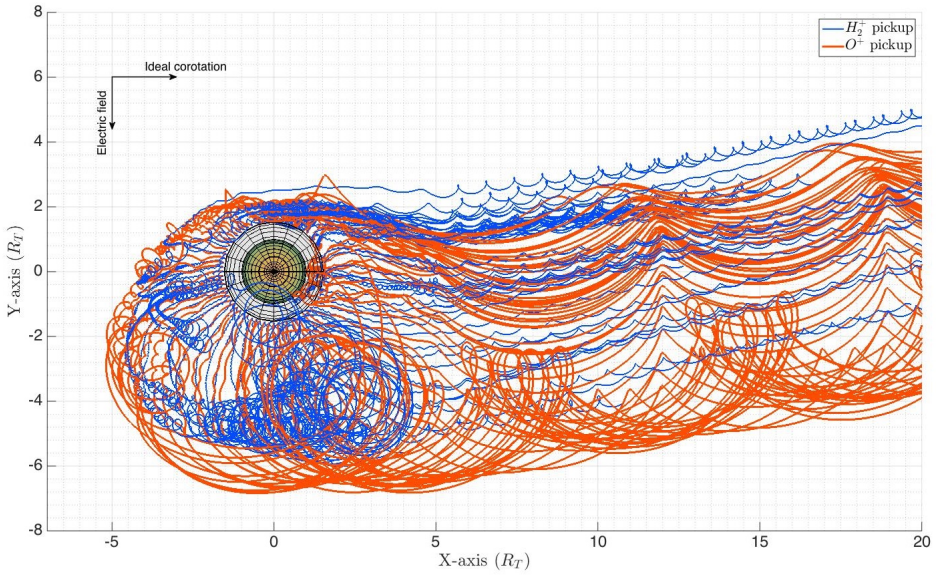

Figure 6.1: Pickup ions trajectories starting at Titan. The trajectories start at the exobase (1450 km, transparent grid on the plot) and are initially accelerated in the direction of the corotation electric field and finally convected towards the tail. The plot is shown in TIIS coordinates and the ions were propagated on a background field from a hybrid code simulation for the Cassini T70 flyby. Notice the asymmetry between the Saturn side (positive Y-axis) and the anti-Saturn side (negative Y-axis).

$$Q = n_{ELS} \cdot v \cdot A \tag{6.2}$$

Other estimations of ionospheric escape have been made using the T9 and T18 flybys by Sittler et al. (2010) and the TA and TB flybys by Wahlund et al. (2005). In the first study, they estimated escape rates of $\sim 4 \times 10^{24} ions \cdot s^{-1}$ whereas on the second a value of $10^{25} ions \cdot s^{-1}$ was obtained.

6.1 Ion cyclotron waves

The initial pitch angle distribution is known as a ring distribution in velocity space. This distribution arises from the fact that an ion population at different gyrophases and pitch angle of 90°, when seen in velocity space, will form a ring centred initially at the thermal velocity of the original ion population. The population will then be accelerated to the corotating plasma flow velocity.

This distribution is unstable to wave generation, leading to the appearance of ion cyclotron waves (ICWs) and the scattering in pitch angles from the original ring distribution to a shell distribution. The ring and subsequent shell distributions in velocity space are depicted in Figure 6.2 for the case of the interaction between a comet and the solar wind (Coates et al. 1990).

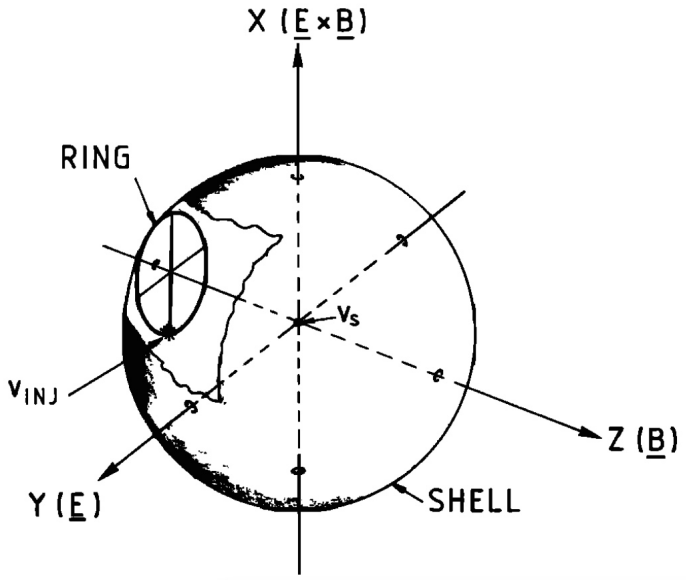

Figure 6.2: Ring and shell distributions of pickup ions arising from the interaction of a cometary exosphere with the solar wind Coates et al. (1990).

One particularity of Titan's environment is that, even when the ions are being picked up, no ICWs are observed in most of the available datasets. At the time of writing this thesis, with 114 dedicated flybys by Cassini, ICWs had been observed in only two of them, namely T63 and T98 (Russell et al. 2016). The reason for this is yet not well understood. Cowee et al. (2010) argued that the lack of wave signatures in the data could be due to the amplitude of the waves being too small and thus being buried in the noisy magnetic environment present at Titan or due to the convection time of the magnetic field lines being too short and thus not giving time for the waves to fully grow before leaving the interaction region.

Figure 6.3 shows Lomb-Scargle periodograms for two different flybys. On the left hand side, the power spectrum for T63 (one of the two flybys where ICWs were observed) is shown, where an enhancement immediately below the gyrofrequency of H_2^+ can be observed. On the right hand side, a typical case for Titan is shown,

where no clear enhancement is observed at any frequency. The peak present in both plots above 100 Hz is present in many of the flybys and has, most probably, an instrumental origin.

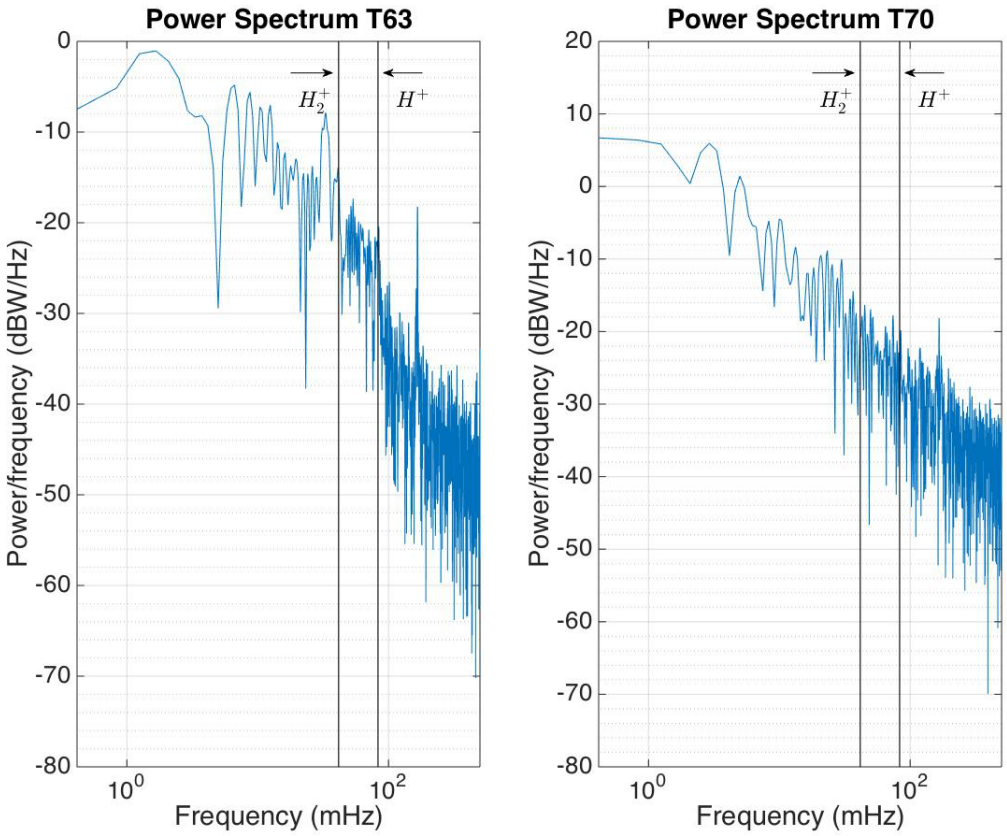

Figure 6.3: Lomb-Scargle spectrograms of magnetic field data for T63 (left panel) and T70 (right panel).

Due to the absence of the waves, other methods to study the ion pickup at Titan are needed. This study focuses on the thermal plasma data from the CAPS/IMS instrument on-board Cassini.

6.2 Pickup ions signatures in plasma data

The first report on the signatures left by freshly picked up ions in the CAPS data is from Hartle et al. (2006). In their study, they looked at data from the first Titan flyby by Cassini (TA) and compared it with the Voyager 1 flyby. In spectrograms of the IMS singles data, they observed the presence of signatures with a narrow

distribution in energy and they interpreted these as being due to ions that are still in the early stages of the pickup process and thus have not yet been scattered in energy into a shell distribution.

These signatures can be observed during several flybys. An example from T70 is shown in the middle panel in Figure 6.4 with the signatures circled in white. The panel shows a spectrogram of the singles data from anode 4 during the flyby. The other two panels show an average of the counts per anode (top panel) and the instantaneous pitch angle for anode 4 (bottom panel).

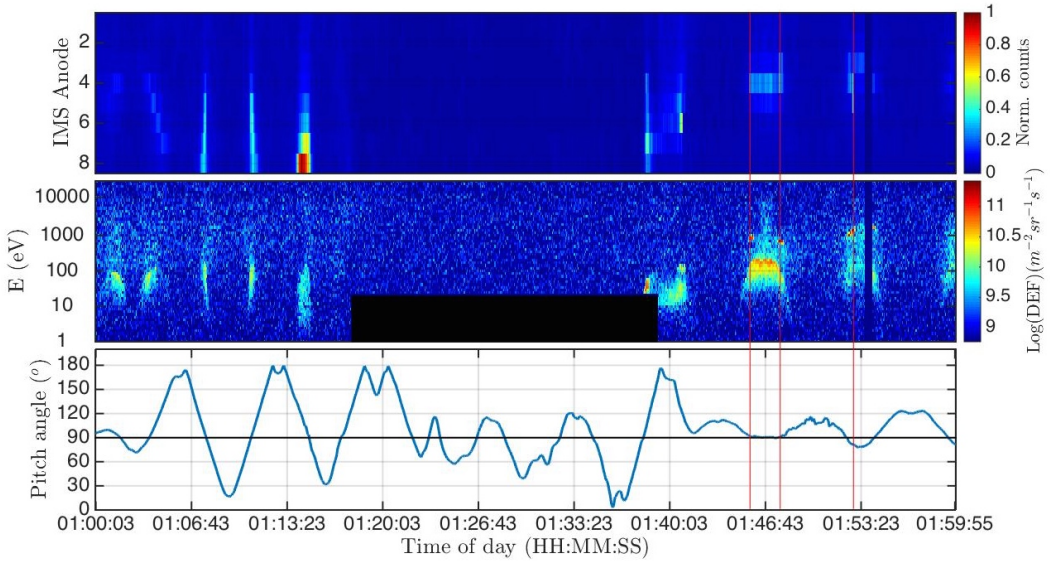

Figure 6.4: Ion data during T70 flyby. Normalised counts for the 8 anodes from CAPS/IMS (top panel), ion spectrogram in differential energy flux (DEF) units for anode 4 (middle panel) and instantaneous pitch angle as measured by anode 4 (bottom panel).

The reason for looking at the average of the counts per anode is to make sure that the signatures are not coming from the corotating plasma (if that were the case, a clear enhancement in the counts would be seen at any of the anodes). This gives a hint that the ions might be originating at Titan. This is further supported by looking at the angular distribution of the observations made by CAPS/IMS shown in Figure 6.5. The left panel shows the angular distribution at the moment of the detection of one of the signatures interpreted as pickup ions while the right panel shows the distribution once outside the interaction region, far from Titan. It can be seen that the enhancement in the fluxes during the detection of the signatures is clearly not

coming from the corotation direction, while later on, once the interaction region is left behind, the enhancement has moved towards the corotation direction. Additionally, the pitch angle coverage shows that the narrow signatures have a distribution of 90°, further supporting the theory of a ring distribution.

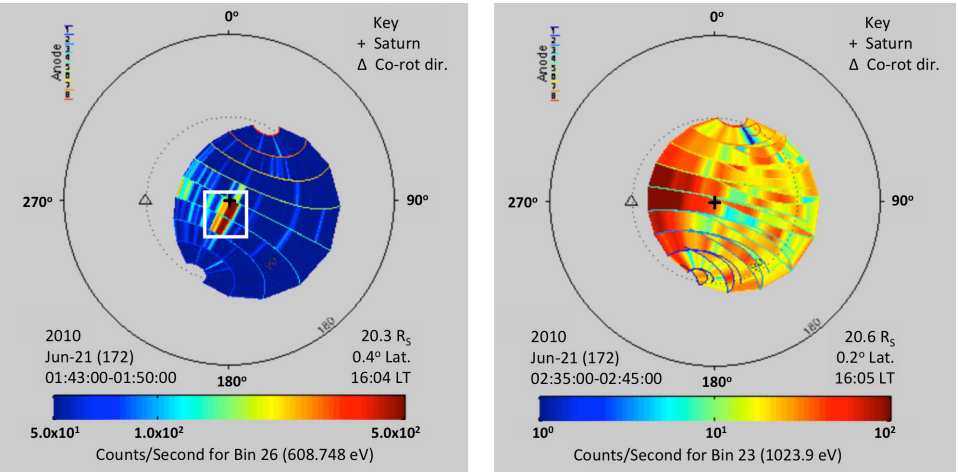

Figure 6.5: Angular distribution of the ion measurements by CAPS/IMS. The left panel shows the distribution during one of the detections of the features interpreted as freshly produced pickup ions (marked with a white rectangle). The right panel shows the distribution upstream of Titan (outside the interaction region). In both figures, the plus sign in the middle shows where Saturn is located while the triangle shows the direction of the incoming plasma under ideal corotation conditions.

The lower energy population observed in the middle panel of Figure 6.4 corresponds to ionospheric ions flowing out from Titan as well, but the distribution has been broadened in both energy and pitch angle. To understand why, inspection of the time-of-flight (TOF) data provided by the CAPS/IMS instrument is necessary in order to identify the species being observed.

Figure 6.6 shows the plasma composition as obtained from the coincident TOF data for six different periods of time before (first two panels on top) and after (four remaining panels) closest approach (CA). Since Cassini flies through the ionosphere during CA, these data were intentionally omitted for the analysis.

Saturn's corotating plasma in the outer magnetosphere close to Titan's orbit is composed mostly of H^+, H_2^+ and O^+ (Thomsen et al. 2010). During the approaching phase of the flyby, it can be seen that the $m/q = 2$ densities are enhanced with

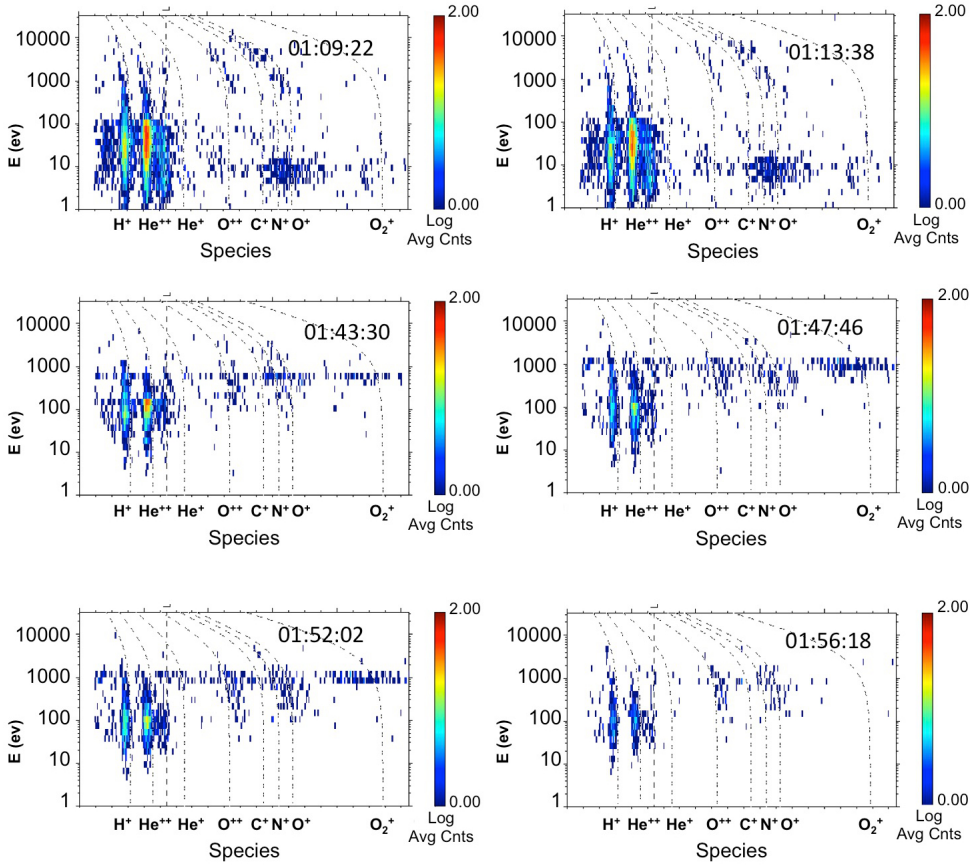

Figure 6.6: Coincident TOF data from the CAPS/IMS instrument showing counts vs. mass/charge during six different periods while Cassini was flying through the interaction region (two first panels) and after (four final panels). The solid line ovals show the $m/q = 2$ population and the dashed line ovals show the $m/q \sim 16$ population.

respect to $m/q = 1$. This is interpreted as outflowing H_2^+ coming from Titan. Additionally, closer to the point of CA, an enhancement on the $m/q \sim 16$ component can be observed. This is interpreted as plasma originating from Titan as well, even though the composition cannot be precisely determined using CAPS/IMS due to the low mass resolution, not allowing to distinguish between CH_3^+, CH_4^+ or CH_5^+ (Westlake et al. 2012). The possibility of these ions being O^+ can be ruled out due to the absence of significant amounts of oxygen in Titan's atmosphere as well as the absence of a clear O^{++} signature which is left as an instrumental fingerprint in the presence of O-bearing molecules.

To further constrain the origin of the plasma leaving the signatures, a test par-

ticle simulation on a background field produced by A.I.K.E.F. was run for the time period between 01:40:00 and 01:50:00 (comprising the two signatures encircled together in Figure 6.4). The simulation was a back-tracing of m/q 16 ions with energies from 500 eV to 1 keV from the position of the instrument taking into account the look direction and field of view. The choice of heavy ions was made because, as mentioned earlier, the focus of the study is ions being detected during the early stage of the pickup process and lighter ions will have already undergone many gyrations by the time they reach the instrument, and thus most probably scattered into a more widely-spread distribution.

Figure 6.7 shows the result of the simulation from two different points of view. The dotted line corresponds to Cassini's trajectory. The solid orange lines correspond to particles that are coming from the magnetosphere and the blue lines to particles that seem to originate at the exobase (transparent grid surrounding Titan at an altitude of 1450 km).

It can be seen that the ions reaching the instrument seem to have originated both in the magnetosphere and in the exosphere of the moon. However, the fact that the environment around Titan during the flyby was rather poor in O^+ supports the idea that the real origin of the ions leaving the signatures in the plasma data is the moon's atmosphere.

This is also supported by taking into account the look direction of the instrument during the detection of the narrow signatures. Figure 6.8 shows the trajectory of Cassini during the T70 flyby with the instantaneous look direction of CAPS/IMS. The locations where the signatures are detected, as well as the broad population before CA, are highlighted in red.

Since the corotation electric field is pointing away from the moon, the look direction of the instrument during the detection is consistent with ions being picked up at the exosphere of the moon and being directed towards the instrument. This is different from the locations where the population with broad energy distribution are detected before CA. At those times, CAPS/IMS is actually pointing away from the moon, towards Saturn, where a detection of pickup ions would be incosistent

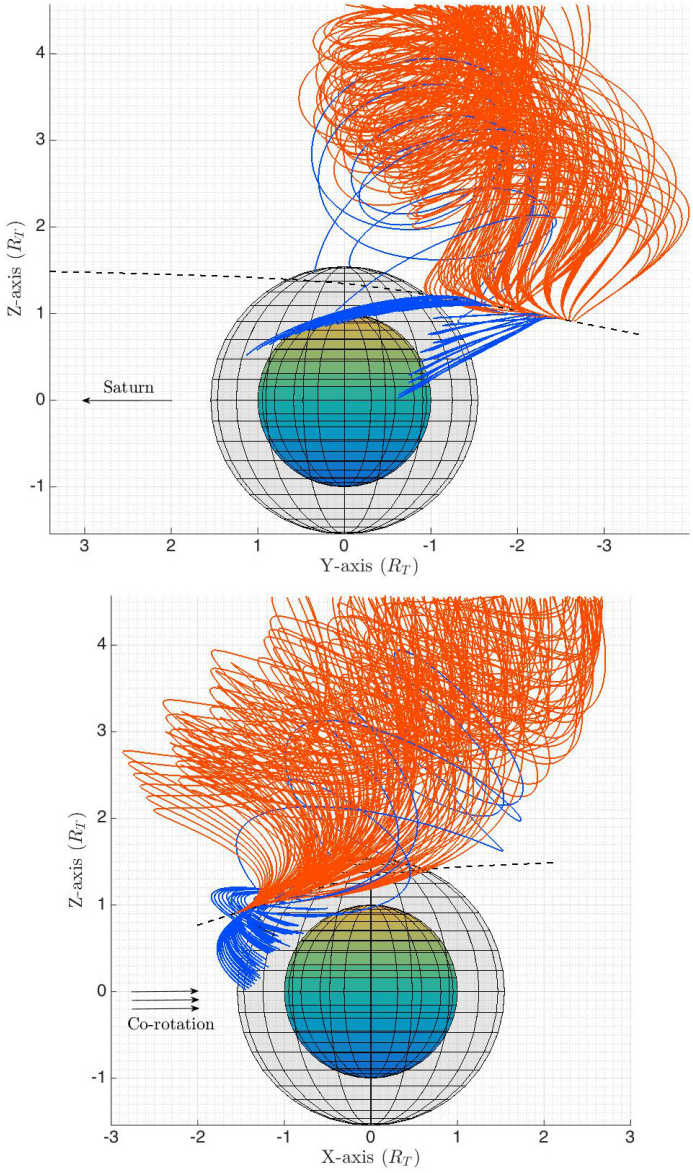

Figure 6.7: Trajectories of ions back-traced from the CAPS/IMS position during the T70 flyby as seen from the corotation direction (top panel) and from the anti-Saturn side (bottom panel). The sphere at the centre depicts Titan with a surrounding transparent grid representing the exobase (at 1450 km). The dotted line shows Cassini's trajectory during the flyby and the solid lines show the ion trajectories with the orange ones corresponding to ions of magnetospheric origin and the blue ones coming from Titan.

with the direction of the local electric field, suggesting that the ions are of magnetospheric origin.

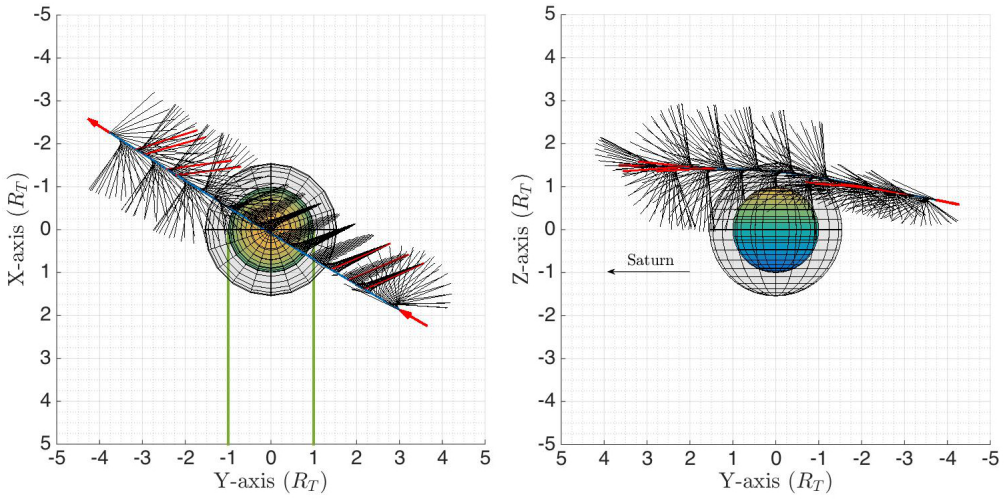

Figure 6.8: Instantaneous look direction of the CAPS/IMS instrument during the T70 flyby. The red arrows indicated the flight direction. The four thick red lines in the outbound part of the trajectory are the four locations where the narrow signatures interpreted as pickup ions are observed while the three lines in the inbound part of the trajectory indicate the locations where the broad populations are detected (Figure 6.4).

6.3 Pickup ion signatures around Titan

A survey of freshly picked up ion signatures was carried out for all the flybys with valid CAPS/IMS data. Since CAPS was turned off in 2012, the last flyby for which data are available is T83. Valid data are available for 73 of those 83 flybys and, of these 73 flybys, clear signatures were observed in 27 of them. The locations of these signatures, together with the flyby trajectores is shown in Figure 6.9.

In the figure, a strong asymmetry is evident, with all the signatures observed located on the anti-Saturn side. This is the hemisphere where the ideal corotation electric field is pointing to, something that has been shown to generally be a good approximation (Arridge et al. 2011a).

6.4 Pickup ion outflow from Titan's ionosphere

To estimate the contribution to the overall ionospheric escape by freshly produced pickup ions, three different planes perpendicular to the ideal corotation direction located at distances from Titan's centre of 1.0 R_T, 1.6 R_T and 2.4 R_T were defined. The boundaries of the planes are defined by the positions where Cassini crossed

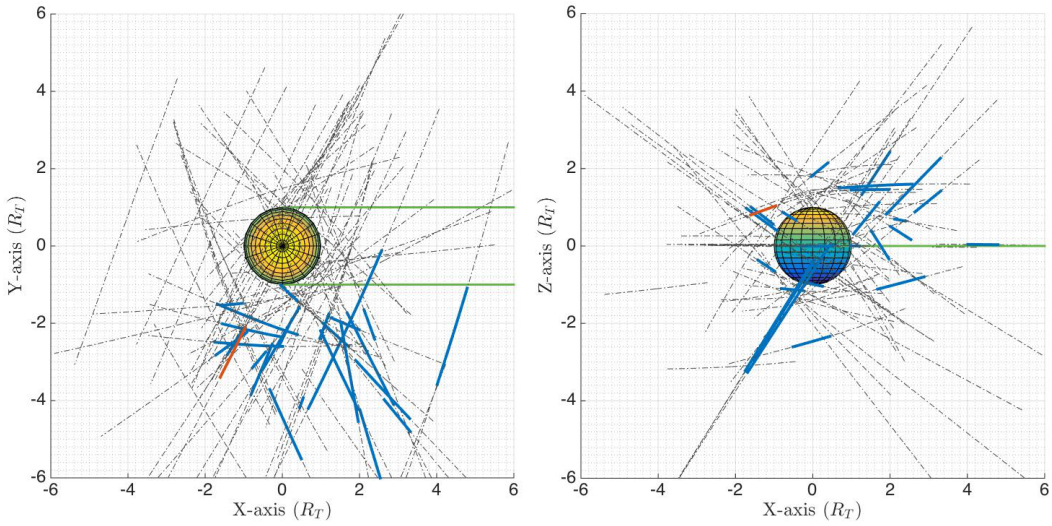

Figure 6.9: Polar (left panel) and side (right panel) views of Titan showing the regions where freshly produced pickup ion signatures are observed. The dashed lines show Cassini's trajectory during the different flybys. The blue lines show the location where the reported signatures were observed and the red line shows the location of the signatures specifically for the T70 flyby (further analysed in the text). The parallel green lines show the nominal location of the plasma tail.

Table 6.2: Coordinates of corners and areas of planes used to calculate fluxes. The coordinates are given as (X,Y,Z) vectors in units of R_T. The areas are given in units of R_T^2.

Plane	Corner 1	Corner 2	Corner 3	Corner 4	Area
	1.00	1.00	1.00	1.00	
X = 1	-4.08	-4.08	-1.75	-1.75	3.56
	0.00	1.53	1.53	0.00	
	1.60	1.60	1.60	1.60	
X = 1.6	-3.63	-3.63	-1.73	-1.73	5.68
	-1.11	1.88	1.88	-1.11	
	2.40	2.40	2.40	2.40	
X = 2.4	-7.82	-7.82	-0.37	-0.37	18.90
	-0.94	1.59	1.59	-0.94	

those planes while pickup ion signatures were observed. The planes used for the calculations are shown in Figure 6.10.

The location of the corners as well as the areas of each plane are shown in Table 6.2. The area of the planes increases with distance from Titan. This is interpreted as a consequence of the ions being diffused outwards as they travel down the tail once picked up.

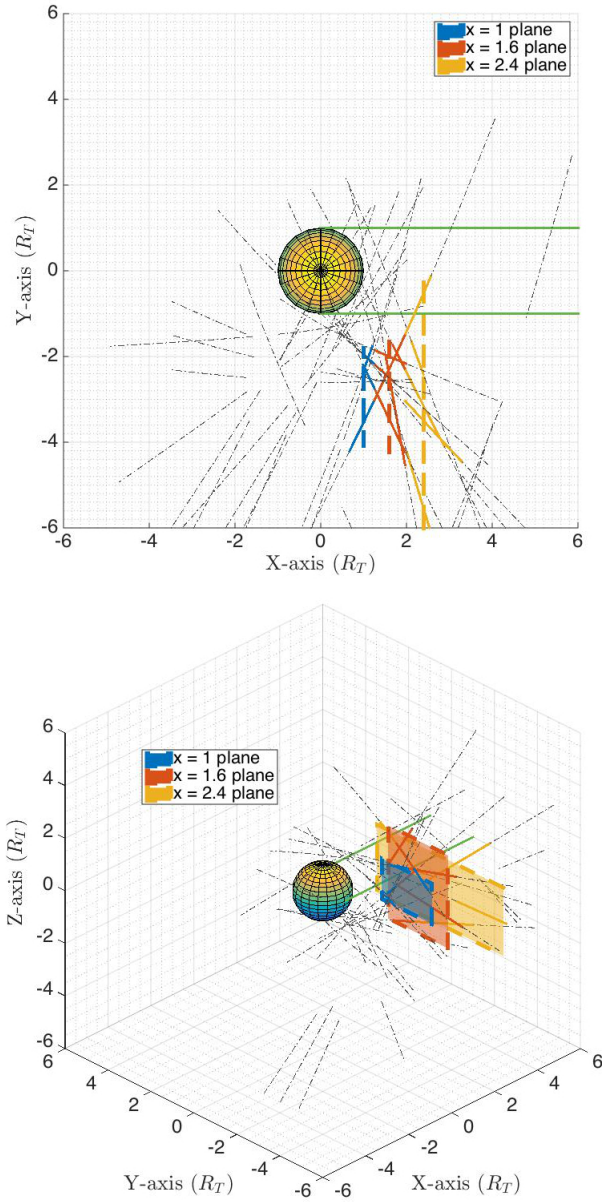

Figure 6.10: Location of planes used for estimation of freshly produced pickup ion escape rates. The top panel shows an equatorial view from the north pole of Titan and the bottom panel shows a 3-dimensional view. The black dashed lines show Cassini's trajectory for all the flybys. The colour lines show the flybys that contribute to the estimation of the escape rates with each colour matching that of the corresponding plane to which they contribute.

For the calculation, the differential energy flux (DEF; an explanation of the different scientific units and their relationship the the counts detected by the instruments is provided in Appendix D) values obtained by CAPS/IMS at the moment of the detection was used and the fluxes were obtained using Equation 6.3, where α is

Table 6.3: Median and deviations from differential energy flux (DEF) measurements (in $m^{-2} \cdot sr^{-1} \cdot s^{-1}$) and particle fluxes (in $ions \cdot s^{-1}$).

Plane	DEF	Particle flux
X = 1	$8.6 \pm 0.2 \times 10^{10}$	$8.3 \pm 0.2 \times 10^{22}$
X = 1.6	$1.5 \pm 0.03 \times 10^{11}$	$2.4 \pm 0.04 \times 10^{23}$
X = 2.4	$8.3 \pm 0.2 \times 10^{10}$	$4.2 \pm 0.1 \times 10^{23}$

the solid angle determined by the width of the distribution and A is the corresponding area of the planes (6.2) shown in Figure 6.10.

$$F = DEF \cdot \alpha \cdot A \tag{6.3}$$

The solid angle used for the integration was estimated from the angular distribution plots for the moment of detection shown in Figure 6.5. From the figure, an elevation angle of approximately 40° and an azimuth angle of approximately 20° are obtained, giving a total solid angle of 0.24 sr.

This way, an estimate of the fluxes through each plane was obtained. These fluxes are summarised in Table 6.3.

For the planes to be a good representation of the area where pickup ions escape towards the magnetosphere, the fluxes at each of the planes have to be similar. From Table 6.3 it can be seen that, even though some variations are present, these are relatively small, with the largest difference being a factor of 3.4 between the largest plane (X = 2.4) and the smallest one (X = 1). This is a consequence of the low number of data points for each plane (between 3 and 4).

By taking the mean of the three estimated values for the escaping fluxes, an estimate of $3.3^{+3}_{-2} \times 10^{23}$ $ions \cdot s^{-1}$ is obtained. If the population is assumed to be composed entirely of $m/q = 16$ ions, an ionospheric loss of ~ 570 kg/day is obtained while if it assumed to be composed entirely of $m/q = 28$ ions, the loss rate can be of up to 1 ton/day. This, although significant, is small compared to the 7 $tonnes/day$ obtained taking into account $m/q = 1$, 2 and 16 as measured during the distant tail flybys in Coates et al. (2012). This shows that the contribution of other ion escape processes is dominant.

These results can be compared to numbers published for neutral atmospheric escape to have an idea of the overall contribution of ionospheric escape to the total mass loss of Titan's atmosphere to the surrounding space. Taking the numbers given at the beginning of this chapter for H, H_2, N_2 and CH_4, the total mass loss through neutral escape is of the order of 5000 $tonnes/day$, making the contribution through ionised particles negligible. This mass loss, however large at about 50 kg/s, is small when compared to other Solar System objects such as Io (~ 1 $tonne/s$, Thomas et al. 2004) and Enceladus (> 150 kg/s, Hansen et al. 2006).

However, the outflow of ions can be detected directly by the instruments onboard Cassini, while the outflow of neutrals needs a combination of instrumentation and chemical modeling that makes it much more difficult to constrain the values. Additionally, since ions are affected by local electromagnetic fields, knowing the electromagnetic configuration at the time of a detection, together with the velocity and direction of a given ion population, these ions also serve as tracers that allow for the identification of the source where they were originated.

Due to the extremely dynamic nature of the magnetospheric environment surrounding Titan, the atmospheric and ionospheric escape processes taking place there are of a larger complexity than at any other Solar System body. In order to properly understand the dynamics of the ion escape, the source and ionisation processes that originated each ion population needs to be identified.

The results reported on this chapter contribute to this aim by identifying the contribution of a specific ionisation process, namely pickup ion. While the identification of pickup ions of lower masses is still unresolved, the escape through heavy pickup ions was shown to contribute about 10% of the overall ion escape.

A full understanding of all the processes involved can ultimately help modelling efforts directed towards the understanding of atmospheric evolution. In addition, in order to solve some of the open problems that still remain, such as the methane unbalance between loss and production (Strobel and Cui 2014) or the apparent absence of the predicted nitrogen torus at Titan's orbit (Smith et al. 2004, Smith et al. 2007), a detailed knowledge of the geometry of the escape region sur-

rounding Titan as well as the dynamics of the neutrals and charged particles leaving the moon is necessary.

Chapter 7

General conclusions

A combination of observations and simulations was used to study some aspects of the complex magnetospheric environment at Titan's orbit as well as the interaction of the moon with the Saturnian magnetosphere. These aspects include how the Saturnian magnetosphere affects the atmosphere of the moon but also how the presence of the moon affects the electromagnetic fields and the thermal and energetic plasma environment in its vicinity.

The availability of a dataset covering a wide energy spectrum proved to be an invaluable tool, not only for the objectives of the present work, but to contribute to the overall understanding and characterisation of the complex interaction that takes place between the only moon in the solar system with a thick atmosphere and the highly dynamic environment present in the outer magnetosphere of Saturn.

In addition, combining that dataset with test particle simulations helped to cover the gaps inevitably left by the temporally and spatially constrained coverage provided by Cassini.

In Chapter 4, the energetic plasma environment at Titan's orbit was studied using data from the MIMI/LEMMS instrument. While the magnetospheric regions have been categorised using thermal plasma (Rymer et al. 2009, Smith and Rymer 2014) and magnetic field (Simon et al. 2010, Simon et al. 2013) data, the energetic plasma is mostly unaffected by the location within the magnetosphere where the data is obtained from.

For the study, ion data with energies from 27 keV to 4 MeV and electron data

with energies from 18 to 832 keV for all the dedicated flybys and orbit crossings (without Titan being there) from October 2004 to December 2015 were used. This comprises 114 Titan flybys and 189 orbit crossings, for a total of 303 measurement periods. For each period, average fluxes were calculated and a modified Kappa distribution function (Dialynas et al. 2009) was fitted.

A previous noon-midnight asymmetry reported in Garnier et al. (2010) relating ion average fluxes with Saturn local time was observed as well when using the extended data set presented in this thesis. The asymmetry was also observed in the dusk-dawn direction with higher fluxes on the noon-to-dusk sector and lower fluxes on the midnight-to-dawn sector. Further investigation needs to be done to find the origin of this asymmetry, that could be linked to either transport processes such as Dungey or Vasyliūnas cycles or by the presence of electric fields such as the noon-to-midnight reported in Andriopoulou et al. (2012).

Additionally, some dependence on the location within the magnetosphere (plasma sheet, lobes) or outside in the magnetosheath or solar wind was encountered for the ions. This dependence, however, is a weak one with important overlaps, making it possible to measure similar fluxes during flybys that occur at completely different locations.

For the case of electrons, no dependence was found whatsoever, something that is here interpreted as a consequence of their high mobility that allows them to travel along the field lines to higher latitudes. The variabilities observed might have an origin that is not related to the magnetic latitude at which Titan is found at any given time. They could be related instead to some non-local factor such as solar wind activity or acceleration or transport processes within the magnetosphere.

For both cases, the difficulty to classify the environment based on the observed fluxes is a consequence of the high kinetic energy and the non-isotropic distribution of the particles. At the energies studied in this thesis, the ions and electrons have a non-negligible velocity component along the magnetic field allowing them to travel far from the equator. This means that the particles will no longer be confined to the plasma sheet and thus a clear distinction between plasma sheet and lobes is not

present anymore.

The high variability encountered means that when studying the interaction of Titan with the Saturnian magnetosphere from the point of view of energetic particles, the analyses need to be made on a case-by-case basis.

In Chapter 5, the energy deposition by energetic ions was studied. Special emphasis was put on how the draped magnetic field lines that form the induced magnetosphere around Titan guide charged particles with different characteristics in a different way, causing them to deposit their energy at different locations around the moon.

The simulations were run using a test particle tracer and a 3-dimensional description of the electromagnetic fields provided by a hybrid code. As a test case, an equatorial flyby (T9) was used. During this flyby, important asymmetries in the magnetic field signature were observed, with large deviations from the nominal north-south configuration that can be expected in the inner regions of the magnetosphere.

By tracing H^+ and O^+ ions with energies from 1 keV to 1 MeV, it was shown that particles with energy different that are coming from different locations in the magnetosphere are able to access the moon's exobase at completely different locations, giving rise to considerable asymmetries in the energy deposition and, consequently, in the ionisation rates.

For the specific case studied, differences in ionisation rates by O^+ of about 15% and by $H^+$of almost 80% were estimated. From these results, it is possible to foresee that the specific configuration of the electromagnetic field around the moon at any given time will have an effect on the local ionospheric densities. This effect is large enough to be considered when studying the contribution of energetic ions to the ion production in Titan's atmosphere.

While the precipitation of energetic ions can trigger ionisation of atmospheric particles by charge exchange, the photoionisation by solar EUV radiation is by far the dominant process in the creation of the ionosphere (Cravens et al. 2009), so the impact of the results might be more relevant when looking at the nightside iono-

spheric densities. However, even on the nightside, the significance of the results will depend on another factor that has been pointed out as dominant over charge exchange, namely electron impact ionisation from energetic electrons (Sittler et al. 2009).

In Chapter 6, the production of pickup ions at Titan was investigated. Once ions are produced and picked up by the local electric fields, they form a population with a ring distribution in velocity space. This distribution is unstable and when scattering in the pitch angle distribution occurs, ion cyclotron waves are generated.

At Titan, however, these waves are usually absent and, for this reason, another mechanism is needed to study the ions. In this thesis, thermal ion data provided by the CAPS/IMS instrument were used to detect them and to characterise the region around the moon where these ions are present.

By looking at ion data with energies lower than 50 keV for all the available flybys, a survey of signatures left by these ions was performed and the region where the freshly produced pickup ions can be detected was constrained. This region is mainly located on the anti-Saturn side, something that was already expected due to the nominal direction of the corotation electric field. However, a tighter constraint was obtained by looking at the spatial distribution of the detected ions downstream of the moon. This constraint led to the definition of three different planes along the corotation direction that were used to estimate escape rates by freshly produced heavy pickup ions with $m/q \sim 16$ to $m/q \sim 28$.

The estimated fluxes are a small fraction of the total ion and neutral escape estimated by other authors (e.g. Coates et al. 2012, Strobel and Cui 2014) when analysing data obtained during distant tail flybys. However, estimating the contribution of individual escape processes opens the door to a better understanding of the loss mechanisms that take place at the moon.

Chapter 8

Future work

The results obtained during the development of this thesis opened new questions that need to be addressed in future works. These questions can be individually linked specifically to each of the topics studied but also to a combination of them.

In terms of the energetic environment, a continuation of the analysis presented in this thesis might enable to find an empirical model of the ion fluxes encountered at Titan's orbit. This could be made, for instance, by correlating different factors such as the fitting parameters from the modified Kappa distribution used in the study.

For the case of electrons, the complete lack of correlation with any of the factors studied seems to imply that the variabilities have a different origin and the determination of this origin is still an open question. The use of the extended data set made it possible to rule out any obvious seasonal effect, so further studies need to focus on other aspects, probably not limiting the analysis to the vicinity of Titan's orbit but also looking for correlations with other magnetospheric phenomena such as injection events or morphological changes in the overall structure of the magnetosphere due to solar activity.

While the effect that the draping of the field lines has on the precipitation of energetic ions was studied, the effect on energetic electrons remains unknown. Since the ionisation by precipitating energetic electrons has been shown to be more important than that of energetic ions, the effect of the draped field lines in the local ionisation could be more important than what was stated in this study. However, how important it is remains an open question. While electrons follow more closely

the field lines and thus the effect could be expected to be more prominent, they are also more affected by the shielding that arises from the pile-up of magnetic field lines around the moon.

Additionally, for the simulations presented in Chapter 5, another important factor that needs to be studied, the incidence angle of the ions, was not taken into account. The inclusion of the incidence angle will also have an impact in the results, leaving the ones presented here as an upper limit for the ionisation rates. This, however, affects both the regions with minimum and maximum ionisation rates and because of this, even though the overall rates will be affected, the relative ones between different positions should remain relatively unchanged.

Regarding the atmospheric and ionospheric losses, while the analysis of pickup ion losses presented here is a first step in the determination of the contribution of individual loss mechanisms, different methods need to be assessed to study other processes individually. This even applies to pickup ions with lower masses or detected farther from the moon, where the initial ring distribution has been scattered.

Also, while the absence of ion cyclotron waves was explained by the short convection times of the flux tubes when passing Titan, the fact that they were indeed observed during two flybys (T63 and T98) still requires an explanation. A detailed analysis of the locations where ions originated at Titan are first observed in all directions together with specific magnetic field configurations probably obtained with the help of simulations could shed some light on what was special about those two specific flybys.

Finally, from a more general point of view, a combination of the simulation and data analysis methods applied in the three research chapters of this thesis would make it possible to study Titan's interaction region from a global perspective.

By combining the energetic ion and electron fluxes obtained with those typical for thermal plasma at the different possible environments, upstream conditions for different simulation scenarios could be defined. These upstream fluxes could then be used in combination with the tracing of charged particles in the vicinity of the moon to predict the energy deposition rates and, at the same time, the production of

pickup ions to estimate ionisation and escape rates under different conditions.

All of this together could provide some of the building blocks of an empirical model covering all the different aspects of the interaction, from the energetic ion and electron fluxes to the corresponding energy deposition, ionisation rates and atmospheric losses. Such a model could make significant contributions to the overall understanding of how moons interact with their parent magnetospheres throughout the Solar System.

Appendix A

Validation of particle tracing code

Before using the tracing code described in Chapter 3 for any research purpose, a validation had to be carried out in order to ensure that the results obtained from it were accurate.

As described throughout this thesis, Titan's magnetospheric environment is extremely complex. This complexity makes it impossible to predict how a charged particle will behave once it interacts with the electromagnetic field perturbations that arise from the draping of the field lines close to the moon.

Basic validations under completely predictable scenarios were initially performed. These include the comparison of the analytically calculated mirror points and the location of the simulated ones as well as the bouncing motion of a particle in a dipolar field configuration or the simulation of a forward and backward trajectory verifying that the initial and final positions are the same.

However, a more complex scenario such as the interaction with many particles with an obstacle such as a moon requires the preparation of a scenario with known results, at least to a qualitative degree. In this appendix, the results from a validation run using a simple uniform north-south magnetic field configuration are presented.

Even though the magnetic field configuration is completely different from the one provided by the hybrid code output that is used for the results presented in Chapter 5, parameters such as the energy and species of the particles simulated need to be similar in order to ensure that no numerical errors are introduced when using the hybrid code. These errors could arise, for instance, from using a grid for

which the spatial separation between two adjacent cells is larger than the gyroradius of the particle being traced.

The particles used for this run were 1 keV electrons with 90°() pitch angle ($V_{||} = 0$) which, for a background field of 5 nT have a gyroradius of approximately 22 km, or 0.0083 Titan radii (R_T). Even though this is smaller than the spatial resolution of the hybrid code output (0.05 R_T), since the field description used here is uniform, no numerical errors are expected.

Apart from the simple field description mentioned above, a corotation electric field is implemented. This is expected to move the particles along the corotation direction thus creating an asymmetry in the access of the electrons to the moon.

Figure A.1 shows the result of the validation run in the form of a 2D projection of Titan's exobase showing the percentage of simulated particles that are able to escape the moon's vicinity during a backward tracing. This is equivalent to the percentage of particles that would be able to reach a given location around the moon during a forward tracing. This is the same type of map as presented in Chapter 5.

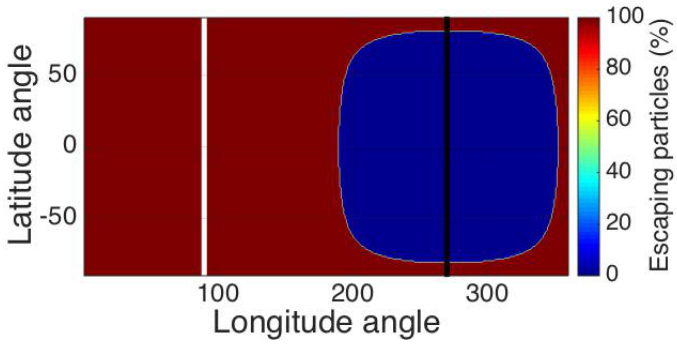

Figure A.1: Equirectangular projection of Titan's exobase showing the percentage of 1 keV electrons that are able to escape the moon's vicinity during a backward tracing under a uniform background magnetic field. The white vertical line indicates the position of the ram direction while the black vertical line indicates the position of the tail.

The map shows a clear depletion of particles around the tail of the moon. This is the expected result given the small gyroradius of the simulated particles which causes them to impact the moon as they are transported in the corotation direction by the convecting magnetic field lines.

Appendix B

Effect of changing the exobase altitude on the access of energetic particles

In Chapter 5, while studying how the access of energetic particles to Titan's exobase is affected by the electromagnetic field configuration around Titan, the exobase altitude was set at 1450 km. This is the altitude suggested by some authors (e.g. Yelle et al. 2014), but some other altitudes have been used in other studies as well (e.g. Ledvina et al. 2012, Johnson et al. 2009, Strobel 2009).

In this appendix, the effect on the results of moving the exobase towards higher altitudes is investigated. For this, one of the results presented in Chapter 5, specifically the backtracing of 1 keV O^+ ions is repeated while setting the exobase altitude at 1500 km, 1550 km and 1600 km and the results are compared with the original setting of 1450 km.

Figure B.1 shows the equirectangular projections representing the access of ions to the exobase at the four mentioned altitudes.

From a visual inspection of the four maps, no significant differences are present on a global scale. Given that the colour scale is the same for the four cases, it can be seen that quantitatively the percentage of particles that would reach the moon at a given position does not change in an appreciable manner by changing the exobase altitude by up to 150 km.

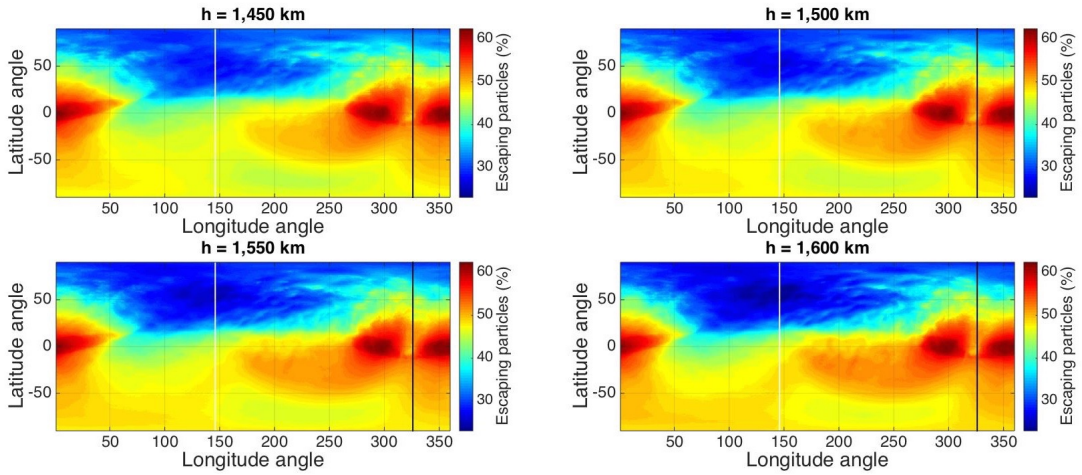

Figure B.1: Percentage of particles that are able to escape the vicinity of the moon by setting the exobase at four different altitudes: 1450 km (top left), 1500 km (top right), 1550 km (bottom left) and 1600 km (bottom right).

There are some changes in small scale structures, for instance in the northern region surrounding the ram direction (white line), where the access seems to decrease with increasing altitude, or in the southern region between 200° and 250° longitude, where the access increases. This might be a consequence of the local magnitude of the magnetic field changing with increasing altitude but the effect is small enough, leading to the conclusion that the choice of 1450 km for the exobase altitude is an appropriate one.

Appendix C

Flyby and orbit crossing times

In Chapter 4, the energetic plasma environment at Titan's orbit was analysed. For this, ion and electron data gathered by the MIMI/LEMMS instrument between the 26th. of October 2004 and the end of 2015 were considered. The following table presents the dates at which each flyby and each pass occurred.

Flyby	Date	Pass	Date
TA	2004-300T15:30:00.000	P1	2005-014T12:15:00.000
TB	2004-348T11:38:00.000	P2	2005-049T19:05:00.000
T3	2005-046T06:54:00.000	P3	2005-066T17:30:00.000
T4	2005-090T20:05:16.000	P4	2005-070T05:50:00.000
T5	2005-106T19:11:46.000	P5	2005-087T05:30:00.000
T6	2005-234T08:53:37.000	P6	2005-124T21:00:00.000
T7	2005-250T08:11:57.000	P7	2005-143T01:20:00.000
T8	2005-301T04:15:00.000	P8	2005-161T05:55:00.000
T9	2005-360T18:59:30.000	P9	2005-179T11:00:00.000
T10	2006-015T11:41:27.000	P10	2005-197T17:30:00.000
T11	2006-058T08:25:00.000	P11	2005-216T01:05:00.000
T12	2006-078T00:05:57.000	P12	2005-265T03:55:00.000
T13	2006-120T20:54:00.000	P13	2005-268T15:20:00.000
T14	2006-140T12:18:12.000	P14	2005-283T07:50:00.000
T15	2006-183T09:12:00.000	P15	2005-286T19:20:00.000
T16	2006-203T00:25:00.000	P16	2005-304T17:25:00.000

T17	2006-250T20:16:00.000	P17	2005-329T16:45:00.000
T18	2006-266T18:59:00.000	P18	2005-333T06:05:00.000
T19	2006-282T17:23:00.000	P19	2005-357T02:40:00.000
T20	2006-298T15:58:00.000	P20	2006-019T01:50:00.000
T21	2006-346T11:41:00.000	P21	2006-054T16:05:00.000
T22	2006-362T10:05:00.000	P22	2006-081T14:45:00.000
T23	2007-013T08:34:00.000	P23	2006-117T05:20:00.000
T24	2007-029T07:16:00.000	P24	2006-144T03:35:00.000
T25	2007-053T03:11:00.000	P25	2006-179T18:30:00.000
T26	2007-069T01:47:00.000	P26	2006-227T02:10:00.000
T27	2007-085T00:22:00.000	P27	2006-310T19:30:00.000
T28	2007-100T22:58:00.000	P28	2006-322T18:30:00.000
T29	2007-116T21:33:00.000	P29	2006-334T17:05:00.000
T30	2007-132T20:08:00.000	P30	2007-035T04:30:00.000
T31	2007-148T18:51:00.000	P31	2007-047T13:20:00.000
T32	2007-164T17:46:00.000	P32	2007-177T07:40:00.000
T33	2007-180T17:03:00.000	P33	2007-203T14:55:00.000
T34	2007-200T01:04:00.000	P34	2007-239T18:40:00.000
T35	2007-243T06:35:00.000	P35	2007-299T01:45:00.000
T36	2007-275T04:44:00.000	P36	2008-017T21:55:00.000
T37	2007-323T00:47:00.000	P37	2008-029T20:05:00.000
T38	2007-339T00:07:00.000	P38	2008-041T18:40:00.000
T39	2007-354T22:58:00.000	P39	2008-064T08:30:00.000
T40	2008-005T21:30:00.000	P40	2008-075T00:30:00.000
T41	2008-053T17:32:00.000	P41	2008-095T05:35:00.000
T42	2008-085T14:28:00.000	P42	2008-104T19:40:00.000
T43	2008-133T10:02:00.000	P43	2008-114T09:05:00.000
T44	2008-149T08:25:00.000	P44	2008-123T22:15:00.000
T45	2008-213T02:13:00.000	P45	2008-141T11:00:00.000
T46	2008-308T17:35:00.000	P46	2008-156T13:55:00.000
T47	2008-324T15:56:00.000	P47	2008-163T17:15:00.000

T48	2008-340T14:26:00.000	P48	2008-170T20:15:00.000
T49	2008-356T13:00:00.000	P49	2008-178T00:45:00.000
T50	2009-038T08:51:00.000	P50	2008-185T01:35:00.000
T51	2009-086T04:44:00.000	P51	2008-192T02:25:00.000
T52	2009-094T01:48:00.000	P52	2008-199T03:10:00.000
T53	2009-110T00:21:00.000	P53	2008-206T04:05:00.000
T54	2009-125T22:54:00.000	P54	2008-220T15:55:00.000
T55	2009-141T21:27:00.000	P55	2008-228T01:35:00.000
T56	2009-157T20:00:00.000	P56	2008-235T10:05:00.000
T57	2009-173T18:33:00.000	P57	2008-242T19:10:00.000
T58	2009-189T17:04:00.000	P58	2008-250T04:00:00.000
T59	2009-205T15:34:00.000	P59	2008-257T12:55:00.000
T60	2009-221T14:04:00.000	P60	2008-264T21:45:00.000
T61	2009-237T12:52:00.000	P61	2008-272T06:35:00.000
T62	2009-285T08:36:00.000	P62	2008-279T16:20:00.000
T63	2009-346T01:03:00.000	P63	2008-287T01:10:00.000
T64	2009-362T00:17:00.000	P64	2008-294T09:05:00.000
T65	2010-012T23:11:00.000	P65	2008-301T16:20:00.000
T66	2010-028T22:29:00.000	P66	2008-316T18:25:00.000
T67	2010-095T15:51:00.000	P67	2008-332T19:30:00.000
T68	2010-140T03:24:00.000	P68	2008-348T17:20:00.000
T69	2010-156T02:26:00.000	P69	2008-366T00:00:00.000
T70	2010-172T01:27:00.000	P70	2009-009T13:45:00.000
T71	2010-188T00:26:00.000	P71	2009-019T03:20:00.000
T72	2010-267T18:45:00.000	P72	2009-028T16:35:00.000
T73	2010-315T13:45:00.000	P73	2009-050T11:25:00.000
T74	2011-049T16:04:00.000	P74	2009-062T10:10:00.000
T75	2011-109T05:10:00.000	P75	2009-074T09:30:00.000
T76	2011-128T22:52:00.000	P76	2009-101T12:05:00.000
T77	2011-171T18:40:00.000	P77	2009-261T14:55:00.000
T78	2011-255T02:49:00.000	P78	2009-288T23:05:00.000

T79	2011-347T20:07:00.000	P79	2009-304T10:45:00.000
T80	2012-002T14:51:00.000	P80	2009-307T22:35:00.000
T81	2012-030T13:30:00.000	P81	2009-323T11:20:00.000
T82	2012-050T08:16:00.000	P82	2009-326T23:10:00.000
T83	2012-143T00:54:00.000	P83	2009-342T12:10:00.000
T84	2012-159T00:07:21.000	P84	2010-042T23:10:00.000
T85	2012-206T20:03:08.000	P85	2010-046T10:40:00.000
T86	2012-270T14:35:39.000	P86	2010-060T12:20:00.000
T87	2012-318T10:22:10.000	P87	2010-063T23:45:00.000
T88	2012-334T08:57:00.000	P88	2010-078T03:35:00.000
T89	2013-048T01:56:37.000	P89	2010-081T15:00:00.000
T90	2013-095T21:43:32.000	P90	2010-099T07:10:00.000
T91	2013-143T17:32:55.000	P91	2010-116T03:25:00.000
T92	2013-191T13:21:48.000	P92	2010-119T15:55:00.000
T93	2013-207T11:56:23.000	P93	2010-136T14:20:00.000
T94	2013-255T07:43:57.000	P94	2010-168T13:20:00.000
T95	2013-287T04:56:28.000	P95	2010-207T21:25:00.000
T96	2013-335T00:41:19.000	P96	2010-227T19:15:00.000
T97	2014-001T21:59:42.000	P97	2010-247T19:55:00.000
T98	2014-033T19:12:39.000	P98	2010-291T12:30:00.000
T99	2014-065T16:26:48.000	P99	2010-332T15:15:00.000
T100	2014-097T13:41:15.000	P100	2010-336T03:50:00.000
T101	2014-137T16:12:16.000	P101	2010-353T04:30:00.000
T102	2014-169T13:28:25.000	P102	2010-356T17:05:00.000
T103	2014-201T10:40:59.000	P103	2011-008T22:00:00.000
T104	2014-233T08:09:10.000	P104	2011-012T10:30:00.000
T105	2014-265T05:23:20.000	P105	2011-029T08:30:00.000
T106	2014-297T02:40:31.000	P106	2011-032T21:10:00.000
T107	2014-344T22:26:36.000	P107	2011-053T08:40:00.000
T108	2015-011T19:48:36.000	P108	2011-077T16:50:00.000
T109	2015-043T17:08:05.000	P109	2011-081T06:40:00.000

T110	2015-075T14:29:49.000	P110	2011-105T14:50:00.000
T111	2015-127T22:50:25.000	P111	2011-132T16:05:00.000
T112	2015-188T08:09:51.000	P112	2011-168T04:25:00.000
T113	2015-271T21:27:14.000	P113	2011-189T20:55:00.000
T114	2015-317T05:46:35.000	P114	2011-193T11:05:00.000
		P115	2011-211T13:05:00.000
		P116	2011-215T03:15:00.000
		P117	2011-233T08:55:00.000
		P118	2011-236T23:00:00.000
		P119	2011-258T17:35:00.000
		P120	2011-272T22:20:00.000
		P121	2011-276T11:25:00.000
		P122	2011-290T17:50:00.000
		P123	2011-294T07:00:00.000
		P124	2011-308T13:25:00.000
		P125	2011-312T02:35:00.000
		P126	2011-326T09:55:00.000
		P127	2011-329T23:05:00.000
		P128	2011-344T07:30:00.000
		P129	2012-006T08:15:00.000
		P130	2012-026T23:15:00.000
		P131	2012-053T23:50:00.000
		P132	2012-068T07:45:00.000
		P133	2012-071T20:45:00.000
		P134	2012-086T02:55:00.000
		P135	2012-089T16:05:00.000
		P136	2012-103T22:30:00.000
		P137	2012-107T11:35:00.000
		P138	2012-121T18:00:00.000
		P139	2012-125T07:05:00.000
		P140	2012-139T11:55:00.000

		P141	2012-182T21:15:00.000
		P142	2012-228T00:50:00.000
		P143	2012-249T07:00:00.000
		P144	2012-294T11:35:00.000
		P145	2012-347T14:50:00.000
		P146	2012-360T21:00:00.000
		P147	2013-008T03:40:00.000
		P148	2013-021T10:50:00.000
		P149	2013-034T18:00:00.000
		P150	2013-059T23:45:00.000
		P151	2013-071T23:00:00.000
		P152	2013-083T22:05:00.000
		P153	2013-105T10:20:00.000
		P154	2013-115T00:00:00.000
		P155	2013-124T13:40:00.000
		P156	2013-134T03:15:00.000
		P157	2013-155T15:35:00.000
		P158	2013-167T14:35:00.000
		P159	2013-179T13:45:00.000
		P160	2013-231T08:10:00.000
		P161	2014-101T18:15:00.000
		P162	2014-133T09:20:00.000
		P163	2015-099T20:25:00.000
		P164	2015-103T13:50:00.000
		P165	2015-131T14:30:00.000
		P166	2015-146T18:30:00.000
		P167	2015-150T11:20:00.000
		P168	2015-165T16:20:00.000
		P169	2015-169T09:10:00.000
		P170	2015-184T14:50:00.000
		P171	2015-206T09:10:00.000

		P172	2015-210T02:30:00.000
		P173	2015-228T04:45:00.000
		P174	2015-231T22:00:00.000
		P175	2015-250T01:05:00.000
		P176	2015-253T18:20:00.000
		P177	2015-275T12:15:00.000
		P178	2015-285T18:10:00.000
		P179	2015-289T10:05:00.000
		P180	2015-299T15:55:00.000
		P181	2015-303T07:55:00.000
		P182	2015-313T13:30:00.000
		P183	2015-326T07:25:00.000
		P184	2015-329T23:05:00.000
		P185	2015-339T00:45:00.000
		P186	2015-342T16:20:00.000
		P187	2015-351T18:20:00.000
		P188	2015-355T10:00:00.000
		P189	2015-364T14:50:00.000

Appendix D

Scientific units from plasma instruments

Plasma instruments like CAPS and MIMI are based on the principle of counting incoming charged particles in a similar way as charge-coupled devices (CCDs) count photons, even though the working principle for both types of instruments is completely different.

The raw measure from an instrument is counts per accumulation. This is simply the number of particles detected during a certain pre-defined accumulation time. There are different scientific units of interested when studying a plasma and the conversion is somewhat sequential.

Counts per second

The simplest derived unit is the number of counts per second. The relationship between counts per accumulation and counts per second is the integration time (dt) of the instrument (Equation D.1).

$$C_s = \frac{C_{Accum.}}{dt} \tag{D.1}$$

Differential energy flux (DEF)

A more meaningful scientific unit to measure the particle fluxes is the DEF, measured in . It is defined as the counts per second divided by a scale factor that accounts for the MCP gain and the geometric factor (G) of the instrument (Equation

D.2), giving a flux that is dependent on the energy of the particle.

$$DEF = \frac{C_s}{G} \tag{D.2}$$

Differential number flux (DNF)

To get rid of that dependence on the energy, the DEF is divided by the energy of the particle being measured (Equation D.3).

$$DNF = \frac{DEF}{E} \tag{D.3}$$

Phase space density

Finally, to obtain the phase space density (in units of $m^{-6}s^{-3}$), the DNF value is divided by v^4. The velocity v is taken from the kinetic energy ($E = 0.5 \cdot m \cdot v^2$). This is shown in Equation D.4.

$$PSD = \frac{DEF}{v^4} = \frac{DEF \cdot m^2}{4E^2} \tag{D.4}$$

Appendix E

List of acronyms

A.I.K.E.F.	Adaptive Ion-Kinetic Electron-Fluid
CA	Closest approach
CAPS	Cassini Plasma Spectrometer
CHEMS	Charge-Energy-Mass Spectrometer
DEF	Differential Energy Flux
DSMC	Direct Simulation Monte Carlo
ELS	Electron Spectrometer
ENA	Energetic Neutral Atom
ESA	Electrostatic Analyser
EUV	Extreme ultraviolet
FGM	Flux-Gate Magnetometer
IBS	Ion Beam Spectrometer
ICW	Ion Cyclotron Wave
IMF	Interplanetary Magnetic Field
IMS	Ion Mass Spectrometer
INCA	Ion and Neutral Camera
INMS	Ion and Neutral Mass Spectrometer
JPL	Jet Propulsion Laboratory
LEMMS	Low Energy Magnetospheric Measurements System
MAG	Magnetometer
MCP	Microchannel Plate

MHD	Magnetohydrodynamics
$MIMI$	Magnetospheric Imaging Instrument
MPS	Max Planck Institute for Solar System Research
$MSSL$	Mullard Space Science Laboratory
$NASA$	National Aeronautics and Space Administration
PIC	Particle-in-cell
R_S	Saturn's radius (60268 km)
R_T	Titan's radius (2576 km)
S/VHM	Scalar/Vector Helium Magnetometer
SLT	Saturn Local Time
$SRIM$	Stopping and Range of Ions in Matter
SZA	Solar zenith angle
$TIIS$	Titan Interaction System
TOF	Time-of-flight

Bibliography

H. Alfvén. On the theory of comet tails. *Tellus*, 9, 1957.

N. André, M. Blanc, S. Maurice, P. Schippers, E. Pallier, T. I. Gombosi, K. C. Hansen, D. T. Young, F. J. Crary, S. Bolton, E. C. Sittler, H. T. Smith, R. E. Johnson, R. A. Baragiola, A. J. Coates, A. M. Rymer, M. K. Dougherty, N. Achilleos, C. S. Arridge, S. M. Krimigis, D. G. Mitchell, N. Krupp, D. C. Hamilton, I. Dandouras, D. A. Gurnett, W. S. Kurth, P. Louarn, R. Srama, S. Kempf, H. J. Waite, L. W. Esposito, and J. T. Clarke. Identification of Saturn's magnetospheric regions and associated plasma processes: Synopsis of Cassini observations during orbit insertion. *Review of Geophysics*, 46(4), December 2008. doi: 10.1029/2007RG000238.

M. Andriopoulou, E. Roussos, N. Krupp, C. Paranicas, M. Thomsen, S. Krimigis, M. K. Dougherty, and K.-H. Glassmeier. A noon-to-midnight electric field and nightside dynamics in Saturn's inner magnetosphere, using microsignature observations. *Icarus*, 220(2):503–513, August 2012. doi: 10.1016/j.icarus.2012.05.010.

C. S. Arridge, K. K. Khurana, C. T. Russell, D. J. Southwood, N. Achilleos, M. K. Dougherty, A. J. Coates, and H. K. Leinweber. Warping of Saturn's magnetospheric and magnetotail current sheets. *Journal of Geophysical Research*, 2008.

C. S. Arridge, N. André, C. L. Bertucci, P. Garnier, C. M. Jackman, Z. Németh, A. M. Rymer, N. Sergis, K. Szego, A. J. Coates, and F. J. Crary. Upstream of Saturn and Titan. *Space Science Reviews*, 162:25–83, 2011a.

C. S. Arridge, N. André, H. J. McAndrews, E. J. Bunce, M. H. Burger, K. C. Hansen, H.-W. Hsu, R. E. Johnson, G. H. Jones, S. Kempf, K. K. Khurana, N. Krupp, W. S. Kurth, J. S. Leisner, C. Paranicas, E. Roussos, C. T. Russell, P. Schippers, E. C. Sittler, H. T. Smith, M. F. Thomsen, and M. K. Dougherty. Mapping Magnetospheric Equatorial Regions at Saturn from Cassini Prime Mission Observations. *Space Science Reviews*, 164(1):1–83, December 2011b. doi: 10.1007/s11214-011-9850-4.

H. Backes. *Titan's interaction with the Saturnian magnetospheric plasma*. PhD thesis, Universität zu Köln, 2005.

H. Backes, F. M. Neubauer, M. K. Dougherty, N. Achilleos, N. André, C. S. Arridge, C. Bertucci, G. H. Jones, K. K. Khurana, C. T. Russell, and A. Wennmacher. Titan's Magnetic Field Signature During the First Cassini Encounter. *Science*, 2005.

W. Baumjohann and R. A. Treumann. *Basic Space Plasma Physics*. Imperial College Press, 1997.

C. Bertucci, F. M. Neubauer, K. Szego, J.-E. Wahlund, A. J. Coates, M. K. Dougherty, D. T. Young, and W. S. Kurth. Structure of Titan's mid-range magnetic tail: Cassini magnetometer observations during the T9 flyby. *Geophysical Research Letters*, 2007.

C. Bertucci, N. Achilleos, M. K. Dougherty, R. Modolo, A. J. Coates, K. Szego, A. Masters, Y. Ma, F. M. Neubauer, P. Garnier, J.-E. Wahlund, and D. T. Young. The Magnetic Memory of Titan's Ionized Atmosphere. *Science*, 2008.

C. Bertucci, D. C. Hamilton, W. S. Kurth, G. Hospodarsky, D. Mitchell, N. Sergis, N. J. T. Edberg, and M. K. Dougherty. Titan's interaction with the supersonic solar wind. *Geophysical Research Letters*, 2015.

M. Blanc, S. Bolton, J. Bradley, M. Burton, T. E. Cravens, I. Dandouras, M. K. Dougherty, M. C. Festou, J. Feynman, R. E. Johnson, T. G. Gombosi, W. S.

Kurth, P. C. Liewer, B. H. Mauk, S. Maurice, D. Mitchell, F. M. Neubauer, J. D. Richardson, D. E. Shemansky, E. C. Sittler, B. T. Tsurutani, Ph. Zarka, L. W. Esposito, E. Grün, D. A. Gurnett, A. J. Kliore, S. M. Krimigis, D. Southwood, J. H. Waite, and D. T. Young. Magnetospheric and Plasma Science with Cassini-Huygens. *Space Science Reviews*, 104(1):253–346, July 2002. doi: 10.1023/A:1023605110711.

M. Blanc, D. J. Andrews, A. J. Coates, D. C. Hamilton, C. M. Jackman, X. Jia, A. Kotova, M. Morooka, H. T. Smith, and J. H. Westlake. Saturn Plasma Sources and Associated Transport Processes. *Space Science Reviews*, 192(1):237–283, October 2015. doi: 10.1007/s11214-015-0172-9.

A. Bößwetter, T. Bagdonat, U. Motschmann, and K. Sauer. Plasma boundaries at Mars: a 3-D simulation study. *Annales Geophysicae*, 22(12):4363–4379, December 2004. doi: 10.5194/angeo-22-4363-2004.

P. C. Brandt, K. Dialynas, I. Dandouras, D. G. Mitchell, P. Garnier, and S. M. Krimigis. The distribution of Titan's high-altitude (out to ∼50,000 km) exosphere from energetic neutral atom (ENA) measurements by Cassini/INCA. *Planetary and Space Science*, 60(1):107–114, January 2012. doi: 10.1016/j.pss.2011.04.014.

M. E. Burton, B. Buratti, D. L. Matson, and J.-P. Lebreton. The Cassini/Huygens Venus and Earth flybys: An overview of operations and results. *Journal of Geophysical Research*, 106(A12):30099–30107, December 2001. doi: 10.1029/2001JA900088.

M. E. Burton, M. K. Dougherty, and C. T. Russell. Saturn's internal planetary magnetic field. *Geophysical Research Letters*, 37(24), December 2010. doi: 10.1029/2010GL045148.

S. P. Christon, D. C. Hamilton, D. G. Mitchell, R. D. DiFabio, and S. M. Krimigis. Suprathermal magnetospheric minor ions heavier than water at Saturn: Discovery

of $^{28}M^{+}$ seasonal variations. *Journal of Geophysical Research*, 119(7):5662–5673, July 2014. doi: 10.1002/2014JA20010.

S. P. Christon, D. C. Hamilton, J. M. C. Plane, D. G. Mitchell, R. D. DiFabio, and S. M. Krimigis. Discovery of suprathermal Fe^{+} in Saturn's magnetosphere. *Journal of Geophysical Research*, 120(4):2720–2738, April 2015. doi: 10.1002/2014JA020906.

A. J. Coates. Interaction of Titan's ionosphere with Saturn's magnetosphere. *Philosophical Transactions of The Royal Society A*, 367(1889):773–788, February 2009. doi: 10.1098/rsta.2008.0248.

A. J. Coates and G. H. Jones. Plasma environment of Jupiter family comets. *Planetary and Space Science*, 57(10):1175–1191, August 2009. doi: 10.1016/j.pss.2009.04.009.

A. J. Coates, B. Wilken, A. D. Johnstone, K. Jockers, K.-H. Glassmeier, and D. E. Huddleston. Bulk Properties and Velocity Distributions of Water Group Ions at Comet Halley: Giotto Measurements. *Journal of Geophysical Research*, 95(A7):10249–10260, 1990. doi: 10.1029/JA095iA07p10249.

A. J. Coates, A. D. Johnstone, B. Wilken, and F. M. Neubauer. Velocity Space Diffusion and Nongyrotropy of Pickup Water Group Ions at Comet Grigg-Skjellerup. *Journal of Geophysical Research*, 98(A12):20985–20994, December 1993. doi: 10.1029/93JA02535.

A. J. Coates, F. J. Crary, G. R. Lewis, D. T. Young, J. H. Waite Jr., and E. C. Sittler Jr. Discovery of heavy negative ions in Titan's ionosphere. *Geophysical Research Letters*, 34(22), November 2007a. doi: 10.1029/2007GL030978.

A. J. Coates, F. J. Crary, D. T. Young, K. Szego, C. S. Arridge, Z. Bebesi, E. C. Sittler, R. E. Hartle, and T. W. Hill. Ionospheric electrons in Titan's tail: Plasma structure during the Cassini T9 encounter. *Geophysical Research Letters*, 2007b.

A. J. Coates, A. Wellbrock, G. R. Lewis, C. S. Arridge, F. J. Crary, D. T. Young, M. F. Thomsen, D. B. Reisenfeld, E. C. Sittler, R. E. Johnson, K. Szego, Z. Bebesi, and G. H. Jones. Cassini in Titan's tail: CAPS observations of plasma escape. *Journal of Geophysical Research*, 117, 2012. doi: 10.1029/2012JA017595.

J. E. P. Connerney, M. H. Acu na, and N. F. Ness. Currents in Saturn's magnetosphere. *Journal of Geophysical Research*, 88(A11):8779–8789, November 1983. doi: 10.1029/JA088iA11p08779.

M. M. Cowee, S. P. Gary, H. Y. Wei, R. L. Tokar, and C. T. Russell. An explanation for the lack of ion cyclotron wave generation by pikcup ions at Titan: 1-D hybrid simulation results. *Journal of Geophysical Research*, 115, 2010. doi: 10.1029/2010JA015769.

F. J. Crary and F. Bagenal. Ion cyclotron waves, pickup ions, and Io's neutral exosphere. *Journal of Geophysical Research*, 105(A11):25379–25389, November 2000. doi: 10.1029/2000JA000055.

T. E. Cravens, I. P. Robertson, S. A. Ledvina, D. Mitchell, S. M. Krimigis, and J. H. Waite. Energetic ion precipitation at Titan. *Geophysical Research Letters*, 35, 2008. doi: 10.1029/2007GL032451.

T. E. Cravens, R. V. Yelle, J.-E. Wahlund, D. E. Shemansky, and A. F. Nagy. Composition and Structure of the Ionosphere and Thermosphere. In R. H. Brown, J.-P. Lebreton, and J. H. Waite, editors, *Titan from Cassini-Huygens*, chapter 11, pages 259–296. Springer, 2009.

J. Cui, M. Galand, R. V. Yelle, J.-E. Wahlund, K. Ågren, J. H. Waite, and M. K. Dougherty. Ion transport in Titan's upper atmosphere. *Journal of Geophysical Research*, 115, 2010. doi: 10.1029/2009JA014563.

J. Cui, R. V. Yelle, I. C. F. Müller-Wodarg, and P. P. Lavvas. The implications of the H2 variability in Titan's exosphere. *Journal of Geophysical Research*, 116(A11), November 2011. doi: 10.1029/2011JA016808.

K. Dialynas, S. M. Krimigis, D. G. Mitchell, D. C. Hamilton, N. Krupp, and P. C. Brandt. Energetic ion spectral characteristics in the Saturnian magnetosphere using Cassini/MIMI measurements. *Journal of Geophysical Research*, 2009.

M. K. Dougherty, S. Kellock D. J. Southwood, A. Balogh, E. J. Smith, B. T. Tsurutani, B. Gerlach, K.-H. Glassmeier, F. Gleim, C. T. Russell, G. Erdos, F. M. Neubauer, and S. W. H. Cowley. The Cassini magnetic field investigation. *Space Science Reviews*, 2004.

M. K. Dougherty, N. Achilleos, N. André, C. S. Arridge, A. Balogh, C. Bertucci, M. E. Burton, S. W. H. Cowley, G. Erdos, G. Giampieri, K.-H. Glassmeier, K. K. Khurana, J. Leisner, F. M. Neubauer, C. T. Russell, E. J. Smith, D. J. Southwood, and B. T. Tsurutani. Cassini Magnetometer Observations During Saturn Orbit Insertion. *Science*, 307(5713):1266–1270, February 2005. doi: 10.1126/science.1106098.

M. K. Dougherty, K. K. Khurana, F. M. Neubauer, C. T. Russell, J. Saur, J. S. Leisner, and M. E. Burton. Identification of a Dynamic Atmosphere at Enceladus with the Cassini Magnetometer. *Science*, 311(5766):1406–1409, March 2006. doi: 10.1126/science.1120985.

J. W. Dungey. Interplanetary Magnetic Field and the Auroral Zones. *Physical Review Letters*, 6(2):47–48, January 1961. doi: 10.1103/PhysRevLett.6.47.

N. J. T. Edberg, D. J. Andrews, O. Shebanits, K. Ågren, J.-E. Wahlund, H. J. Opgenoorth, E. Roussos, P. Garnier, T. E. Cravens, S. V. Badman, R. Modolo, C. Bertucci, and M. K. Dougherty. Extreme densities in Titan's ionosphere during the T85 magnetosheath encounter. *Geophysical Research Letters*, 2013.

N. J. T. Edberg, D. J. Andrews, C. Bertucci, D. A. Gurnett, M. K. G. Holmberg, C. M. Jackman, W. S. Kurth, J. D. Menietti, H. J. Opgenoorth, O. Shebanits, E. Vigren, and J.-E. Wahlund. Effects of Saturn's magnetospheric dynamics on Titan's ionosphere. *Journal of Geophysical Research*, 120(10):8884–8898, October 2015. doi: 10.1002/2015JA021373.

M. Feyerabend, S. Simon, U. Motschmann, J. Saur, and L. Liuzzo. Filamented ion tail structures at Titan: A hybrid simulation study. *Planetary and Space Science*, page in press, 2015.

M. Feyerabend, S. Simon, F. M. Neubauer, U. Motschmann, C. Bertucci, N. J. T. Edberg, G. B. Hospodarsky, and W. S. Kurth. Hybrid simulation of Titan's interaction with the supersonic solar wind during Cassini's T96 flyby. *Geophysical Research Letters*, 43(1):35–42, January 2016. doi: 10.1002/2015GL066848.

M. Galand, R. Yelle, J. Cui, J.-E. Wahlund, V. Vuitton, A. Wellbrock, and A. J. Coates. Ionization sources in Titan's deep ionosphere. *Journal of Geophysical Research*, 2010.

P. Garnier, I. Dandouras, D. Toublanc, P. C. Brandt, E. C. Roelof, D. G. Mitchell, S. M. Krimigis, N. Krupp, D. C. Hamilton, and H. Waite. The exosphere of Titan and its interaction with the kronian magnetosphere: MIMI observations and modeling. *Planetary and Space Science*, 55(1-2):165–173, January 2007. doi: 10.1016/j.pss.2006.07.006.

P. Garnier, I. Dandouras, D. Toublanc, E. C. Roelof, P. C. Brandt, D. G. Mitchell, S. M. Krimigis, N. Krupp, D. C. Hamilton, and J.-E. Wahlund. Statistical analysis of the energetic ion and ENA data for the Titan environment. *Planetary and Space Science*, 2010.

T. I. Gombosi, T. P. Armstrong, C. S. Arridge, K. K. Khurana, S. M. Krimigis, N. Krupp, A. M. Persoon, and M. F. Thomsen. Saturn's Magnetospheric Configuration. In M. K. Dougherty, L. W. Esposito, and S. M. Krimigis, editors, *Saturn from Cassini-Huygens*, chapter 9, pages 203–255. Springer, 2009.

C. J. Hansen, L. Esposito, A. I. F. Stewart, J. Colwell, A. Hendrix, W. Pryor, D. Shemansky, and R. West. Enceladus' Water Vapor Plume. *Science*, 311(5766):1422–1425, March 2006. doi: 10.1126/science.1121254.

R. E. Hartle, E. C. Sittler Jr., K. W. Ogilvie, J. D. Scudder, A. J. Lazarus, and S. K.

Atreya. Titan's ion exosphere observed from Voyager 1. *Journal of Geophysical Research*, 87(A3):1383–1394, March 1982. doi: 10.1029/JA087iA03p01383.

R. E. Hartle, E. C. Sittler, F. M. Neubauer, R. E. Johnson, H. T. Smith, F. Crary, D. J. McComas, D. T. Young, A. J. Coates, D. Simpson, S. Bolton, D. Reisenfeld, K. Szego, J. J. Berthelier, A. Rymer, J. Vilppola, J. T. Steinberg, and N. Andre. Preliminary interpretation of Titan plasma interaction as observed by the Cassini Plasma Spectrometer: Comparisons with Voyager 1. *Geophysical Research Letters*, 33, 2006. doi: 10.1029/2005GL024817.

R. E. Hartle, M. Sarantos, and E. C. Sittler. Pickup ion distributions from three-dimensional neutral exospheres. *Journal of Geophysical Research*, 116(A10), October 2011. doi: 10.1029/2011JA016859.

P. Hedelt, Y. Ito, H. U. Keller, R. Reulker, P. Wurz, H. Lammer, H. Rauer, and L. Esposito. Titan's atomic hydrogen corona. *Icarus*, 210(1):424–435, November 2010. doi: 10.1016/j.icarus,2010.06.012.

D. E. Huddleston, R. J. Strangeway, X. Blanco-Cano, C. T. Russell, M. G. Kivelson, and K. K. Khurana. Io-jupiter interaction: Waves generated by pickup ions. *Advances in Space Research*, 26(10):1513–1518, 2000. doi: 10.1016/S0273-1177(00)00091-0.

W. J. Hughes. *Introduction to Space Physics*, chapter 9. Cambridge University Press, 1995.

X. Jia and M. G. Kivelson. Dawn-dusk asymmetries in rotating magnetospheres: Lessons from modeling Saturn. *Journal of Geophysical Research*, 121(2):1413–1424, February 2016. doi: 10.1002/2015JA021950.

R. E. Johnson, O. J. Tucker, M. Michael, E. C. Sittler, H. T. Smith, D. T. Young, and J. H. Waite. Mass Loss Processes in Titan's Upper Atmosphere. In R. H. Brown, J.-P. Lebreton, and J. H. Waite, editors, *Titan from Cassini-Huygens*, chapter 15, pages 373–391. Springer, 2009.

K. Kabin, R. L. Israelevich, A. I. Ershkovich, F. M. Neubauer, T. I. Gombosi, D. L. De Zeeuw, and K. G. Powell. Titan's magnetic wake: Atmospheric or magnetospheric interaction. *Journal of Geophysical Research*, 105(A5):10761–10770, May 2000. doi: 10.1029/2000JA900012.

M.-B. Kallenrode. *Space Physics*. Springer, 2004.

E. Kallio, J.-Y. Chaufray, R. Modolo, D. Snowden, and R. Winglee. Modeling of Venus, Mars, and Titan. *Space Science Reviews*, 162(1):267–307, December 2011. doi: 10.1007/s11214-011-9814-8.

K. K. Khurana, C. S. Arridge, H. Schwarzl, and M. K. Dougherty. A model of Saturn's magnetospheric field based on latest Cassini observations. In *American Geophysical Union Spring Meeting Abstracts*, 2006.

M. G. Kivelson and C. T. Russell, editors. *Introduction to Space Physics*. Cambridge University Press, 1995.

A. Kotova, E. Roussos, N. Krupp, and I. Dandouras. Modeling of the energetic ion observations in the vicinity of Rhea and Dione. *Icarus*, 258:402–417, 2015. doi: 10.106/j.icarus.2015.06.031.

S. M. Krimigis, D. G. Mitchell, D. C. Hamilton, S. Livi, J. Dandouras, S. Jaskulek, T. P. Armstrong, J. D. Boldt, A. F. Cheng, G. Gloeckler, J. R. Hayes, K. C. Hsieh, W.-H. Ip, E. P. Keath, E. Kirsch, N. Krupp, L. J. Lanzerotti, R. Lundgren, B. H. Mauk, R. W. McEntire, E. C. Roelof, C. E. Schlemm, B. E. Tossman, B. Wilken, and D. J. Williams. Magnetosphere Imaging Instrument (MIMI) on the Cassini Mission to Saturn/Titan. *Space Science Reviews*, 2004.

S. M. Krimigis, D. G. Mitchell, D. C. Hamilton, N. Krupp, S. Livi, E. C. Roelof, J. Dandouras, T. P. Armstrong, B. H. Mauk, C. Paranicas, P. C. Brandt, S. Bolton, A. F. Cheng, T. Choo, G. Gloeckler, J. Hayes, K. C. Hsieh, W.-H. Ip, S. Jaskulek, E. P. Keath, E. Kirsch, M. Kusterer, A. Lagg, L. J. Lanzerotti, D. LaVallee, J. Manweiler, R. W. McEntire, W. Rasmuss, J. Saur, F. S. Turner,

D. J. Williams, and J. Woch. Dynamics of Saturn's Magnetosphere from MIMI During Cassini's Orbital Insertion. *Science*, 307(5713):1270–1273, February 2005. doi: 10.1126/science.1105978.

N. Krupp. Giant magnetospheres in our solar system: Jupiter and Saturn compared. *The Astronomy and Astrophysics Review*, 22, October 2014. doi: 10.1007/s00159-014-0075-x.

N. Krupp, E. Roussos, A. Lagg, J. Woch, A. L. Müller, S. M. Krimigis, D. G. Mitchell, E. C. Roelof, C. Paranicas, J. Carbary, G. H. Jones, D. C. Hamilton, S. Livi, T. P. Armstrong, M. K. Dougherty, and N. Sergis. Energetic particles in Saturn's magnetosphere during the Cassini nominal mission (July 2004 - July 2008). *Planetary and Space Science*, 57(14-15):1754–1768, December 2009. doi: 10.1016/j.pss.2009.06.010.

N. Krupp, E. Roussos, P. Kollmann, C. Paranicas, D. G. Mitchell, S. M. Krimigis, A. Rymer, G. H. Jones, C. S. Arridge, T. P. Armstrong, and K. K. Khurana. The Cassini Enceladus encounters 2005-2010 in the view of energetic electron measurements. *Icarus*, 218(1):433–447, March 2012. doi: 10.1016/j.icarus.2011.12.018.

S. A. Ledvina and S. H. Brecht. Consequences of negative ions for Titan's plasma interaction. *Geophysical Research Letters*, 39(20), October 2012. doi: 10.1029/2012GL053835.

S. A. Ledvina and T. E. Cravens. A three-dimensional MHD model of plasma flow around Titan. *Planetary and Space Science*, 46(9-10):1175–1191, October 1998. doi: 10.1016/S0032-0633(98)00052-X.

S. A. Ledvina, T. E. Cravens, and K. Kecskeméty. Ion distributions in Saturn's magnetosphere near Titan. *Journal of Geophysical Research*, 110, 2005. doi: 10.1029/2004JA010771.

S. A. Ledvina, Y.-J. Ma, and E. Kallio. Modeling and Simulating Flowing Plasmas

and Related Phenomena. *Space Science Reviews*, 139(1):143–189, August 2008. doi: 10.1007/s11214-008-9384-6.

S. A. Ledvina, S. H. Brecht, and T. E. Cravens. The orientation of Titan's day-side ionosphere and its effects on Titan's plasma interaction. *Earth, Planets and Space*, 2012.

J. J. López-Moreno, G. J. Molina-Cuberos, M. Hamelin, R. Grard, F. Sim oes, R. Godard, K. Schwingenschuh, C. Béghin, J. J. Berthelier, V. J. G. Brown, P. Falkner, F. Ferri, M. Fulchignoni, I. Jernej, J. M. Jerónimo, R. Rodrigo, and R. Trautner. Structure of Titan's low altitude ionized layer from the Relaxation Probe onboard HUYGENS. *Geophysical Research Letters*, 35(22), November 2008. doi: 10.1029/2008GL035338.

Y. J. Ma, A. F. Nagy, G. Toth, T. E. Cravens, C. T. Russell, T. I. Gombosi, J.-E. Wahlund, F. J. Crary, A. J. Coates, C. L. Bertucci, and F. M. Neubauer. 3D global multi-species Hall-MHD simulation of the Cassini T9 flyby. *Geophysical Research Letters*, 34(24), December 2007. doi: 10.1029/2007GL031627.

Y. J. Ma, C. T. Russell, A. F. Nagy, G. Toth, C. Bertucci, M. K. Dougherty, F. M. Neubauer, A. Wellbrock, A. J. Coates, P. Garnier, J.-E. Wahlund, T. E. Cravens, and F. J. Crary. Time-dependent global MHD simulations of Cassini T32 flyby: From magnetosphere to magnetosheath. *Journal of Geophysical Research*, 114 (A3), March 2009. doi: 10.1029/2008JA013676.

R. Marchand. Test-Particle Simulation of Space Plasmas. *Communications in Computational Physics*, 8(3):471–483, 2010. doi: 10.4208/cicp.201009.280110a.

B. H. Mauk, D. C. Hamilton, T. W. Hill, G. B. Hospodarsky, R. E. Johnson, C. Paranicas, E. Roussos, C. T. Russell, D. E. Shemansky, E. C. Sittler Jr., and R. M. Thorne. Fundamental Plasma Processes in Saturn's Magnetosphere. In M. K. Dougherty, L. W. Esposito, and S. M. Krimigis, editors, *Saturn from Cassini-Huygens*, chapter 11, pages 281–332. Springer, 2009.

C. E. McIlwain. Coordinates for mapping the distribution of magnetically trapped particles. *Journal of Geophysical Research*, 66(11):3681–3691, November 1961. doi: 10.1029/JZ066i011p03681.

M. Michael, R. E. Johnson, F. Leblanc, M. Liu, J. G. Luhmann, and V. I. Shematovich. Ejection of nitrogen from Titan's atmosphere by magnetospheric ions and pick-up ions. *Icarus*, 175(1):263–267, May 2005. doi: 10.1016/j.icarus.2004.11.004.

R. Modolo, G. M. Chanteur, J.-E. Wahlund, P. Canu, W. S. Kurth, D. Gurnett, A. P. Matthews, and C. Bertucci. Plasma environment in the wake of Titan from hybrid simulation: A case study. *Geophysical Research Letters*, 34(24), December 2007. doi: 10.1029/2007GL030489.

J. Müller. *A.I.K.E.F.: An Adaptive Hybrid Model with Application to Fossil Fields at Titan and Mercury's Double Magnetopause*. PhD thesis, TU Braunschweig, 2012.

J. Müller, S. Simon, U. Motschmann, J. Schüle, K.-H. Glassmeier, and G. J. Pringle. A.I.K.E.F.: Adaptive hybrid model for space plasma simulations. *Computer Physics Communications*, 2011.

N. F. Ness, M. H. Acuna, K. W. Behannon, and F. M. Neubauer. The induced magnetosphere of Titan. *Journal of Geophysical Research*, 87(A3):1369–1381, March 1982. doi: 10.1029/JA087iA03p01369.

F. M. Neubauer, D. A. Gurnett, J. D. Scudder, and R. E. Hartle. Titan's magnetospheric interaction. In T. Gehrels and M. S. Matthews, editors, *Saturn*. University of Arizona Press, 1984.

F. M. Neubauer, H. Backes, M. K. Dougherty, A. Wennmacher, C. T. Russell, A. Coates, D. Young, N. Achilleos, N. André, C. S. Arridge, C. Bertucci, G. H. Jones, K. K. Khurana, T. Knetter, A. Law, G. R. Lewis, and J. Saur. Titan's near magnetotail from magnetic field and electron plasma observations and modeling: Cassini flybys TA, TB and T3. *Journal of Geophysical Research*, 2006.

F. Raulin, C. McKay, J. Lunine, and T. Owen. Titan's Astrobiology. In M. K. Dougherty, L. W. Esposito, and S. M. Krimigis, editors, *Titan from Cassini-Huygens*, chapter 9, pages 215–234. Springer, 2009.

P. L. Read, T. E. Dowling, and G. Schubert. Saturn's rotation period from its atmospheric planetary-wave configuration. *Nature*, 2009.

L. H. Regoli, E. Roussos, M. Feyerabend, G. H. Jones, N. Krupp, A. J. Coates, S. Simon, U. Motschmann, and M. K. Dougherty. Access of energetic particles to Titan's exobase: A study of Cassini's T9 flyby. *Planetary and Space Science*, 2015. doi: 10.1016/j.pss.2015.11.013.

L. H. Regoli, A. J. Coates, M. F. Thomsen, G. H. Jones, E. Roussos, J. H. Waite, N. Krupp, and G. Cox. Survey of pickup ion signatures in the vicinity of Titan using CAPS/IMS. *Journal of Geophysical Research*, August 2016. doi: 10.1002/2016JA022617.

J. G. Roederer. On the Adiabatic Motion of Energetic Particles in a Model Magnetosphere. *Journal of Geophysical Research*, 1967.

J. G. Roederer. *Dynamics of Geomagnetically Trapped Radiation*. Springer, 1970.

E. Roussos, N. Krupp, T. P. Armstrong, C. Paranicas, D. G. Mitchell, S. M. Krimigis, G. H. Jones, K. Dialynas, N. Sergis, and D. C. Hamilton. Discovery of a transient radiation belt at Saturn. *Geophysical Research Letters*, 35(22), November 2008. doi: 10.1029/2008GL035767.

C. T. Russell, C. M. Jackman, H. Y. Wei, C. Bertucci, and M. K. Dougherty. Titan's influence on Saturnian substorm occurrence. *Geophysical Research Letters*, 35 (12), June 2008. doi: 10.1029/2008GL034080.

C. T. Russell, H. Y. Wei, M. M. Cowee, F. M. Neubauer, and M. K. Dougherty. Ion Cyclotron Waves at Titan. *Journal of Geophysical Research*, 2016. doi: 10.1002/2015JA022293.

A. M. Rymer, H. T. Smith, A. Wellbrock, A. J. Coates, and D. T. Young. Discrete classification and electron energy spectra of Titan's varied magnetospheric environment. *Geophysical Research Letters*, 36, 2009. doi: 10.1029/2009GL039427.

N. Sergis, S. M. Krimigis, D. G. Mitchell, D. C. Hamilton, N. Krupp, B. M. Mauk, E. C. Roelof, and M. Dougherty. Ring current at Saturn: Energetic particle pressure in Saturn's equatorial magnetosphere measured with Cassini/MIMI. *Geophysical Research Letters*, 34(9), May 2007. doi: 10.1029/2006GL029223.

N. Sergis, S. M. Krimigis, D. G. Mitchell, D. C. Hamilton, N. Krupp, B. H. Mauk, E. C. Roelof, and M. K. Dougherty. Energetic particle pressure in Saturn's magnetosphere measured with the Magnetospheric Imaging Instrument on Cassini. *Journal of Geophysical Research*, 114(A2), February 2009. doi: 10.1029/2008JA013774.

M. B. Shah, C. J. Latimer, E. C. Montenegro, O. J. Tucker, R. E. Johnson, and H. T. Smith. The implantation and interactions of O^+ in Titan's atmosphere: laboratory measurements of collision-induced dissociation of N_2 and modeling of positive ion formation. *The Astrophysical Journal*, 703:1947–1954, 2009. doi: 10.1088/0004-637X/703/2/1947.

I. Sillanpää and R. E. Johnson. The role of ion-neutral collisions in Titan's magnetospheric interaction. *Planetary and Space Science*, 108:73–86, 2015. doi: 10.1016/j.pss.2015.01.007.

I. Sillanpää, E. Kallio, R. Jarvinen, and P. Janhunen. Oxygen ions at Titan's exobase in a Voyager 1-type interaction from a hybrid simulation. *Journal of Geophysical Research*, 112(A12), December 2007. doi: 10.1029/2007JA012348.

I. Sillanpää, D. T. Young, F. Crary, M. Thomsen, D. Reisenfeld, J.-E. Wahlund, C. Bertucci, E. Kallio, R. Jarvinen, and P. Janhunen. Cassini Plasma Spectrometer and hybrid model study on Titan's interaction: Effect of oxygen ions. *Journal of Geophysical Research*, 116(A7), July 2011. doi: 10.1029/2011JA016443.

S. Simon, A. Bößwetter, T. Bagdonat, U. Motschmann, and K.-H. Glassmeier. Plasma environment at Titan: a 3-D hybrid simulation study. *Annales Geophysicae*, 24(3):1113–1135, May 2006. doi: 10.5194/angeo-24-1113-2006.

S. Simon, G. Kleindienst, A. Boesswetter, T. Bagdonat, U. Motschmann, K.-H. Glassmeier, J. Schuele, C. Bertucci, and M. K. Dougherty. Hybrid simulation of Titan's magnetic field signature during the Cassini T9 flyby. *Geophysical Research Letters*, 2007.

S. Simon, A. Wennmacher, F. M. Neubauer, C. L. Bertucci, H. Kriegel, J. Saur, C. T. Russell, and M. K. Dougherty. Titan's highly dynamic magnetic environment: A systematic survey of Cassini magnetometer observations from flybys TA–T62. *Planetary and Space Science*, 58(10):1230–1251, August 2010. doi: 10.1016/j.pss.2010.04.021.

S. Simon, S. C. van Treeck, A. Wennmacher, J. Saur, F. M. Neubauer, C. L. Bertucci, and M. K. Dougherty. Structure of Titan's induced magnetosphere under varying background magnetic field conditions: Survey of Cassini magnetometer data from flybys TA-T85. *Journal of Geophysical Research*, 118(4):1679–1699, April 2013. doi: 10.1002/jgra.50096.

S. Simon, E. Roussos, and C. S. Paty. The interaction between Saturn's moons and their plasma environments. *Physics Reports*, 602:1–65, November 2015. doi: 10.1016/j.physrep.2015.09.005.

E. C. Sittler, R. E. Hartle, C. Bertucci, A. Coates, T. Cravens, I. Dandouras, and D. Shemansky. Energy Deposition Processes in Titan's Upper Atmosphere and Its Induced Magnetosphere. In R. H. Brown, J.-P. Lebreton, and J. H. Waite, editors, *Titan from Cassini-Huygens*, chapter 16, pages 393–454. Springer, 2009.

E. C. Sittler, R. E. Hartle, R. E. Johnson, J. F. Cooper, A. S. Lipatov, C. Bertucci, A. J. Coates, K. Szego, M. Shappirio, D. G. Simpson, and J.-E. Wahlund. Saturn's magnetospheric interaction with Titan as defined by Cassini encounters T9 and

T18: New results. *Planetary and Space Science*, 58:327–350, 2010. doi: 10.1016/j.pss.2009.09.017.

H. T. Smith and A. M. Rymer. An empirical model for the plasma environment along Titan's orbit based on Cassini plasma observations. *Journal of Geophysical Research*, 119(7):5674–5684, July 2014. doi: 10.1002/2014JA019872.

H. T. Smith, R. E. Johnson, and V. I. Shematovich. Titan's atomic and molecular nitrogen tori. *Geophysical Research Letters*, 31(16), August 2004. doi: 10.1029/2004GL020580.

H. T. Smith, R. E. Johnson, E. C. Sittler, M. Shappirio, D. Reisenfeld, O. J. Tucker, M. Burger, F. J. Crary, D. J. McComas, and D. T. Young. Enceladus: The likely dominant nitrogen source in Saturn's magnetosphere. *Icarus*, 188(2):356–366, June 2007. doi: 10.1016/j.icarus.2006.12.007.

H. T. Smith, D. G. Mitchell, R. E. Johnson, and C. P. Paranicas. Investigation of energetic proton penetration in Titan's atmosphere using the Cassini INCA instrument. *Planetary and Space Science*, 57(13):1538–1546, November 2009. doi: 10.1016/j.pss.2009.03.013.

M. F. Smith and M. Lockwood. Earth's magnetospheric cusps. *Review of Geophysics*, 34(2):233–260, May 1996. doi: 10.1029/96RG00893.

D. Snowden and R. V. Yelle. The global precipitation of magnetospheric electrons into Titan's upper atmosphere. *Icarus*, 143:1–15, November 2014. doi: 10.1016/j.icarus.2014.08.027.

D. Snowden, R. Winglee, C. Bertucci, and M. K. Dougherty. Three-dimensional multifluid simulation of the plasma interaction at Titan. *Journal of Geophysical Research*, 2007.

D. F. Strobel. Titan's hydrodynamically escaping atmosphere: Escape rates and the structure of the exobase region. *Icarus*, 202(2):632–641, August 2009. doi: 10.1016/j.icarus.2009.03.007.

D. F. Strobel and J. Cui. Titan's upper atmosphere/exosphere, escape processes, and rates. In I. Müller-Wodarg, C. A. Griffith, E. Lellouch, and T. E. Cravens, editors, *Titan: Interior, Surface, Atmosphere, and Space Environment*, chapter 10, pages 355–375. Cambridge University Press, 2014. doi: 10.1017/CBO9780511667398.013.

B. D. Teolis and J. H. Waite. Dione and Rhea seasonal exospheres revealed by Cassini CAPS and INMS. *Icarus*, 272:277–289, July 2016. doi: 10.1016/j.icarus.2016.02.031.

B. D. Teolis, G. H. Jones, P. F. Miles, R. L. Tokar, B. A. Magee, J. H. Waite, E. Roussos, D. T. Young, F. J. Crary, A. J. Coates, R. E. Johnson, W.-L. Tseng, and R. A. Baragiola. Cassini Finds an Oxygen–Carbon Dioxide Atmosphere at Saturn's Icy Moon Rhea. *Science*, 330(6012):1813–1815, December 2010. doi: 10.1126/science.1198366.

N. Thomas, F. Bagenal, T. W. Hill, and J. K. Wilson. The Io neutral clouds and plasma torus. In F. Bagenal, T. E. Dowling, and W. B. McKinnon, editors, *Jupiter. The Planet, Satellites and Magnetosphere*, chapter 23, pages 561–591. Cambridge University Press, 2004.

M. F. Thomsen, D. B. Reisenfeld, D. M. Delapp, R. L. Tokar, D. T. Young, F. J. Crary, E. C. Sittler, M. A. McGraw, and J. D. Williams. Survey of ion plasma parameters in Saturn's magnetosphere. *Journal of Geophysical Research*, 115 (A10), October 2010. doi: 10.1029/2010JA015267.

R. L. Tokar, R. E. Johnson, M. F. Thomsen, E. C. Sittler, A. J. Coates, R. J. Wilson, F. J. Crary, D. T. Young, and G. H. Jones. Detection of exospheric O2+ at Saturn's moon Dione. *Geophysical Research Letters*, 39(3), February 2012. doi: 10.1029/2011GL050452.

W.-L. Tseng, W.-H. Ip, and A. Kopp. Exospheric heating by pickup ions at Titan. *Advances in Space Research*, 42:54–60, 2008. doi: 10.1016/j.asr.2008.03.009.

O. J. Tucker and R. E. Johnson. Thermally driven atmospheric escape: Monte Carlo simulations for Titan's atmosphere. *Planetary and Space Science*, 57(14-15): 1889–1894, December 2009. doi: 10.1016/j.pss.2009.06.003.

J. A. Van Allen. Energetic particles in the inner magnetosphere of Saturn. In T. Gehrels and M. S. Matthews, editors, *Saturn*. University of Arizona PressArizona, 1984.

V. M. Vasyliūnas. A survey of low-energy electrons in the evening sector of the magnetosphere with OGO 1 and OGO 3. *Journal of Geophysical Research*, 73: 2839–2884, May 1968. doi: 10.1029/JA073i009p02839.

V. M. Vasyliūnas. Plasma distribution and flow. In A. J. Dessler, editor, *Physics of the Jovian Magnetosphere*. Cambridge University Press, 1983.

A. N. Volkov, R. E. Johnson, O. J. Tucker, and J. T. Erwin. Thermally driven atmospheric escape: transition from hydrodynamic to Jeans escape. *The Astrophysical Journal Letters*, 729(2), February 2011. doi: 10.1088/2041-8205/729/2/L24.

J.-E. Wahlund, R. Boström, G. Gustafsson, D. A. Gurnett, W. S. Kurth, A. Pedersen, T. F. Averkamp, G. B. Hospodarsky, A. M. Persoon, P. Canu, F. M. Neubauer, M. K. Dougherty, A. I. Eriksson, M. W. Morooka, R. Gill, M. André, L. Eliasson, and I. Müller-Wodarg. Cassini Measurements of Cold Plasma in the Ionosphere of Titan. *Science*, 308(5724):986–989, May 2005. doi: 10.1126/science.1109807.

J. H. Waite, W. S. Lewis, W. T. Kasprzak, V. G. Ancich, B. P. Block, T. E. Cravens, G. G. Fletcher, W.-H. Ip, J. G. Luhmann, R. L. McNutt, H. B. Niemann, J. K. Parjko, J. E. Richards, R. L. Thorpe, E. M. Walter, and R. V. Yelle. The Cassini Ion and Neutral Mass Spectrometer (INMS) Investigation. *Space Science Reviews*, 114(1):113–231, September 2004. doi: 10.1007/s11214-004-14082-2.

H. Y. Wei, C. T. Russell, A. Wellbrock, M. K. Dougherty, and A. J. Coates. Plasma environment at Titan's orbit with Titan present and absent. *Geophysical Research Letters*, 36(23), December 2009. doi: 10.1029/2009GL041048.

A. Wellbrock, A. J. Coates, G. H. Jones, G. R. Lewis, and J. H. Waite. Cassini CAPS-ELS observations of negative ions in Titan's ionosphere: Trends of density with altitude. *Geophysical Research Letters*, 40(17):4481–4485, September 2013. doi: 10.1002/grl.50751.

J. H. Westlake, C. P. Paranicas, T. E. Cravens, J. G. Luhmann, K. E. Mandt, H. T. Smith, D. G. Mitchell, A. M. Rymer, M. E. Perry, J. H. Waite Jr., and J.-E. Wahlund. The observed composition of ions outflowing from Titan. *Geophysical Research Letters*, 39(19), October 2012. doi: 10.1029/2012GL053079.

V. Wulms, J. Saur, D. F. Strobel, S. Simon, and D. G. Mitchell. Energetic neutral atoms from Titan: Particle simulations in draped magnetic and electric fields. *Journal of Geophysical Research*, 2010.

R. V. Yelle, D. F. Strobel, E. Lellouch, and D. Gautier. Engineering Models for Titan's Atmosphere. *ESA SP-1177*, 1997.

R. V. Yelle, J. Cui, and I. C. F. Müller-Wodarg. Methane escape from Titan's atmosphere. *Journal of Geophysical Research*, 113(E10), October 2008. doi: 10.1029/2007JE003031.

R. V. Yelle, D. S. Snowden, and I. C. F. Müller-Wodarg. Titan's upper atmosphere: thermal structure, dynamics, and energetics. In I. Müller-Wodarg, C. A. Griffith, E. Lellouch, and T. E. Cravens, editors, *Titan: Interior, Surface, Atmosphere, and Space Environment*, chapter 9, pages 322–354. Cambridge University Press, 2014. doi: 10.1017/CBO9780511667398.012.

D. T. Young, J. J. Berthelier, M. Blanc, J. L. Burch, A. J. Coates, R. Goldstein, M. Grande, T. W. Hill, R. E. Johnson, V. Kelha, D. J. McComas, E. C. Sittler, K. R. Svenes, K. Szegö, P. Tanskanen, K. Ahola, D. Anderson, S. Bakshi, R. A. Baragiola, B. L. Barraclough R. K. Black, S. Bolton, T. Booker, R. Bowman, P. Casey, F. J. Crary, D. Delapp, G. Dirks, N. Eaker, H. Funsten, J. D. Furman, J. T. Gosling, H. Hannula, C. Holmlund, H. Huomo, J. M. Illiano, P. Jensen, M. A. Johnson, D. R. Linder, T. Luntama, S. Maurice, K. P. McCabe, K. Mursula, B. T.

Narheim, J. E. Nordholt, A. Preece, J. Rudzki, A. Ruitberg, K. Smith, S. Szalai, M. F. Thomsen, K. Viherkanto, J. Vilppola, T. Vollmer, T. E. Wahl, M. Wüest, T. Ylikorpi, and C. Zinsmeyer. Cassini Plasma Spectrometer investigation. *Space Science Reviews*, 2004.

J. F. Ziegler, M. D. Ziegler, and J. P. Biersack. SRIM - The stopping and range of ions in matter (2010). *Nuclear Instruments and Methods in Physics Research B*, 268:1818–1823, 2010. doi: 10.1016/j.nimb.2010.02.091.